

FEMTOSECOND
MID-INFRARED
SPECTROSCOPY
OF
WATER



HAN-KWANG NIENHUYS

FEMTOSECOND MID-INFRARED
SPECTROSCOPY OF WATER

FEMTOSECOND MID-INFRARED SPECTROSCOPY OF WATER

PROEFSCHRIFT

ter verkrijging van de graad van doctor aan de Technische Universiteit
Eindhoven, op gezag van de Rector Magnificus, prof. dr. R. A. van Santen,
voor een commissie aangewezen door het College voor Promoties in het
openbaar te verdedigen op woensdag 30 januari 2002 om 16.00 uur

door

HAN-KWANG NIENHUYS

geboren te Utrecht

Dit proefschrift is goedgekeurd door de promotoren:

prof. dr. R. A. van Santen

en

prof. dr. H. J. Bakker

The work described in this thesis was performed at the FOM Institute for Atomic and Molecular Physics (AMOLF), Kruislaan 407, 1098 SJ Amsterdam, The Netherlands. This work is part of a collaborative research program of N10K (Netherlands Graduate School of Catalysis Research) and FOM (Foundation for Fundamental Research on Matter), which is financially supported by Nwo (Netherlands Organization for the Advancement of Research).

CIP-DATA LIBRARY TECHNISCHE UNIVERSITEIT EINDHOVEN

Nienhuys, Han-Kwang

Femtosecond mid-infrared spectroscopy of water / by Han-Kwang Nienhuys. – Eindhoven : Technische Universiteit Eindhoven, 2002.

Proefschrift. – ISBN 90-386-2703-3

NUGI 813

trefwoorden: fysische chemie / water / waterstofbruggen / tijdopgeloste laserspectroscopie / moleculaire vibraties

subject headings: physical chemistry / water / hydrogen bond / time-resolved laser spectroscopy / molecular vibration

CONTENTS

1	Introduction	10
1.1	The infrared absorption of water	11
1.2	Vibrational pump–probe spectroscopy	13
1.2.1	Absolute magnitude of the pump–probe signals	16
1.3	Outline of this thesis	16
2	Experimental details	18
2.1	Three-wave mixing as an infrared source	18
2.1.1	Parametric generation and amplification	19
2.2	Pulse generation for pump–probe experiments	20
2.2.1	Titanium-sapphire amplifier	20
2.2.2	Topas: a BBO-based OPG/OPA device	20
2.2.3	Pulse generation ($\sim 3 \mu\text{m}$) for one-color experiments	20
2.2.4	Pulse generation ($\sim 3 \mu\text{m}$) for two-color experiments	21
2.2.5	Pulse generation at $\sim 4 \mu\text{m}$	22
2.3	Sample	22
2.4	Pump–probe setup	23
2.4.1	Two-color setup	24
2.4.2	One-color polarization-resolved setup	25
2.5	Pulse characterisation	26
2.6	Refinements of the pump–probe signal description	27
2.7	Noise suppression	30
2.7.1	Uncorrelated noise	30
2.7.2	Time-correlated noise	32
2.8	Thermal effects in the sample	33
3	Generation of mid-infrared pulses by $\chi^{(3)}$ difference frequency generation in CaF_2 and BaF_2	36
3.1	Introduction	36
3.2	Experiment	37
3.3	Results	38
3.4	Conclusions	40
4	Vibrational relaxation in HDO: D_2O	41
4.1	Introduction	41
4.2	Experiment	41
4.3	Results	42
4.4	Intermediate-state model	43

4.5	Discussion	47
4.6	Conclusions	49
5	Isotope effects on vibrational relaxation and hydrogen-bond dynamics in water	50
5.1	Introduction	50
5.2	Experiment	51
5.3	Results	51
5.4	The Brownian-oscillator model	53
5.5	Thermalization and fits	55
5.6	Discussion	56
5.7	Conclusions	58
6	Dynamics of water molecules in an alkaline environment	59
6.1	Introduction	59
6.2	Experiment	61
6.3	Results	62
6.3.1	Transient spectra	62
6.3.2	The OH band as a distribution of Brownian oscillators	63
6.3.3	Dynamics at small delays	65
6.3.4	Fit details	67
6.4	Discussion	68
6.5	Conclusions	71
7	Orientational relaxation of HDO: D₂O as an activated process	73
7.1	Introduction	73
7.2	Experiment	75
7.3	Results	75
7.4	Activated reorientation and spectral diffusion	76
7.4.1	Model	76
7.4.2	Discussion of the model	79
7.4.3	Comparison with other studies	81
7.5	Conclusions	82
7.6	Appendix: mathematical details	82
7.6.1	Rotational diffusion	82
7.6.2	Spectral diffusion	83
7.6.3	Anisotropy decay at large delays	84
7.6.4	Numerical implementation	85
8	Spectral diffusion and mechanism for autodissociation	86
8.1	Introduction	86
8.2	Experiment	87
8.3	The equilibrated transient spectrum	87
8.3.1	Quantum-mechanical Lippincott-Schroeder model	88
8.3.2	Calculation of transient spectra	91
8.4	The dynamics of the transient spectra	93
8.4.1	Spectral diffusion	93

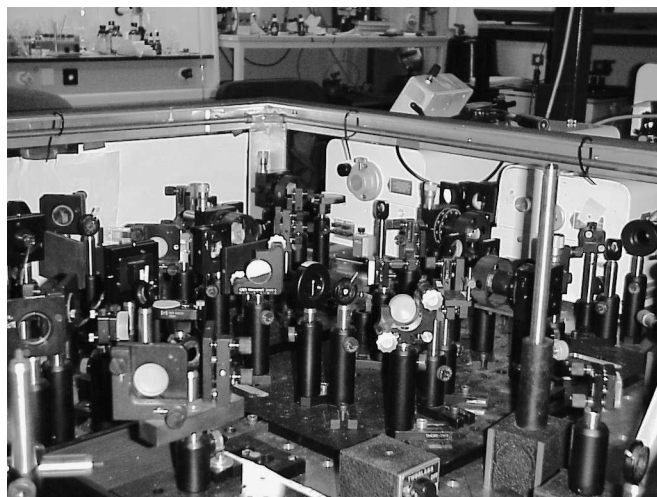
8.4.2	Inertial dynamics	95
8.5	Autodissociation of water	97
8.5.1	Transition state	98
8.5.2	Mechanism	100
8.6	Conclusions	100
	Appendix: The cm^{-1} unit	102
	Bibliography	103
	Summary	113
	Samenvatting	115
	Nawoord	119
	Curriculum Vitae	121
	Index	122
	Colophon	125

PUBLICATIONS COVERED IN THIS THESIS

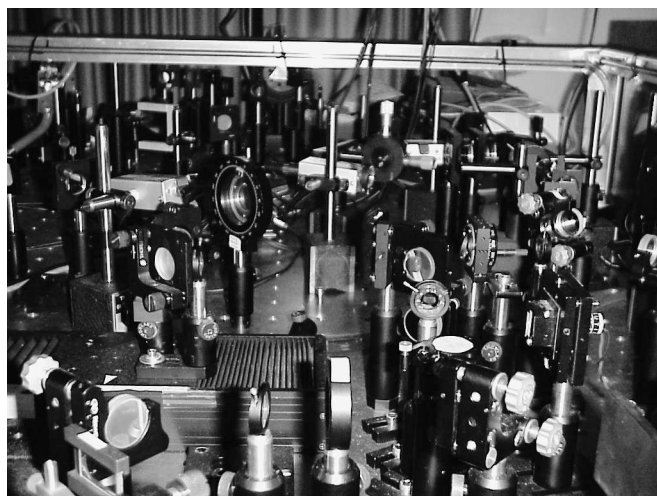
- H. K. Nienhuys, P. C. M. Planken, R. A. van Santen, and H. J. Bakker. Generation of mid-infrared pulses by $\chi^{(3)}$ difference frequency generation in CaF_2 and BaF_2 . *Opt. Lett.* *26*, 1350–1352 (2001).
- H. K. Nienhuys, S. Woutersen, R. A. van Santen, and H. J. Bakker. Mechanism for vibrational relaxation in water investigated by femtosecond infrared spectroscopy. *J. Chem. Phys.* *111*, 1494–1500 (1999).
- M. F. Kropman, H. K. Nienhuys, S. Woutersen, and H. J. Bakker. Vibrational relaxation and hydrogen-bond dynamics of $\text{HDO}:\text{H}_2\text{O}$. *J. Phys. Chem. A* *105*, 4622–4626 (2001).
- H. K. Nienhuys, A. Lock, R. A. van Santen, and H. J. Bakker. Dynamics of water molecules in an alkaline environment. *Submitted*.
- H. K. Nienhuys, R. A. van Santen, and H. J. Bakker. Orientational relaxation of liquid water molecules as an activated process. *J. Chem. Phys.* *112*, 8487–8494 (2000).
- H. J. Bakker, H. K. Nienhuys, G. Gallot, N. Lascoux, G. Gale, J. C. Leicknam, and S. Bratos. Fast inertial hydrogen-bond dynamics of liquid water. *Scheduled for publication in J. Chem. Phys.*, February 18 (2002).
- H. J. Bakker and H. K. Nienhuys. Transient Absorption of Vibrationally Excited Water. *Submitted*.

OTHER PUBLICATIONS

- C. van der Struijf, H. K. Nienhuys, D. Harryvan, G. Kothe, and Y. K. Levine. Influence of high orientational order on the shape of the echo response from a Hahn pulse sequence. *J. Magnetic Resonance* *130*, 253–261 (1998).
- S. Woutersen, U. Emmerichs, H. K. Nienhuys, and H. J. Bakker. Anomalous temperature dependence of vibrational lifetimes in water and ice. *Phys. Rev. Lett.* *81*, 1106–1109 (1998).
- H. J. Bakker, S. Woutersen, and H. K. Nienhuys. Reorientational motion and hydrogen-bond stretching dynamics in liquid water. *Chem. Phys.* *258*, 233–245 (2000).
- P. C. M. Planken, H. K. Nienhuys, H. J. Bakker, and W. Th. Wenckebach. Measurement and calculation of the orientation dependence of THz pulse detection in ZnTe . *J. Opt. Soc. Am. B* *18*, 313–317 (2001).
- M. A. F. H. van den Broek, H. K. Nienhuys, and H. J. Bakker. Vibrational dynamics of the C–O stretch vibration in alcohols. *J. Chem. Phys.* *114*, 3182–3186 (2001).
- M. F. Kropman, H.-K. Nienhuys, and H. J. Bakker. Real-time measurement of the orientational dynamics of aqueous solvation shells in bulk liquid water. *Submitted*.



The pulse-generation part of the experimental setup (schematic picture in Fig. 2.2 on page 21). The two white boxes at the right are two TOPASES. As an indication of the scale for those who are not familiar to optical experiments: most objects are about 15 cm in height.



The pump-probe part of the experimental setup (schematic picture in Fig. 2.3 on page 24). The sample (currently a germanium wafer with the purpose of finding time overlap) is located in the upper right corner.

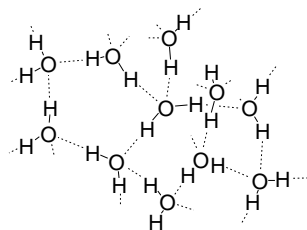
I INTRODUCTION

This thesis is about water and hydrogen bonding. That is: the properties of individual water molecules, whose collective behavior is responsible for how we experience water in everyday life. The first scientific knowledge of this kind was obtained by the end of the 18th century. At that time, chemists observed that ‘inflammable air’ (hydrogen), when burnt, would generate water vapor that fogged the glassware of their experiments. In 1781, Henry Cavendish was the first to synthesize water from correct proportions of hydrogen (which he assumed to be the element ‘phlogiston’ in pure form) and ‘dephlogisticated air’ (oxygen). Most likely, a considerable amount of shattered glass has been produced during the course of his experiments. Cavendish explained his observations in terms of the traditional alchemistic view that every material is composed of the elements earth, fire (phlogiston), water, and air. However, his discovery led Antoine Lavoisier, the founder of modern chemistry, to his demonstration in 1783 in front of a scientific audience that the summed weights of the oxygen and hydrogen gas in this synthesis were equal to the weight of the resulting water, that was ‘as pure as distilled water.’^{39,70} Though the concept of atoms and molecules was not very clear at the time, there was a notion that weights and chemical components are somehow conserved in chemical reactions. Therefore, we may regard these experiments as the first to prove that water is a compound consisting of hydrogen and oxygen in a fixed ratio. Nowadays, we learn at school that water has the chemical formula H_2O , but the simplicity of this formula is by no means reflected in the physical properties of this liquid. No other molecules with a comparable size and mass form a liquid at room temperature. The cause of water being liquid is the fact that every water molecule can form up to four hydrogen bonds with neighboring water molecules, which means that a three-dimensional network is formed, as shown in Fig. 1.1.

The hydrogen bonds in water are the attractive interactions between the H atom of a water molecule and the O atom of a neighboring water molecule. This attraction is 10 to 100 times weaker than the chemical bonds of the O–H groups. Due to this weakness, the network in liquid water is by no means static: hydrogen bonds are constantly formed and broken as the molecules change their position and orientation relative to one another.

Hydrogen bonds are not limited to attractions between water molecules. Generally, a

FIGURE 1.1. Hydrogen-bond network in liquid water. The dotted lines indicate hydrogen bonds, of which up to 4 can be formed per water molecule. On the average, a water molecule has 3.4 hydrogen bonds.¹¹⁶



hydrogen bond has the form



where the donating atom X is usually an N or O atom, and the accepting atom Y is usually either an N or O atom or a negative ion. For example, for the correct biological functioning of proteins and DNA molecules, two building blocks of life, the formation of $N-H \cdots O$ and $N-H \cdots N$ hydrogen bonds is essential.¹¹⁶ Further, the existence of hydrogen bonds between water molecules and the polarity of water molecules are responsible for water being an excellent solvent for polar molecules and salts, which is essential for many chemical reactions in both biochemistry and inorganic chemistry. Water is not only of chemical importance. As of today, a simple query on the scientific search engine INSPEC, which covers only the areas of physics and physical chemistry, generates 175,000 hits for articles with the word 'water' in the title or abstract, and 17,000 hits with 'hydrogen bond.'

The general importance of water is a constant motivation for seeking more knowledge about and understanding of the microscopic mechanisms that underly its properties. It has been suggested that the peculiar properties of liquid water, such as the temperature dependence of its density and viscosity,^{3,112} can be explained in terms of a two-state mixture model. In this view, molecules aggregate into clusters that come in two types of structure that have different properties.¹⁰² These aggregates would rapidly transform into one another. Whether water consists of two structures or not, the rapid breaking and forming of hydrogen bonds in liquid water does occur on an extremely rapid time scale, typically 10^{-12} seconds. Obtaining knowledge on processes requires experimental techniques that can resolve such processes. The next section concerns the effect of hydrogen bonds on the infrared spectrum of water, which is an ingredient for vibrational pump-probe spectroscopy, which satisfies this requirement and is used in this thesis.

I.I THE INFRARED ABSORPTION OF WATER

Generally, molecules absorb light at infrared wavelengths with a spectrum that is characteristic for its structure.⁵² In water, the absorption by OH groups is especially interesting. Figure 1.2 shows two transmittance spectra. One is the spectrum of ambient air, which has a complicated structure of absorption lines around 3700 cm^{-1} due to the presence of water vapor. (see the Appendix on page 102 about spectroscopic units.) The source of the infrared absorption is formed by two types of so-called stretch vibrations in the H_2O molecule, one at 3652 and one at 3756 cm^{-1} .[↓] These vibrational frequencies are well-defined,¹¹⁰ but the overwhelming number of additional possible rotational excitations, each of them responsible for a separate narrow line, obscures this fact completely, at least at first sight. The other spectrum is of liquid water, which does not show any fine structure and which is broader and shifted towards lower frequencies. The widths of the liquid and vapor spectrum have different origins. In liquid water, rapid rotations such as those in the gas phase are not possible, mainly due to the ubiquitous presence of hydrogen bonds. In fact, both the lower average frequency of the liquid spectrum and its broadening can be explained from hydrogen bonds. It is a general property of hydrogen bonds that

[↓] These two vibrational modes are known as the symmetric and anti-symmetric stretch modes, respectively. There is a third mode, the bend mode, that has a frequency of 1595 cm^{-1} , but this mode is not part of the spectral region under consideration.

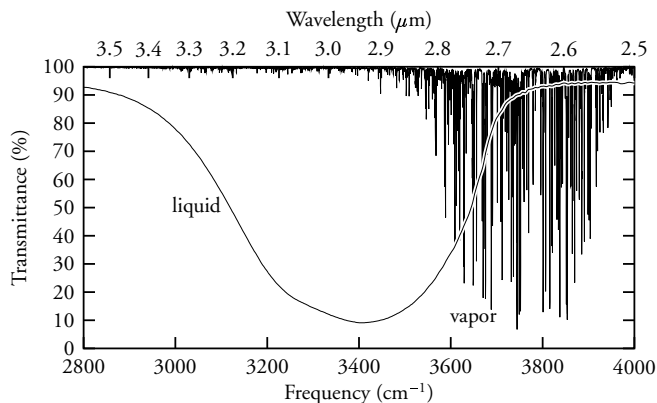


FIGURE 1.2. Transmittance spectrum of ordinary water (H_2O) vapor (~ 20 cm air of normal humidity at room-temperature) and transmittance spectrum of a water film with a thickness of $\sim 3 \mu\text{m}$.

they lower the vibrational frequency of the donating X–H group; this lowering effect is stronger for shorter XY-distances. References 77, 85, 92, 106 provide extensive data on the magnitude of this effect on O–H groups with various types of Y atoms; Ref. 114 provides a theoretical treatment. The presence of hydrogen bonds in liquid water and the variation in hydrogen-bond lengths, a consequence of the ever varying network structure in Fig. 1.1, cause the broad shape that ranges from 3200 to 3600 cm^{-1} .

The rapidly changing hydrogen bonds in liquid water cause the frequency of each participating OH group to fluctuate at a comparable rate. However, because an H_2O molecule has two separate independent vibrational frequencies that differ significantly, there is no single translation of vibrational frequency to hydrogen-bond length. However, if one H atom is replaced by a deuterium (D) atom, which combines chemical properties nearly identical to those of ordinary hydrogen with a mass that is twice as large, then the two vibrational modes will be clearly distinguishable. In such an HDO molecule, the OH stretch frequency is 3707 cm^{-1} in vapor¹¹⁰ and about 3400 cm^{-1} in the liquid phase, while the OD stretch frequency is 2727 cm^{-1} or 2500 cm^{-1} , respectively. Typically, we dissolve HDO molecules in D_2O , which has no significant infrared absorption in the range 3300 – 3700 cm^{-1} . Hence, in liquid HDO dissolved in D_2O , there is a reasonably well-defined relation between the OH stretch frequency and the hydrogen-bond length; Figure 1.3 shows the spectrum of liquid HDO and the corresponding hydrogen-bond lengths. However, this absorption spectrum only provides information on the variety of the hydrogen bonds and not on the time scale of the hydrogen-bond fluctuations.

If it were possible to follow the frequency of an individual OH group in time, one would have enough information to calculate the hydrogen-bond length for this OH group at any moment. Time-resolved single-molecule spectroscopy, as this principle is called, is not (yet) possible for molecular vibrations, but it is possible to follow the behavior in time of a *subensemble* of the OH groups with the technique discussed in the next section.

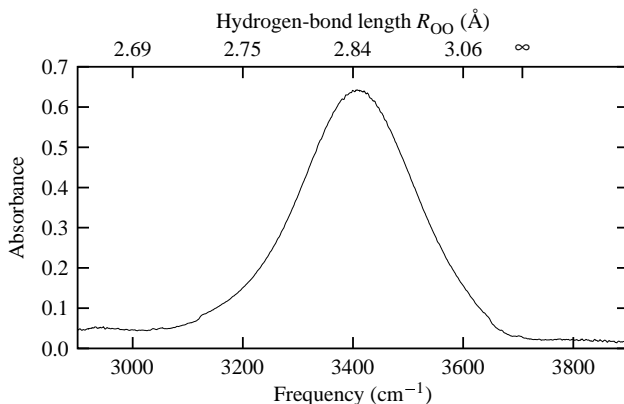


FIGURE I.3. Absorption spectrum of HDO in D₂O, corrected for the absorption of the solvent, D₂O, at an HDO concentration of $\sim 0.4\%$ and a sample thickness of $200\ \mu\text{m}$. In this thesis, the absorbance is defined as $A = -\ln(T)$, where T is the transmittance. (Other literature may also define $A = -\log_{10}(T)$.) On the top axis, approximate hydrogen-bond lengths corresponding to the OH frequencies are given (see also Fig. 8.2 on page 90).

I.2 VIBRATIONAL PUMP–PROBE SPECTROSCOPY

In a pump–probe experiment, a pulse of radiation creates an excitation in a sample, the effect of which is subsequently probed by a second pulse. A historical example of this technique applied on water consists of the nuclear magnetic resonance (NMR) experiments published by Bloembergen in 1948.⁴ He observed that, in a strong magnetic field, the hydrogen nuclei of water could be excited by a ‘pulse’ of 30 MHz radio waves that lasted half a minute. The effect of this excitation remained measurable for several seconds; by filming the screen of his oscilloscope using a movie camera, he was able to determine that the relaxation time of the proton excitation was 2.3 seconds. Over half a century later, we employ pulse durations of 2×10^{-13} seconds (200 fs) in vibrational pump–probe experiments to gain understanding of vibrational relaxation processes that occur on a timescale of 1 picosecond; the movie camera is now replaced by computer soft- and hardware. Vibrational pump–probe spectroscopy is now a technique widely employed, on the OH stretch,^{51,62,65,74,130} the OD stretch,⁷⁸ and the CO stretch.^{49,89,121} In a pump–probe experiment on the OH stretch vibration, a short laser pulse, or pump pulse, excites the OH stretch vibration of a significant fraction of the OH groups in the sample. The result of this excitation is a temporarily decreased absorbance, due to the fact that there are less OH groups left that are still capable of absorbing light.[†] This absorbance change is measured by means of a second, or probe, pulse that passes through the sample with a variable delay t after the pump pulse. Consider the simple case of a thin sample with a concentration ρ of OH groups per unit of surface, each capable of absorbing one photon at a particular

[†] More precisely: in thermal equilibrium, the OH stretch absorption results from the $0 \rightarrow 1$ transition. After excitation, there is still the possibility of absorption due to the $1 \rightarrow 2$ transition, which is generally at a lower frequency. Moreover, a population of the excited state leads to an additional decrease of the apparent $0 \rightarrow 1$ absorption due to stimulated emission caused by $1 \rightarrow 0$ transitions.

resonance frequency ω . The transmittance of such a sample is

$$T_o = e^{-\rho\xi_o\sigma}, \quad (I.1)$$

where σ is the absorption cross-section of an individual OH group (dimension m^2) and $\xi_o = 1/3$ is a geometrical factor to account for the fact that linearly polarized light preferentially excites OH groups that are approximately parallel to its polarization. If a pump pulse at a frequency ω , on resonance with the OH groups, excites N_x molecules per surface unit, then the partially excited sample has a temporarily changed transmittance that is different depending on the polarization ϵ with respect to the pump pulse. This transmittance is $T_\epsilon = \exp([2N_x\xi_\epsilon - \rho\xi_o]\sigma)$, where $\xi_{||} = 3/5$ and $\xi_\perp = 1/5$.[†] The factor 2 results from the fact that both the ground-state depletion and the excited-state population affect the transmittance. A useful quantity is the absorbance change

$$\Delta\alpha_\epsilon \equiv -\ln(T_\epsilon/T_o). \quad (I.2)$$

Because excited molecules typically decay to the ground state with a time constant τ , the absorbance change at time t after the pump pulse becomes

$$\Delta\alpha_\epsilon(t) = -2N_x\xi_\epsilon\sigma e^{-t/\tau}. \quad (I.3)$$

In this simple case, we have assumed that all HDO molecules absorb at the same frequency, which is not very realistic in view of the dependence of the OH stretch frequency on its OH...O hydrogen-bond length. Therefore, we assume a distribution over frequencies that corresponds to a distribution over hydrogen-bond lengths. Let the normalized function $f_d(\omega)$ represent the distribution of HDO molecules over resonance frequencies. Further, $f_{pu}(\omega)$ is the normalized spectrum of the pump pulses, and $f_x(\omega, t)$ the distribution of excited molecules at time t after the pump pulse. Because of the fluctuations in hydrogen-bond lengths, this frequency distribution must be time-dependent in a way that mirrors the length fluctuations. Initially ($t = 0$), only OH groups within the small range of frequencies contained by the pump spectrum are excited, after which this distribution broadens, a process called spectral diffusion or spectral modulation. We assume that every HDO molecule absorbs within a narrow frequency band around a central frequency ω , such that we can describe the cross-section at frequency ω' by the 'cross-section spectrum'

$$s(\omega' - \omega) = \delta(\omega' - \omega)\bar{\sigma}, \quad (I.4)$$

where δ is the Dirac- δ function and $\bar{\sigma} = \sigma / \max[f_d(\omega)]$. We can then write the equivalents of Eqs. (I.1) and (I.3):

$$\alpha_o(\omega) \equiv \ln(T_o(\omega)) = f_d(\omega)\rho\xi_o\bar{\sigma}, \quad (I.5)$$

$$\Delta\alpha_\epsilon(\omega, t) = -2N_x\xi_\epsilon\bar{\sigma}f_x(\omega, t). \quad (I.6)$$

[†]The factors ξ_ϵ result from the fact that vibrational excitations are dipole transitions, whose excitation probability is proportional to $\cos^2(\theta)$, where θ is the angle between the OH bond vector and the polarization of the excitation light. We define σ as the cross-section of an OH group that is exactly parallel to the light polarization. Hence, for an isotropic population, $\xi_o = \int (1/4\pi) \cos^2(\theta) d\Omega = 1/3$, with $\int d\Omega \equiv \int d\phi \int \sin\theta d\theta$. If $g(\theta) = 3 \cos^2(\theta)/4\pi$ describes an anisotropic excited population, $\xi_{||} = \int g(\theta) \cos^2(\theta) d\Omega = 3/5$ and $\xi_\perp = \int g(\theta) \cos^2(\chi) d\Omega = 1/5$. Here, χ is the angle between a vector with polar coordinates (θ, ϕ) and the probe polarization vector $(\pi/2, \pi/2)$ and $\cos(\chi) = \sin(\theta) \sin(\phi)$.

At $t = 0$,

$$f_x(\omega, 0) = f_{\text{pu}}(\omega), \quad (1.7)$$

where we assume that all pump energy is absorbed by the sample [otherwise, multiply by $(1 - T_o(\omega))$].

Equation (1.6) describes the so-called transient spectrum at delay t . Its dependence on frequency and time is the essential ingredient of all pump–probe experiments described in this thesis, because it relates the dynamics of the hydrogen bonds to the time evolution of the absorbance change.

Up to now, we have assumed that the HDO molecules do not significantly change their orientations, which means that the orientation distribution $g(\theta)$ of excited molecules, that results from the polarization of the pump pulse, does not depend on time. With reorientation, $g(\theta)$ is time-dependent, e.g.

$$g(\theta, t) = \frac{1}{4\pi} \left(1 + [3 \cos^2(\theta) - 1] e^{-t/\tau_r} \right), \quad (1.8)$$

where τ_r is known as the rotational correlation time. If reorientation takes place, the geometrical coefficients ξ_{\parallel} and ξ_{\perp} will be time-dependent. An elegant way to circumvent the effect of reorientation is measuring the isotropic absorbance change

$$\Delta \alpha_{\text{iso}}(\omega, t) = (\Delta \alpha_{\parallel} + 2\Delta \alpha_{\perp})/3 = -2N_x \xi_o \bar{\sigma} f_x(\omega, t). \quad (1.9)$$

It can be shown that reorientational processes do not affect $\Delta \alpha_{\text{iso}}$. The isotropic absorbance change can be measured by means of polarizing optics or by simply choosing the polarization of the probe pulses such that the intensities of its parallel and perpendicular polarization components have a ratio 1:2. This ratio is obtained if the angle between pump and probe polarizations is $\arctan(\sqrt{2}) \approx 54.7$ deg, known as the magic angle. Most pump–probe studies in this thesis concern the behavior of the isotropic absorbance change, with the exception of Chapter 7, where we will use the difference between $\Delta \alpha_{\parallel}$ and $\Delta \alpha_{\perp}$ to obtain information on the reorientational dynamics in water. Equations (1.6) and (1.8) are a first approximation; I will discuss some refinements in §2.6.

All pump–probe experiments in this thesis, except for those in Chapter 5, were carried out on dilute HDO in D_2O , with or without dissolved substances. I already mentioned in §1.1 that HDO has a well-defined OH stretch vibration that is only weakly coupled to the OD stretch vibration in the same molecule. Further, the absorbed pump pulse energy is ultimately converted to heat; in a pure H_2O sample, this effect overwhelms any other signal contributions almost completely.⁷⁴ In a dilute HDO in D_2O solution, however, the thermal effects are rather small (§2.8). Finally, the short average distance between OH groups in pure H_2O or in concentrated HDO: D_2O (which contains H_2O as well) enables resonant energy transfer from one OH group to another.¹³⁰ This energy transfer (Förster transfer²⁹ in the limit for long-range interactions) would complicate the analysis.

Finally some remarks on notational conventions. The OH stretch vibration can be treated as quantum-mechanical (hence the distinction between ground-state and excited-state OH groups) with the quantum number ν (vee), that can take the values $0, 1, 2, \dots$, with $\nu = 0$ corresponding to the ground state. In this thesis, I will use the symbol ν exclusively for OH or OD stretch vibrations. Similarly, the symbol R will be used exclusively for the O–O distance of a hydrogen bond. Error margins in experimental values will be denoted in parentheses, e.g. 1.32(2) means 1.32 ± 0.02 .

1.2.1 ABSOLUTE MAGNITUDE OF THE PUMP-PROBE SIGNALS

We can use Eqs. (1.3) and (1.6) to estimate how large the absorbance changes $\Delta\alpha$ will be for given experimental parameters. A pump pulse containing N photons per unit area will excite $N_x = N(1 - T_o)$ molecules, where we assume that $N_x \ll \rho$. If an appropriate HDO concentration and sample thickness are chosen, then $1 - T_o \approx 1$, which is optimal for the sensitivity of the experiment. If the pump pulse has an energy E_{pu} per unit surface, the absorbance change in Eq. (1.3) is

$$\Delta\alpha_\epsilon = \frac{-2E_{pu}\xi_\epsilon\sigma}{\hbar\omega} \quad (1.10)$$

The OH stretch of HDO in D_2O has a cross-section $\sigma \approx 8.0 \times 10^{-23} \text{ m}^2$ (Ref. 135), which can also be estimated from the linear spectrum in Fig. 1.3. For a pump pulse at 3400 cm^{-1} with $E_{pu} = 1 \mu\text{J}$ in a focus of $100 \times 100 \mu\text{m}^2$, we can expect an isotropic absorbance change $\Delta\alpha_{iso} \approx -0.1$. Of course, the pump energy must be contained within a pulse that is shorter than the vibrational lifetime, because most of the excited population would otherwise relax to the ground state before the pump pulse is finished.

If the spectral distribution f_x is to be incorporated, the expression in Eq. (1.10) should be multiplied roughly by the ratio Δ_d/Δ_{pu} , where Δ_d is the width of the linear absorbance spectrum and Δ_{pu} is the width of the pump pulse spectrum. This correction factor holds in the case of spectral modulation that is slow compared to the pulse duration. Otherwise, Eq. (1.10) applies.

In our experience, the observed pump-probe signals are smaller (typically a factor 3) than the estimated signal amplitude, possibly due to geometrical effects in the overlap region of pump and probe pulses. However, it is worth to note that the fraction of excited molecules can be written as

$$\frac{N_x}{\rho} = \frac{-\xi_o\Delta\alpha_\epsilon}{2\xi_\epsilon\alpha_o} \quad (1.11)$$

Thus, a typical sample transmittance $T_o = 0.05$ and an absorbance change $\Delta\alpha_{iso} = -0.1$ imply that only 1.7% of the HDO molecules is excited, which justifies the assumption at the beginning of this section.

1.3 OUTLINE OF THIS THESIS

Pump-probe experiments on water and the resulting information on the dynamics of hydrogen bonds constitute the central theme of this thesis. In Chapter 2, I will discuss the various experimental setups that have been used in the rest of the thesis, along with a practical considerations and additional contributions to the pump-probe signal that have to be taken into account. All experiments were carried out with pulses at wavelengths in the range 2.8–4.2 μm that were generated by means of optical parametric generation and amplification (OPG/OPA), that has become standard practice in time-resolved spectroscopy. However, Chapter 3 discusses a novel way to generate infrared pulses with wavelengths up to 7.2 μm by means of a 4-photon mixing process, which has the potential of being extended to even longer wavelengths.

The following chapters describe experimental pump–probe studies on water. First, Chapter 4 describes the vibrational relaxation of the OH stretch vibration of HDO dissolved in D_2O . Here, the donated $OH \cdots O$ hydrogen bond shows its influence by acting as an acceptor for the vibrational energy. Next, Chapter 5 is concerned with the difference between the OH stretch vibration of HDO in D_2O and the OD stretch vibration of HDO in H_2O . It turns out that the OD stretch vibration is affected by hydrogen-bond dynamics at a timescale somewhat faster than those affecting the OH stretch, but that the lifetime of the OD stretch is significantly longer. In Chapter 6, dissolving sodium deuteroxide ($NaOD$) in $HDO:D_2O$ turns out to have a strong impact on the fluctuations in the hydrogen-bond network. The OD^- ions that are embedded in this network strongly distort its structure, with the result that the fluctuations in the hydrogen-bond lengths become slower by at least an order of magnitude. Returning to $HDO:D_2O$, we will find in Chapter 7 how the orientational motions of water molecules are related to the making and breaking of hydrogen bonds. Finally, in Chapter 8, we use the transient spectrum of excited $HDO:D_2O$ to obtain information on the shape of the potential surface in terms of the OH stretch coordinate and the hydrogen-bond coordinate, which has interesting implications on the mechanism of the autodissociation reaction that is responsible for the fact that pure water has a pH of 7.

2 EXPERIMENTAL DETAILS

2.1 THREE-WAVE MIXING AS AN INFRARED SOURCE

Three-wave mixing is a versatile method for generating short and tuneable pulses at wavelengths ranging from ultraviolet (~ 250 nm) to mid-infrared (up to ~ 10 μm). Examples of three-wave mixing are sum-frequency generation (SFG), second-harmonic generation (SHG), difference-frequency generation (DFG), and optical parametric generation and amplification (OPG and OPA). These techniques^{23,24,27,34,48,56,69,97} are now standard practice in time-resolved spectroscopy. In these processes, oscillating electrical fields at two or three different frequencies are coupled to each other.

In general, the dielectric polarization $P(t)$ at time t in a medium can be written as a power series in the electrical field:

$$P(t) \propto \chi^{(1)}E(t) + \chi^{(2)}E^2(t) + \chi^{(3)}E^3(t) + \dots \quad (2.1)$$

Here, the coefficients $\chi^{(n)}$ are the n -th order susceptibilities of the medium. For any three-wave mixing process, the second-order term is crucial; it is only nonzero in media that have a broken inversion symmetry. If we write

$$E(t) = E_1e^{i\omega_1t} + E_2e^{i\omega_2t} + \text{c.c.}, \quad (2.2)$$

where c.c. denotes the complex conjugate, the second-order term in Eq. (2.1) will read^d

$$P^{(2)}(t) \propto \sum \chi^{(2)} n_o E_1^{n_1} E_2^{n_2} e^{i(m_1\omega_1 + m_2\omega_2)t} + \text{c.c.}, \quad (2.3)$$

where the summation is over

$$(n_o, n_1, n_2, m_1, m_2) = (1, 2, 0, 2, 0), (1, 0, 2, 0, 2), (2, 2, 0, 0, 0), \\ (2, 0, 2, 0, 0), (2, 1, 1, 1, -1), (2, 1, 1, 1, 1). \quad (2.4)$$

The six combinations (n_x, m_x) correspond, respectively, to the second harmonic of E_1 , the second harmonic of E_2 , the optically rectified signals of E_1 and E_2 , the difference frequency, and the sum frequency. A medium that is thus pumped by the fields E_1 and E_2 will radiate a field E_3 with an angular frequency $\omega_3 = m_1\omega_1 + m_2\omega_2$.

Up to now, we ignored the position dependence of the electrical fields. In a typical situation, the electrical fields are traveling waves with an electric field

$$E_j(\mathbf{x}, t) = e^{i(\omega_j t - \mathbf{k}_j \cdot \mathbf{x})}, \quad (2.5)$$

^dWe assume here that $\chi^{(2)}$ is a scalar. In reality, $\chi^{(2)}$ is a tensor whose components depend on the combination of frequencies.¹⁰⁹

at position \mathbf{x} , with the wave vector $\mathbf{k}_j = n(\omega_j)\omega_j/c$, where c is the velocity of light and $n(\omega_j)$ the index of refraction of the medium at angular frequency ω_j . Thus, the second-order polarization angular frequency ω_3 is

$$P^{(2)}(\mathbf{x}, t) \propto E_1^{n_1} E_2^{n_2} e^{i(\omega_3 t - (m_1 \mathbf{k}_1 + m_2 \mathbf{k}_2) \cdot \mathbf{x})}. \quad (2.6)$$

At each position \mathbf{x} , the oscillating second-order polarization radiates at angular frequency ω_3 and a corresponding wave vector $\mathbf{k}_3 = n(\omega_3)\omega_3/c$. Constructive interference, and therefore a high intensity ω_3 field, will occur only if

$$\mathbf{k}_3 = m_1 \mathbf{k}_1 + m_2 \mathbf{k}_2. \quad (2.7)$$

Equation (2.7) is known as the phase *phase matching condition*. Typically, three-wave mixing is done in a birefringent crystalline material (i.e. the index of refraction depends on the polarization and direction of the light that passes through), where the polarizations of the fields and the orientation of the crystal are chosen such that the phase-matching condition is fulfilled. For more details, see for example Refs. 6, 23, 109, 136.

2.1.1 PARAMETRIC GENERATION AND AMPLIFICATION

Optical parametric amplification (OPA) is a special case of difference frequency generation ($\omega_3 = \omega_1 - \omega_2$), where the pump field amplitude E_1 is much larger than E_2 . The field E_3 that is generated causes, in turn, E_2 to increase by the simultaneous DFG process $\omega_2 = \omega_1 - \omega_3$. Because phase matching for the generation of ω_3 implies phase matching for the generation of ω_2 , light at frequencies ω_2 and ω_3 is generated simultaneously. The latter means that in OPA, a photon at frequency ω_1 is ‘split’ into two photons at frequencies ω_2 and ω_3 . The two fields at frequencies ω_2 and ω_3 are usually referred to as signal (the one with the higher frequency) and idler (the lower frequency), and the field at ω_1 is called the pump (not to be confused with the term ‘pump’ in a pump–probe experiment). Parametric generation (OPG) is the limiting case where, initially, $E_2 = E_3 = 0$. Though Eq. (2.3) suggests that second-order polarizations at neither ω_2 nor ω_3 would be generated, the latter does happen in reality, because of quantum-mechanical properties of the electric field. This is, however, beyond the scope of this short summary of three-wave mixing processes. See for example Refs. 6, 109. For all OPG/OPA wavelength conversions that I describe in this thesis, we used specially designed crystals such as β -barium borate (BBO), potassium titanyl phosphate (KTP), lithium niobate (LiNbO₃), and potassium niobate (KNbO₃). These crystals have, due to their crystal symmetry (or the absence thereof), both a nonzero $\chi^{(2)}$ and a strong birefringence, which we employ for phase-matching. In general, the phase-matching can be of ‘type 1’ (pump polarization is perpendicular to both signal and idler), ‘type 2’ (pump and idler polarizations are perpendicular to the signal), or ‘type 3’ (pump and signal polarizations are perpendicular to idler).

The infrared pulses for the time-resolved experiments presented in this thesis were all generated by OPG/OPA processes. However, in Chapter 3, I will discuss a scheme for the generation of infrared pulses by use of a four-wave mixing process, that employs the third-order term in Eq. (2.1).

2.2 PULSE GENERATION FOR PUMP–PROBE EXPERIMENTS

This section treats the methods of infrared-pulse generation that have been used for the experiments in this thesis. In order to study processes that take place on a timescale on the order of one picosecond or less, we need pulses that are (preferably much) shorter than one picosecond. Moreover, in a pump–probe experiment, the pump pulses should be of an intensity that is sufficiently high to induce measurable changes in the absorbance of the sample under study (see §1.2). We have used several different methods of pulse generation, depending on the required wavelengths, on whether or not two simultaneous independently tuneable pulses were needed, and on the available equipment.

2.2.1 TITANIUM-SAPPHIRE AMPLIFIER

The basis of the pulse generation is a commercial titanium–sapphire amplifier, i.e. a laser that delivers pulses at a repetition rate of 1 kHz, a wavelength of ~ 800 nm, and a pulse duration of ~ 100 fs. Two different amplifiers have been used. For the experiments in Chapters 4 and 7, we used a Quantronix 4800 regenerative amplifier with a pulse energy of 1 mJ, a pulse duration of 150 fs full width at half maximum (FWHM), and a wavelength centered at 800 nm. For the experiments in the remaining chapters, we used a Quantronix Titan regenerative/multipass amplifier with a pulse energy of 3 mJ, a pulse duration of 100 fs (FWHM), and a wavelength centered at 805 nm.

2.2.2 TOPAS: A BBO-BASED OPG/OPA DEVICE

A common element for our pulse generation is the TOPAS. This is a commercial device (manufacturer: Light Conversion, Ltd.) that converts the 800 nm pulses from the Ti:sapphire amplifier to longer wavelengths through a type-2 OPG/OPA (§2.1.1) process. It uses a β -barium borate (BBO) crystal as the nonlinear medium. The output pulses are tunable in the range 1140–1600 nm (signal) and 1600–2650 nm (idler). The wavelength tuning range for both signal and idler is limited by absorption in the BBO crystal of (idler) wavelengths beyond 2500 nm. Since spectroscopic experiments on the OH stretch vibration require wavelengths in the range 2850–3600 nm, additional conversion steps are necessary. A direct conversion by use of a crystal such as KTP (see following sections) instead of BBO is not possible, because it would not survive the high pump intensity required by the first (OPG) step in the conversion.

2.2.3 PULSE GENERATION ($\sim 3 \mu\text{M}$) FOR ONE-COLOR EXPERIMENTS

This section describes the pulse generation for the experiments in Chapters 4 and 7. In these experiments, pump and probe pulses had equal frequencies, hence the name ‘one-color’.

The method of pulse generation is depicted schematically in Fig. 2.1. A Ti:sapphire amplifier (§2.2.1) pumps a Topas OPG/OPA device (§2.2.2). We tuned the Topas to generate a signal wavelength of 1140 nm, with an FWHM bandwidth of 80 nm. The spectrum of this signal contains sufficient intensity at a wavelength of 1090 nm in order to act as a seed for a second OPA process in a potassium titanyl phosphate (KTP) crystal, that is pumped by the remaining 800 nm light. This second OPA process generates a signal at approximately

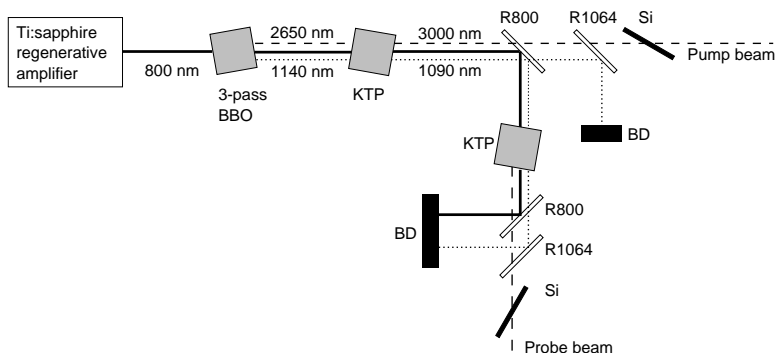


FIGURE 2.1. Generation of mid-infrared pulses for one-color experiments and some of the two-color experiments. Abbreviations: BBO: BBO crystal; KTP: KTP crystal; R800: dielectric 800 nm mirror; R1064: dielectric 1064 nm mirror; Si: silicon Brewster window; BD: beam dump. The probe branch was only used for the experiments in Chapter 4.

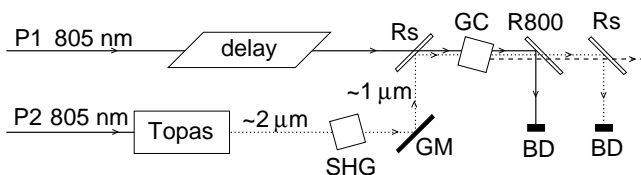


FIGURE 2.2. Pulse generation for §2.2.4 and §2.2.5. Abbreviations: Topas, commercial OPG/OPA device; SHG, second harmonic generation crystal (BBO); GM, gold mirror; Rs, dichroic signal-reflecting mirror; GC, IR-generating crystal (KTP, LiNbO₃, or KNbO₃); R800, dielectric 800-nm mirror. Pump pulse energy at P1, P2 varies; see §2.2.4 and §2.2.5.

1090 nm and an idler at approximately 3000 nm. By changing the phase-match angle of the KTP crystal, the idler wavelength can be continuously tuned up to 3300 nm with an energy of typically 20 μJ , a bandwidth of 80 nm and an FWHM duration of 250 fs. This wavelength range corresponds to frequencies larger than 3000 cm^{-1} , which is suitable for exciting and probing the O–H stretch vibration in water. The remaining 800-nm pump and signal wavelength components are removed by means of dielectric 800 and 1064 nm mirrors. Any remaining short wavelength components are filtered out by a silicon plate positioned at the Brewster angle. This method of infrared pulse generation is described in more detail in Ref. 27. To obtain a probe pulse, we used a reflection from a wedged calcium fluoride window.

2.2.4 PULSE GENERATION ($\sim 3 \mu\text{M}$) FOR TWO-COLOR EXPERIMENTS

In the two-color experiments described in Chapter 4, the pump pulses were generated as described in §2.2.3. Part of the seed and the remaining energy of the 800 nm pulses were combined in a second KTP crystal for an independently frequency-tunable probe pulse with an energy of $< 1 \mu\text{J}$.

In the two-color experiments described in Chapters 6 and 8, the pump and probe

pulses were generated in two completely independent branches. Each branch was set up as in Fig. 2.2. A Topas device (§2.2.2), pumped at 805 nm, delivered idler pulses around $2.2 \mu\text{m}$, which were frequency-doubled in a BBO crystal. The resulting $1.1\text{-}\mu\text{m}$ pulses served as a seed in a type-2 OPA process (§2.1.1) in a 5-mm KTP crystal that was pumped by an independent 805 nm pulse. After the KTP crystal, dielectric mirrors and a long wave pass filter filtered out the remaining 805 nm and signal light. In the pump-pulse branch, the energies of the 805-nm pulses were 0.8 mJ (P1) and 1.3 mJ (P2), which resulted in typical energies of the generated pulses near $3 \mu\text{m}$ of $10\text{--}20 \mu\text{J}$. In the probe-pulse branch, they were 0.45 mJ (P1) and 0.11 mJ (P2), yielding $\sim 1 \mu\text{J}$ of pulse energy. Compared to the method described in §2.2.3, this method offers a much better pulse stability. Typically, the $3 \mu\text{m}$ pulses had a bandwidth of $80\text{--}120 \text{ nm}$ ($80\text{--}100 \text{ cm}^{-1}$) FWHM and a duration of $200\text{--}250 \text{ fs}$ (§2.5).

2.2.5 PULSE GENERATION AT $\sim 4 \mu\text{M}$

This section describes the pulse generation for the experiments in on the OD stretch vibration Chapter 5. The OD stretch vibration has typically a frequency of 2500 cm^{-1} , which corresponds to wavelengths around $4 \mu\text{m}$. The pump and probe pulses were generated independently from each other.

PUMP PULSES Figure 2.2 shows the pump-pulse generation setup, which is very similar to that described in §2.2.4. Here, the Topas device (§2.2.2) was pumped with 0.9 mJ pulses and generated idler pulses at a slightly shorter wavelength, around $2.0 \mu\text{m}$. For the parametric amplification, we used a 5-mm KNbO₃ crystal, which is more suitable than KTP for the wavelength range $3.7\text{--}4.25 \mu\text{m}$. The pulses typically had energies of $18 \mu\text{J}$ and bandwidths of 70 nm (44 cm^{-1}) FWHM.

PROBE PULSES We employed two different techniques for probe pulses at wavelengths below and above $4.25 \mu\text{m}$. Below $4.25 \mu\text{m}$, the technique is similar to that for generating the pump pulses, as described in the previous section, but with smaller pulse energies and a LiNbO₃ crystal instead of a KNbO₃ crystal. With LiNbO₃, the spectral shape and pulse energies of the generated light were more stable than with KNbO₃. It was pumped with 0.1 mJ 805 nm light. Cross-correlation traces of these pulses with the pump pulses (delay-dependence of sum-frequency generation in a LiIO₃ crystal), had FWHMs of 350 fs and bandwidths of $50\text{--}110 \text{ nm}$ ($30\text{--}70 \text{ cm}^{-1}$).

Wavelengths longer than 4250 nm are absorbed by LiNbO₃, which imposed the need of an alternative pulse generation technique. For these longer wavelengths, we tuned the Topas to generated pulses at $1.36 \mu\text{m}$ (signal) and $1.97 \mu\text{m}$ (idler). The signal and idler pumped a DFG (§2.1) process in a 3-mm AgGaS₂ crystal, which generated pulses with a wavelength of $4.40 \mu\text{m}$. In this case, cross-correlation traces of these pulses with the pump pulses had an FWHM of 600 fs and a bandwidth of 166 nm (85 cm^{-1}).

2.3 SAMPLE

We conducted most pump-probe experiments described in this thesis on samples that consist of a thin ($200\text{--}500 \mu\text{m}$) layer of liquid sandwiched between two 4-mm-thick CaF₂

windows. Calcium fluoride combines a number of properties that make it very suitable for this purpose: it is transparent up to a wavelength of $\sim 8 \mu\text{m}$ (1250 cm^{-1}), practically insoluble, reasonably easy to handle, and not birefringent (which is relevant since the relative polarizations of pump and probe pulses affect the outcome of the experiment). Only for the experiments at low temperatures, described in Chapter 4, we used sapphire windows. Because sapphire is birefringent, we used windows with the optical axis perpendicular to the surface. If the laser pulses do not have a normal angle of incidence, the birefringence still affects the polarization of the pulses. For a small external angle of incidence $\theta = 0.075 \text{ rad}$, a window thickness $L = 3 \text{ mm}$, an ordinary refractive index $n_o = 1.7$,^{58,79} an extraordinary refractive index $(1 + \epsilon)n_o$ with $\epsilon = 0.0011$,[†] and a wavelength (*in vacuo*) $\lambda = 3 \mu\text{m}$, the introduced phase difference between horizontal (p) and vertical (s) polarizations is

$$\Delta\phi \equiv \phi_p - \phi_s \approx \frac{2\pi L \theta^2 \epsilon}{n_o \lambda} = 0.022. \quad (2.8)$$

See for example Refs. 6, 136 for an explanation on calculating effective indices of refraction in birefringent media. For linearly polarized light at an angle of 45 deg (equal p and s components), this phase difference will introduce a polarization component perpendicular to the original polarization with an intensity $\sin^2(\Delta\phi/2) \approx 10^{-4}$ relative to the original intensity, which can safely be neglected. Moreover, in a typical experimental geometry, only the ratio of the intensities of the p and s components is relevant, which is not affected by a phase retardance. (Similarly, any p–s phase differences caused by mirrors can be ignored.)

In the measurements as a function of temperature, described in Chapter 4 and 7, it was important to have a well-defined temperature in the sample. For that reason, we used a construction that rotates the sample in a plane parallel to the sample windows, such that a fresh part of the sample was probed for each laser shot. This limited the temperature error to the effect of one pump pulse, which we can estimate to be less than 0.2 K, assuming that $20 \mu\text{J}$ of energy are homogeneously dissipated in the $200^2 \times 500 \mu\text{m}^3$ focus. We used the rotating sample cell for the experiments in Chapter 5 as well, because the thinner, i.e. $50 \mu\text{m}$, sample would suffer from a larger temperature increase for the same amount of dissipated pump pulse energy. In §2.8, I will discuss the effect the pump pulses heating the sample for a nonmoving sample.

2.4 PUMP–PROBE SETUP

I described the physical principles of a pump–probe experiment in Section 1.2. This section is concerned with the practical details. Two slightly different setups have been used, a two-color setup (Chapters 5, 6, and 8) and a one-color, polarization-resolved setup (Chapters 4 and 7).

[†]No literature data for the birefringency of sapphire are available. This value applies to ruby (which is very similar) at 707 nm.⁵⁸

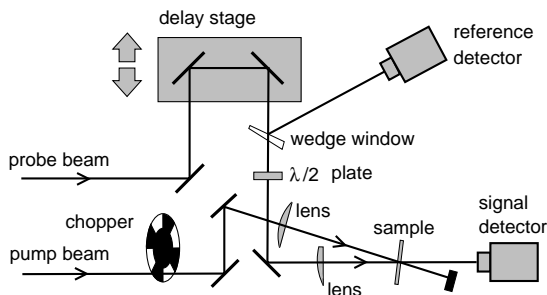
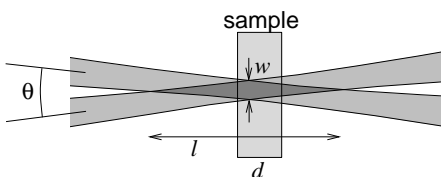


FIGURE 2.3. Pump-probe setup for the experiments in Chapters 5, 6 and 8. The $\lambda/2$ plate rotates the probe pulse polarization to the magic angle (54.7 deg) with respect to the pump pulse polarization.

FIGURE 2.4. Intersection region of the pump and probe beams in the sample. The sample is shown without the sample windows.



2.4.1 TWO-COLOR SETUP

Figure 2.3 shows the two-color pump-probe setup. Calcium fluoride lenses focus the pump and probe pulses into an overlapping region in the sample. A translation stage enables varying the time delay between the pump and probe pulses. A PbSe photoconductive detector measures the energy E_p of the probe pulses after they have passed through the sample; another detector registers, as a reference, the energy of a small fraction of the probe pulse energy E_r that has reflected off a calcium fluoride window. A chopper blocks every other pump pulse, which enables measuring the pulse energies E_p° and E_r° without the effect on the sample of a pump pulse. Thus, the absorbance change

$$\Delta\alpha = -\ln \frac{T}{T^\circ} = -\ln \left(\frac{E_p E_r^\circ}{E_r E_p^\circ} \right) \quad (2.9)$$

is measured as a function of the delay between pump and probe pulses. Around zero delay, we typically achieved $|\Delta\alpha| \approx 0.1$ at 10–20 μJ pump pulse energy.

A zero-order quartz $\lambda/2$ plate rotates the polarization of the probe pulse to the magic angle $\arctan(\sqrt{2}) = 54.7$ deg with respect to the pump pulse polarization. Due to this angle, the reorientational motions of the excited molecules do not affect the absorbance change.

The geometry of the lenses and the sample thickness are a compromise between several considerations. The beam waist diameters w in the pump and probe beam foci and the angle θ between the pump and probe beams lead to an intersection region with a length $l \approx 2w/\theta$ as in Fig. 2.4. Refraction by a sample with index of refraction n will affect both w and θ by a factor $\approx 1/n$, which means that one can substitute the values for w and θ as obtained in air. Since the excitation by the pump pulse temporarily changes the optical

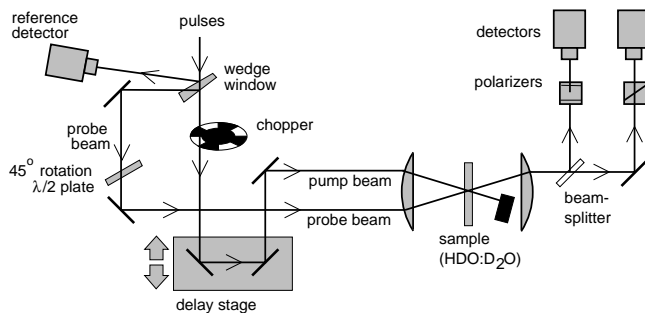


FIGURE 2.5. Pump-probe setup for the experiments in Chapters 4 and 7. In the two-color experiments in Chapter 4, the probe polarization was at the magic angle (54.7 deg), no polarizers were used, and only one detector was placed behind the sample.

properties in the focal region, the probe pulse may not only be partially absorbed, but may also be focused or defocused (due to both diffraction and a change in the index of refraction) compared to the case where no pump pulse was present. This (de)focusing can affect the measured absorbance changes. Therefore, it is important that the probe pulse does not ‘experience’ a strong spatial variation of the optical properties of the sample. From the figure, it is clear that, in order to avoid such edge effects, the length d of the sample should be much shorter than the intersection length l . Also, it is better if the probe beam waist is narrower than the pump beam waist. Further, the necessary angle between the pump and probe beams causes the time resolution to become worse, by roughly $\Delta\tau \approx w\theta/c$. (See Ref. 139 for a detailed calculation.)

In the setup, the lenses have focal lengths of 170 mm (pump) and 100 mm (probe). This results in focal waists of about 100 μm , i.e. typically, 60% of the pump pulse energy and 80% of the probe pulse energy pass through a pinhole with a diameter of 100 μm . With a beam angle $\theta = 0.1$ rad inside the sample, we can estimate that $l \approx 2$ mm and $\Delta\tau \approx 30$ fs. In most experiments, the sample length was $d = 200$ μm . Much shorter lengths would have the disadvantage of a more significant effect of temperature increase as a result of the dissipation of the pump pulse energy (see §2.8). The effect on the time resolution is of minor importance for the pulse durations of typically 200–250 fs in our experiments.

2.4.2 ONE-COLOR POLARIZATION-RESOLVED SETUP

Figure 2.5 shows the pump-probe setup used in the experiments of Chapters 4 and 7. It differs from the setup in §2.4.1 in that the probe pulse is a small fraction of the pump pulse instead of a separately generated pulse, and in that the setup is polarization-resolved. For this purpose, a zero-order quartz $\lambda/2$ plate rotates the probe polarization to 45 deg with respect to the pump pulse polarization. By means of a beamsplitter and two rutile (TiO₂) polarizers, the polarization components parallel and perpendicular to the pump pulse polarization are measured separately. Thus, absorbance changes $\Delta\alpha_{\parallel}$ and $\Delta\alpha_{\perp}$ are measured, from which the isotropic absorbance change and the rotational anisotropy can be calculated. Section 2.7.1 describes how the probe pulse polarization can be extracted

efficiently. In this setup, the focus of the pump and probe pulses is somewhat larger than in the two-color setup of §2.4.1 because a single $f = 100$ mm CaF₂ lens focuses both the pump and probe pulses into the sample. Here, we used 500 μm thick samples of an HDO in D₂O solution.

2.5 PULSE CHARACTERISATION

The most important properties of the pulses that were used to carry out the experiments are their duration and their spectrum. Before each pump–probe experiment, we recorded power spectra of both pump and probe pulses using a scanning monochromator (Oriel model MS257) and a PbSe detector. The PbSe detectors and the reflection coefficient of the grating in the monochromator did not have a completely flat frequency response, for which we did not correct. The latter has a minor effect on the measured spectrum, since the frequency response does not vary significantly across an individual power spectrum, which is typically 100 cm^{-1} wide.

In a scan of pump–probe signal versus delay, the instrument function is the correlation function

$$C(t) = \int_{-\infty}^{\infty} I_{\text{pu}}(t')I_{\text{pr}}(t+t')dt' \quad (2.10)$$

of the pump and probe pulses, where $I_{\text{pu}}(t)$ and $I_{\text{pr}}(t)$ are the time-dependent intensities of the pump and probe pulses. We obtained these cross-correlates using the following two methods.

1. Sum-frequency generation (SFG) in a LiIO₄ crystal. The sample was replaced by a LiIO₄ crystal; the overlapping foci of the pump and probe pulses generated sum-frequency light in the case of time-overlap (see §2.1), the intensity of which was detected as a function of delay. This method is accurate, but it has practical disadvantages in the typical situation that pump–probe and cross-correlate measurements are carried out interleaved. The phase-matching for SFG requires polarizations of the pump and probe pulses that are different from in a pump–probe measurement. Due to this phase-matching, the sum-frequency light is emitted in a direction different from the that of the probe pulses, which requires displacing the detectors from their position in a pump–probe experiment. Moreover, the fact that the sum-frequency light has a shorter wavelength than the probe pulses requires replacing spectral filters.
2. Two-photon absorption in germanium. Germanium is transparent for frequencies below 5000 cm^{-1} (Ref. 58) due to its band gap. However, at high intensities, electrons can get excited from the valence band to the conduction band via a two-photon process. If the pump and probe have relatively low intensities, causing only a small amount of two-photon absorption, then it can be shown that the transmittance change $T(t)/T_0 - 1$ of the probe pulses is negative and proportional to $C(t)$. Here, T_0 is the transmittance of the probe pulse in absence of pump pulses. Typically, this technique requires reducing the pulse energies of both pump and probe to ~ 100 nJ. This technique has the advantage of being quick: it requires only replacing the liquid sample by a germanium plate and it does not require adjusting the phase-matching angle. Further, two-photon absorption at high pump intensities creates a population of the

conduction band that causes an increase in absorbance that lasts for many nanoseconds, which enables the experimenter to find the time overlap very rapidly—contrary to sum frequency generation, where both the delay zero point and the phase-matching angle must be adjusted simultaneously in order to obtain any signal. Its disadvantage is a somewhat lower signal-to-noise ratio.

The liquid samples were typically 200 μm thick. Both of the above techniques have the disadvantage that the overlap region (§2.4.1) in the sample is different from that in germanium or LiIO_4 , which are 500 μm and 2 mm thick, respectively. Not only the different lengths of the overlap regions matter, but also the fact that the sample liquid and the cross-correlation material have different dispersive properties. Especially if the pump and probe frequencies are different, dispersion due to different group velocities of the pump and probe introduces an error. Because of this dispersion, we used the cross correlates only to determine the pulse duration and not for the exact delay zero point. In the two-color studies in chapters 5 and 6, the delay zero point was a parameter in the fit procedure. The difference $\Delta t_o = t_{\text{fit}} - t_{\text{cc}}$ between the delay zero points t_{fit} from this fit and t_{cc} from the cross correlate in germanium is roughly proportional to the difference $\Delta\omega = \omega_{\text{pr}} - \omega_{\text{pu}}$ between probe and pump frequencies. The proportionality constant is $\Delta t_o / \Delta\omega \approx 0.78 \text{ fs/cm}^{-1}$ for $\omega_{\text{pr}}, \omega_{\text{pu}}$ in the range 3000–3600 cm^{-1} . We used this relation in Chapter 8.

2.6 REFINEMENTS OF THE PUMP–PROBE SIGNAL DESCRIPTION

The description in §1.2 of vibrational pump–probe signals is a first approximation. An accurate analysis of experimental data requires taking into account a number of additional effects that we have skipped in §1.2. The following list outlines the typical effects that are significant in the studies in this thesis.

1. The pump and pulses are not infinitely short. For realistic pulse durations, we must convolve the signal $\Delta\alpha_\epsilon$ with the instrument response function $C(t)$ described in §2.5.
2. The absorbance change is not measured exactly at frequency ω , but within a frequency distribution defined by the spectrum $f_{\text{pr}}(\omega)$ of the probe pulse. If we assume that $\Delta\alpha \ll 1$ and that the variation of the absorbance $\alpha_o(\omega)$ [Eq. (1.5)] is $\ll 1$ within the probe pulse spectrum, then we can write the experimental pump–probe signal as

$$\Delta\bar{\alpha}_\epsilon(t) = \int d\omega' f_{\text{pr}}(\omega') \int dt' \Delta\alpha_\epsilon(\omega', t - t') C(t'), \quad (2.11)$$

which incorporates point 1 as well.

3. The cross-section spectrum $s(\omega' - \omega)$ of an individual OH group is not an infinitely narrow δ function that peaks at frequency ω , but has a certain width, known as the homogeneous linewidth. For optically thin samples, it can be shown that homogeneous broadening is equivalent to replacing the pump and probe spectra by the convolutions $F_{\text{pr,pu}}(\omega) = f_{\text{pr,pu}}(\omega) * s(\omega)$.

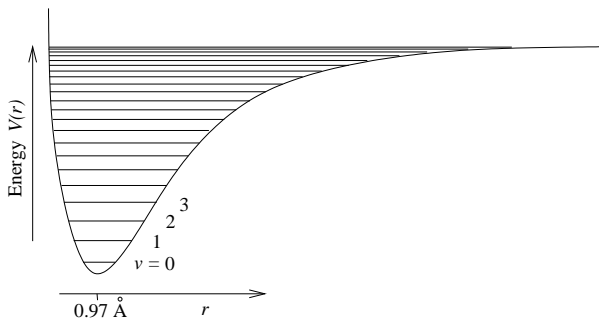


FIGURE 2.6. Schematic potential of the OH stretch vibration, as a function of the O–H distance r . The distance between subsequent energy levels decreases with increasing quantum number ν . This potential applies to gas phase OH groups that have no hydrogen-bonds interactions. The case with hydrogen bonds is discussed in Chapter 8.

4. The excited state and the ground state have different spectra. Typically, subsequent energy levels of a molecular vibration are not spaced uniformly, as is shown in Fig. 2.6, which means that the presence of excited OH groups results in a negative absorbance change (bleaching) at the frequency corresponding to the $\nu = 0 \rightarrow 1$ transition, and in a positive absorbance change (induced absorbance) at the frequency corresponding to the $\nu = 1 \rightarrow 2$ transition. The frequency difference is called the anharmonic redshift $\delta\omega_{\text{anh}}$, which has a value of 270 cm^{-1} (Ref. 45 and Chapter 8). Further, the relation between the hydrogen bond and the OH stretch frequency causes the $\nu = 1$ population to contribute to the bleaching at a slightly different frequency than the depletion of the $\nu = 0$ population. This Stokes shift will be discussed in detail in Chapter 5 and will be used in later chapters. Finally, the value of the anharmonic redshift is in a complicated manner related to the hydrogen-bond interactions, an issue that is treated in Chapter 8.
5. The linear relationship [Eq. (1.6)] between the excited-state population $f_x(\omega, t)$ and the absorbance change $\Delta\alpha_\epsilon(\omega, t)$, corrected for the pulse duration and bandwidths (points 1 and 2) only holds if the time evolution of f_x is relatively slow. Slow means that $\tau_c\Delta_m \gg 1$, where Δ_m is the bandwidth over which spectral modulation occurs and τ_c is the correlation time of the spectral modulation. Except for Chapter 7, the studies in this thesis assume the limit $\tau_c\Delta_m \gg 1$.[♯]

The above refinements are in a sense trivial and will be used during the analysis of the experiments when necessary. However, there are two effects that must be described in a different language. Around $t = 0$, the temporal overlap between the pump and probe pulses can cause contributions to the pump–probe signal that are not described by Eq. (1.6). Because these extra signals are only indirectly related to the dynamics of the OH groups, and because they depend in a complicated way on parameters that may or may

[♯]For $\tau_c\Delta_m \lesssim 1$, the spectral width of $\Delta\alpha_\epsilon$ would be smaller than the width of f_x . For $\tau_c\Delta_m \ll 1$, the system becomes homogeneously broadened (item 3). We assume here that spectral modulation can be interpreted as an oscillating spring whose force constant is randomly modulated, without jumps in the phase of the oscillation. See for example Buhrstein¹³ for a theoretical treatment on the effects of various types of spectral modulation.

not be known, these extra signal contributions are often referred to as *artifacts*.

6. The *coherent artifact*, that occurs when the pump and probe pulses have overlapping spectra and that appears as a narrow (less than the pulse duration) peak centered at $t = 0$. During time overlap, the simultaneous presence of the pump and probe fields causes an interference pattern in the sample and hence a corresponding spatial pattern of the sample transmittance. The latter acts as a grating that diffracts pump light into the propagation direction of the probe beam, thus causing an additional negative contribution to $\Delta\alpha$. The effect (i.e. the product of amplitude and duration of the artifact) is strongest when strongly coherent (Fourier transform limited) pulses are used. The magnitude of the effect may be calculated, but the calculation is rather involved and requires knowledge about the spectral broadening mechanisms and the degree of coherence of the laser pulses.^{88,131} It appears, however, that the coherent artifact is not very significant in the experiments described in this thesis. For example, the transient spectra of HDO:D₂O in Chapter 8 can be described without incorporating a coherent artifact.
7. The *cross-phase modulation (XPM) artifact*, in which the spectrum of the probe pulses changes slightly due to the simultaneous presence of the electric field of the pump pulse. The index of refraction effectively changes slightly due to the presence of the intense pump field. This coupling is called the optical-field-induced birefringence.¹⁰⁹ Depending on whether this change occurs predominantly in the head (delay $t < 0$) or tail ($t > 0$) of the probe pulses, the result is a small shift $\delta\omega_{\text{pr}}(t)$ of the spectrum that is negative or positive, respectively. Equation (30) in Ref. 60 describes the relative change in spectral intensity for the case of transform-limited pump and probe pulses that applies to the typical pump intensities in the experiments in this thesis, but is limited to cases with negligible differences in group velocity between pump and probe (e.g. $|\omega_{\text{pu}} - \omega_{\text{pr}}| < 100 \text{ cm}^{-1}$). At higher pump intensities, or with significant group-velocity differences between pump and probe (as is the case with two-color experiments), a numerical approach is necessary to calculate the XPM artifact.²⁶ Cross-phase modulation can occur both in the sample and in the sample window before the sample (in the window behind the sample, the pump intensity is too low to be significant). The amplitude of the XPM artifact depends further on the coupling constant (i.e., one of the tensor elements of $\chi^{(3)}$) in the windows and in the sample medium and on the geometry of the spatial overlap region of the pump and probe beams. In the experiments in this thesis, the maximum amplitude of the shift $\delta\omega_{\text{pr}}$ is small ($< 2 \text{ cm}^{-1}$ as measured in CaF₂), but if the transmittance of the sample changes steeply with frequency, the result is that the spectrally shifted pulse undergoes a different attenuation different from what the original pulse would have had. For narrow pulse spectra, we can approximate the XPM contribution to the absorbance change $\Delta\alpha$ as

$$\Delta\alpha_{\text{XPM}}(\omega, t) = \frac{d\alpha_o}{d\omega} \delta\omega_{\text{pr}}(t) \quad (2.12)$$

where ω is the probe frequency and α_o is the linear absorption spectrum [Eq. (1.5)]. Because of the large number of parameters whose values are difficult to obtain, the exact magnitude is difficult to calculate, but if group velocity dispersion can be neglected,

$\delta\omega_{\text{pr}}$ has a behavior similar to

$$\delta\omega(t) \approx kE_{\text{pu}}g'(t), \quad (2.13)$$

where g' is the derivative of a Gaussian with unit amplitude and a width comparable to the width of the instrument function $C(t)$ (§2.5) and k is a proportionality constant. It is clear that the XPM artifact will be reduced if the absorbance of the sample is not chosen too high: the artifact contribution $\Delta\alpha_{\text{XPM}}$ is proportional to the sample absorbance $\Delta\alpha_0$, while the pump–probe signal is proportional to $1 - T_0 = 1 - \exp(-\alpha_0)$. Further, the XPM artifact is especially significant if the desired bleaching signal is very weak.

In principle, pump–probe signals can be described with a much more rigorous mathematical formalism,^{8,88} which incorporates the effects under points 1–3, 5, and 6. Because the coherent artifact is a natural result of this formalism, the term ‘artifact’ is sometimes considered inappropriate. However, that the formalism is more rigorous cannot compensate for the fact that it depends on the same unknown or difficult to obtain parameters under 3, 5, and 6. Even very general expressions for a pump–probe signal, that can only be evaluated after some approximations, depend on some assumptions that tend to be obscured by the mathematical details.

2.7 NOISE SUPPRESSION

The parametric generation and amplification process that we use to obtain infrared pulses, is inherently a source of noise in the signals being measured. Since the conversion process depends highly nonlinearly on the energy of the pump pulses, any fluctuations in the 800-nm pump energy show up as large variations in the energy of the infrared pulses at $3\ \mu\text{m}$. It is not uncommon to observe an individual pulse energy that differs by 30% from the average pulse energy. In addition, the power spectrum and the beam profile can vary slightly from pulse to pulse. Finally, in an experiment where the sample is rotated to reduce the effects of accumulated local heating, a small inhomogeneity, e.g. in the thickness, of the sample may cause the sample transmittance to oscillate with a few Hertz. Hence, it is important to design the experiment such that an optimal signal-to-noise ratio is achieved. I will discuss two limiting cases.

2.7.1 UNCORRELATED NOISE

Uncorrelated noise is noise of a completely random nature that varies randomly from pulse to pulse and possibly from detector to detector. This may originate from fluctuations in the pulse energy or from the detector electronics. In order to correct for energy fluctuations, we use one detector to measure the energies of the pulses in the reference beam. In the case of the laser shots where a pump pulse is present, this yields reference energies r_i , where the subscript $i = 1, \dots, N$ indicates the individual pulses. A detector behind the sample acquires the energies p_i of the probe pulses. For the laser shots without a pump pulse, the energies are r_i° and p_i° . The corresponding transmittances are $T_i = p_i/r_i$ and $T_i^\circ = p_i^\circ/r_i^\circ$. (Formally, this is not correct if the detectors have different efficiencies.

However, this does not affect the ratio T_i/T_i° .) Commonly, the absorbance change is calculated as $\Delta\alpha = -\ln(\langle T_i \rangle / \langle T_i^\circ \rangle)$ or $\Delta\alpha = -\ln(\langle T_i/T_i^\circ \rangle)$. Unfortunately, any noise in the detector signals will affect the ratio p_i/r_i more strongly for pulses with a weaker energy. In these equations, all laser shots are assigned equal weights, which causes excessive noise in $\Delta\alpha$ due to pulses with low energies. Therefore, we calculate $\Delta\alpha = -\ln(T/T^\circ)$, where T and T° result from a linear least-squares fit of $p_i = Tr_i$ and $p_i^\circ = T^\circ r_i^\circ$ to the data, as is shown in Fig. 2.7. If we assume that the error is unknown, but equal for each data point, a linear least squares fit of the parameter T in $p = Tr$ results in

$$T = \frac{\sum_i p_i^2}{\sum_i r_i p_i}, \quad (2.14)$$

$$\sigma_p = \left(\frac{\sum_i p_i^2 + 2T \sum_i r_i p_i + T^2 \sum_i r_i^2}{N-1} \right)^{\frac{1}{2}}, \quad (2.15)$$

$$\sigma_T = \sigma_p / \sqrt{\sum_i r_i^2}, \quad (2.16)$$

where σ_T and σ_p are the errors in T and in p , respectively. These result from the assumption that a good error estimate should result in

$$\chi^2 \equiv \sum_i \sigma_p^{-2} (p_i - Tr_i)^2 \approx N-1. \quad (2.17)$$

Using Eq. (2.14) leads to a strong reduction in the noise in $\Delta\alpha$ compared to the more naïve methods mentioned in the beginning of this section.

In polarization-resolved experiments (Chapter 7), separate detectors measure the probe pulse energies for parallel and perpendicular polarizations, which results in $\Delta\alpha_{\parallel}$ and $\Delta\alpha_{\perp}$ from the same procedure as above. In the polarization-resolved experiments, we measured the quantity

$$A = \frac{\Delta\alpha_{\parallel} - \Delta\alpha_{\perp}}{\Delta\alpha_{\parallel} + 2\Delta\alpha_{\perp}}. \quad (2.18)$$

In this case, we can reduce the noise even more by observing that, for a single laser shot, we can write the numerator as

$$\Delta\alpha_{\parallel,i} - \Delta\alpha_{\perp,i} = -\ln \left(\frac{p_{\parallel,i}}{p_{\perp,i}} \cdot \frac{p_{\perp,i}^\circ}{p_{\parallel,i}^\circ} \right). \quad (2.19)$$

which is now not influenced by any noise in the reference signals r_i . Using similar arguments as for T/T° , we calculate the quantities D and D° , that represent the ratios of the signals measured by the parallel and perpendicular detectors, by fitting the functions $p_{\parallel} = Dp_{\perp}$ and $p_{\parallel}^\circ = D^\circ p_{\perp}^\circ$. We can now express the rotational anisotropy [Eq. (2.18)] as

$$A = \frac{-\ln(D/D^\circ)}{\Delta\alpha_{\parallel} + 2\Delta\alpha_{\perp}}. \quad (2.20)$$

We found that the above techniques improved our signal-to-noise ratio by almost an order of magnitude, compared to mere averaging of the detector responses.

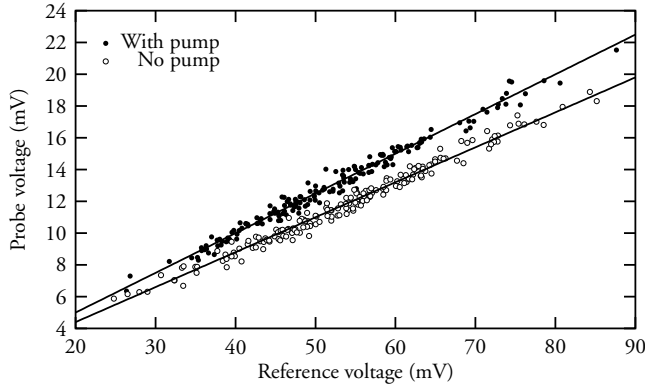


FIGURE 2.7. Typical detector responses for the component of the probe polarization that is parallel to the pump polarization. The lines are linear least-squares fits to the data, with slope $T = \sum_i p_{w,i} r_i / \sum_i r_i^2$ (similar for T_o).

2.7.2 TIME-CORRELATED NOISE

In the case where the laser shows slow fluctuations or the sample transmittance fluctuates due to an inhomogeneous sample that is rotated, the method in §2.7.1 is not optimal. Typically, we handle data sets with size $N \sim 10^3$ points that are acquired during a few consecutive seconds. Equation (2.14) ignores the fact that the sample transmittance is nearly equal for two consecutive laser shots—the sample rotates with a frequency of typically about 2 Hz. On the other hand, we can expect that the quantity of interest, $A \equiv T/T_o$, does not depend significantly on the sample transmittance T_o . In this case, it is better to calculate A and its error σ on a shot-per-shot basis:

$$A_i = \frac{p_i r_i^o}{r_i p_i^o}, \quad (2.21)$$

$$\sigma_i = \frac{\sigma_p r_i^o}{(p_i^o)^2 r_i} \sqrt{(p_i^o)^2 + p_i^2}. \quad (2.22)$$

Here, σ_p is the (yet unknown) error in each individual probe pulse energy p_i or p_i^o ; Eq. (2.22) results from standard error propagation in Eq. (2.21). The best estimate $\langle A \rangle$ is now the weighted average

$$\langle A \rangle = \frac{\sum_i \sigma_i^{-2} A_i}{\sum_i \sigma_i^{-2}}, \quad (2.23)$$

with an error

$$\tilde{\sigma}_{\langle A \rangle} = \frac{1}{\sqrt{\sum_i \sigma_i^{-2}}}. \quad (2.24)$$

The tilde indicates that this error is still dependent on the per-shot error σ_p . We can eliminate this by assuming $\sigma_p = 1$ (or any other value) and then calculating the statistical quantity

$$\chi^2 = \sum_i \sigma_i^{-2} (A_i - \langle A \rangle)^2 \quad (2.25)$$

$$= \langle A \rangle^2 \sum_i \sigma_i^{-2} + \sum_i \sigma_i^{-2} A_i^2 - 2\langle A \rangle \sum_i \sigma_i^{-2} A_i. \quad (2.26)$$

Since, as in the previous section, a good error estimate should result in $\chi^2 \approx N - 1$, the error in $\langle A \rangle$ is

$$\sigma_{\langle A \rangle} = \bar{\sigma}_{\langle A \rangle} \sqrt{\frac{\chi^2}{N - 1}}. \quad (2.27)$$

For ‘outlier’ data points with small values of either r or p , the expression $T/T_0 = \langle A \rangle$ is unstable, because A can essentially take any value between 0 and infinity. The data weighing in Eq. (2.23) does not entirely compensate for this fact. Further, the summation in Eq. (2.26) is written in a way that allows easy implementation in a computer program, because it does not require storage of all A_i values. However, Eq. (2.26) is somewhat sensitive to roundoff errors if the values of A_i that are averaged differ over many orders of magnitude, which can result in $\chi^2 < 0$. Fortunately, we can easily circumvent this problem by assigning thresholds for r and p and only counting laser shots with r , r_0 , p , and p all above these thresholds.

Compared to the method in the previous section, the present method of calculating T/T_0 can reduce the noise significantly if there are slow fluctuations in the pulse properties or in the sample transmittance. Under circumstances with highly fluctuating pulse energies, it may be a disadvantage that one small value for either r_i^0 , r_i , p_i^0 , or p_i can invalidate the whole expression in Eq. (2.21), which ends up as fewer data points contributing to the final value $\langle A \rangle$.

2.8 THERMAL EFFECTS IN THE SAMPLE

The energy of a pump pulse that is absorbed by the sample does not only lead to a transient absorbance change, but also to a temperature increase in the sample. There are two timescales on which this heating occurs. The faster timescale consists of the thermalization of the vibrational energy, that occurs within picoseconds after the pump pulse. Reference 74 discusses the mechanism of this thermalization. For sample thicknesses of $\sim 200 \mu\text{m}$, this thermalization leads to a very small temperature increase of $\sim 0.2 \text{ K}$, if we assume that $20 \mu\text{J}$ of pump pulse energy is homogeneously dissipated in a volume of $200^2 \times 500 \mu\text{m}^3$, or $\sim 2 \text{ K}$ for a volume of $100^2 \times 200 \mu\text{m}^3$. Because the absorption spectrum of the OH stretch vibration is somewhat dependent on the temperature, this temperature increase affects the delay dependence of the absorbance change by typically 10^{-3} , which is negligible with respect to the signals resulting from bleaching of the OH stretch vibration that are typically 10^{-1} .

The slower timescale results from the diffusion of heat out of the focus of the pump pulse. Because this process is slow compared to the repetition frequency of the laser, the net effect is a build-up temperature increase and gradient in the neighborhood of the focus. Of course, this issue is only relevant for a nonmoving sample, such as used for the experiments in Chapters 6 and 8. I will devote the rest of this section to estimate the magnitude of this effect.

The sample consists of two thick calcium fluoride windows with a thin liquid layer in between, where the energy of the pump pulses is dissipated. We will first consider the simple case of a homogeneous medium. If the medium has a heat conductivity λ , a heat

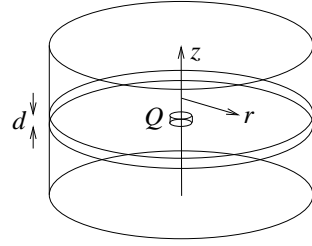


FIGURE 2.8. Geometry of the sample heating. The sample proper has a thickness d ; the heat source Q results from a laser beam that propagates in the z direction.

capacity C per unit volume, and a spherical heat source with power P and radius r_s at the origin, the steady-state temperature $T(r)$ as a function of distance $r > r_s$ from the origin satisfies

$$P = -4\pi\lambda r^2 \frac{dT}{dr}. \quad (2.28)$$

A boundary condition $T(\infty) = T_o$ leads to the solution

$$T(r) = \frac{P}{4\pi\lambda r} + T_o, \quad (2.29)$$

for $r > r_s$. The temperature at the center of the heat source can be obtained by substituting $r = r_s/2$ in Eq. (2.29), as can be shown by refining Eq. (2.28) for $r < r_s$. In water ($\lambda = 0.60 \text{ Wm}^{-1}\text{K}^{-1}$, Ref. 72), a heat source $P = 10 \text{ mW}$ with a radius $r_s = 100 \mu\text{m}$ will therefore lead to a steady-state temperature increase of 27 K. If the medium consists solely of window material (CaF_2 ; $\lambda = 10 \text{ Wm}^{-1}\text{K}^{-1}$, Ref. 58), the same heat source will cause a 1.6 K increase of the steady-state temperature.

The temperature increase in a realistic sample must lie somewhere between these two limiting values. For a quantitative calculation, we choose a cylindrical coordinate system as depicted in Fig. 2.8. The heat diffusion equation for the temperature $T(r, z, t)$ in this geometry is

$$\frac{\partial(CT)}{\partial t} = D \left(\frac{1}{r} \frac{\partial(CT)}{\partial r} + \frac{\partial^2(CT)}{\partial r^2} + \frac{\partial^2(CT)}{\partial z^2} \right) + \frac{\partial D}{\partial z} \frac{\partial(CT)}{\partial z} + Q, \quad (2.30)$$

where $D(z) \equiv \lambda(z)/C(z)$ is the position-dependent diffusion constant and $Q(r, z)$ is the heat source. We assume that

$$Q(r, z) = Q_o \exp\left(-\frac{r^2}{2r_o^2} - \alpha z\right) \quad (0 < z < d), \quad (2.31)$$

where r_o corresponds to an FWHM of $100 \mu\text{m}$ and $\alpha = -\ln(T_o)/d$ is the extinction coefficient that corresponds to a transmittance $T_o = 0.05$ with a sample thickness $d = 200 \mu\text{m}$. We choose Q_o such that the total dissipated power is 10 mW , which corresponds to $20 \mu\text{J}$ pump pulses at a repetition rate of 500 Hz (due to chopping). For a water sample, $C = 4.18 \times 10^6 \text{ Jm}^{-3}\text{K}^{-1}$ (Ref. 72); for the calcium fluoride windows, $C = 2.70 \times 10^6 \text{ Jm}^{-3}\text{K}^{-1}$ (Ref. 58). A simple forward time centered space (FTCS) algorithm¹⁰⁰ was used to integrate Eq. (2.30), with step sizes $\delta r = \delta z = 0.01 \text{ mm}$, $\delta t = 6.25 \mu\text{s}$. The boundary conditions were

$$T(r_{\max}, z, t) = T(r, -z_{\max}, t) = T(r, d + z_{\max}, t) = 0, \quad (2.32)$$

$$T(r, z, 0) = 0, \quad (2.33)$$

FIGURE 2.9. Calculated equilibrium temperature distribution (relative to the temperature at $r, z \rightarrow \infty$) in a CaF_2 sample cell for a 10-mW heat source. The shaded area indicates the sample (200 μm water). Subsequent contour lines correspond to temperatures that differ by a factor $10^{1/12}$. Temperatures are in K. The highest relative temperature is 11.0 K.

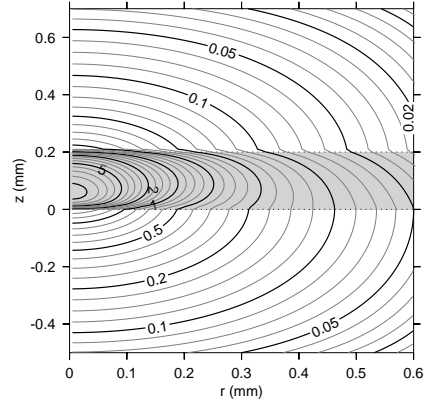


TABLE 2.1. Maximum temperature increases in the focus for a water sample with CaF_2 or sapphire windows at a dissipated power $Q = 10$ mW, for various sample thicknesses d and focus radii r_0 . In sapphire, $C = 3.0 \times 10^6$ Jm^{-3} and $\lambda = 34$ $\text{Wm}^{-1}\text{K}^{-1}$.⁵⁸

r_0 (mm)	d (mm)	$T_{\text{max, CaF}_2}$ (K)	$T_{\text{max, sapphire}}$ (K)
0.03	0.03	12.8	10.5
0.03	0.05	15.9	14.0
0.03	0.10	17.9	16.5
0.03	0.20	17.5	16.6
0.03	0.50	13.4	13.1
0.05	0.03	6.2	4.7
0.05	0.05	8.0	6.7
0.05	0.10	10.1	9.1
0.05	0.20	11.1	10.5
0.05	0.50	9.5	9.3
0.10	0.03	2.2	1.5
0.10	0.05	2.8	2.1
0.10	0.10	3.9	3.4
0.10	0.20	5.1	4.7
0.10	0.50	5.3	5.1

with $r_{\text{max}} = z_{\text{max}} = 0.8$ mm.⁵⁹ There exist algorithms to calculate the steady-state solution more efficiently¹⁰⁰ than by the FTCS algorithm, but the latter requires relatively limited programming effort. Figure 2.9 shows the temperature distribution at $t = 1$ s, which is very close to equilibrium, given that the equilibration time is 45 ms for this set of parameters. Table 2.1 shows the maximum temperature increases for some other parameter combinations.

⁵⁹The first term inside the brackets of Eq. (2.30) needs special attention, because it is undefined at $r \leq 0$. If $r_j = (j + 1/2)\delta r$, then for $j = 0$, the sum of the first two terms can be written as $2C(\delta t/\delta r^2)(T_i - T_0)$, which is well-defined.

3 GENERATION OF MID-INFRARED PULSES BY $\chi^{(3)}$ DIFFERENCE FREQUENCY GENERATION IN CaF_2 AND BaF_2

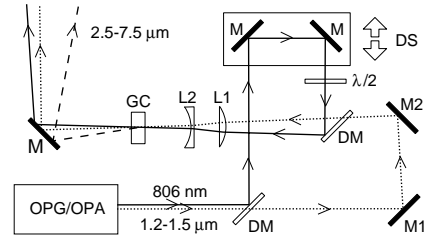
Tunable mid-IR pulses in the range $1300\text{--}4200\text{ cm}^{-1}$ ($7.7\text{--}2.4\text{ }\mu\text{m}$) are generated through a phase-matched four-wave mixing process in ordinary mid-IR window materials such as calcium fluoride and barium fluoride. In this process, the difference frequency $\omega_3 = 2\omega_2 - \omega_1$ is generated from pump fields ω_1 and ω_2 . The process can be phase-matched to different frequencies by adjustment of the angle between the pump fields.

3.1 INTRODUCTION

The common methods for generating femtosecond mid-infrared pulses employ various kinds of three-wave mixing processes, such as difference frequency generation and optical parametric generation and/or amplification (OPG/OPA), which is used for all pump-probe experiments in this thesis. As explained in §2.1, these processes all rely on the second-order polarization $P^{(2)}(t) \propto \chi^{(2)}E^2(t)$ created by a high-intensity field $E(t)$. This second-order polarization is nonzero only in materials that lack inversion symmetry. Then, fields with (angular) frequencies ω_1 and ω_2 couple to a field with frequency $\omega_3 = \omega_1 \pm \omega_2$. A high efficiency can only be obtained if the phase-matching condition $\mathbf{k}_3 = \mathbf{k}_1 \pm \mathbf{k}_2$ is fulfilled. The wavevectors \mathbf{k}_x have magnitudes $k_x = \omega_x/n_x$, where n_x is the index of refraction at frequency ω_x . Since in a medium with a normal dispersion, $n(\omega)$ is a monotonously increasing function of ω , the phase-matching condition is usually achieved by employing the birefringence of the $\chi^{(2)}$ material. The polarizations of the different fields are then chosen such that the ω_3 field experiences a lower index of refraction than the ω_2 field. In order to be suitable for $\chi^{(2)}$ infrared generation, a crystal should (1) be transparent for the wavelengths involved, (2) lack inversion symmetry, and (3) be sufficiently birefringent. There are many crystalline materials that satisfy these requirements for wavelengths shorter than $4.5\text{ }\mu\text{m}$, such as BBO, KTP, potassium titanyl arsenate (KTA), LiNbO₃, and KNbO₃. However, for many molecular vibrations other than the OH stretch, such as the CO stretch in organic molecules, longer wavelengths are necessary. Unfortunately, the available crystals for wavelengths beyond $4.5\text{ }\mu\text{m}$, such as AgGaS₂,⁴⁸ GaSe,⁵⁶ and ZnGeP₂⁹⁸ cannot be directly pumped with the currently available high-intensity 800 nm Ti:sapphire lasers.

As an alternative to the $\chi^{(2)}$ -based pulse generation discussed above, we will now consider $\chi^{(3)}$ (or four-wave-mixing) processes. Here, three fields interact and drive a third-order polarization $P^{(3)}(t) \propto \chi^{(3)}E^3(t)$. Compared to $\chi^{(2)}$ processes, the advantage of $\chi^{(3)}$ processes is that $\chi^{(3)}$ is nonzero in any medium, without any restrictions on the crystal symmetry. Therefore, $\chi^{(3)}$ frequency mixing is, in principle, possible in any medium, in-

FIGURE 3.1. Setup for $\chi^{(3)}$ pulse generation. Abbreviations: OPG/OPA: optical parametric generation/amplification infrared source; DM: dichroic mirror; M, M1, M2: mirrors; $\lambda/2$: half-wave plate; DS: delay stage; L1, L2: 2:1 telescope (BK7 glass); GC: generation crystal (4 mm CaF_2 or BaF_2). We used M1 and M2 to adjust the angle between the pump and the signal beams.



cluding isotropic media. Since the latter have no birefringence, one must use alternative means to fulfill the requirement of phase-matching.

Pulses in various wavelength ranges have been generated by means of $\chi^{(3)}$ techniques. For example, far-infrared (around 60 cm^{-1}) pulses have been generated in air.¹⁸ Due to the low value of $\chi^{(3)}$ in air, the pulse energy was only about 5 pJ, which required time-gated and phase-sensitive THz detection schemes. In the ultra-violet, the properties of certain modes in hollow fibres have been employed to generate light in gases at well-chosen pressures with $\sim 4 \mu\text{J}$ pulse energies.²⁴ Further, in the mid-infrared, 1064 nm and tunable dye-laser pulses have been combined to generate tunable picosecond pulses at $\sim 1 \text{ pJ}$ pulse energies in a phase-matched $\chi^{(3)}$ process.⁹³

In this chapter, we show how the approach of Ref. 93 can be used to generate mid-IR ($2.4\text{--}7.6 \mu\text{m}$) pulses with high energies and femtosecond durations with the currently available titanium-sapphire laser systems. Here, pump fields with frequencies ω_1 and ω_2 generate a difference frequency $\omega_3 = 2\omega_2 - \omega_1$, with $\mathbf{k}_3 = 2\mathbf{k}_2 - \mathbf{k}_1$ as the phase-matching condition. We use the common window materials CaF_2 and BaF_2 as generating media. In these non-birefringent materials, phase-matching is possible, despite the fact that they have a normal dispersion. The reason is that the fields $2\omega_2$ and ω_1 are equivalent to the fields with the high and medium frequencies, respectively, while $\omega_2 < \omega_1$ counts for the corresponding indices of refraction.

3.2 EXPERIMENT

We used a commercial Ti:sapphire laser (Quantronix Titan; 100 fs, 2.5 mJ pulses, 1 kHz repetition rate) to pump a parametric conversion device based on BBO (§2.2.2). From the output of the device, we used the signal ($6250\text{--}8300 \text{ cm}^{-1}$, $300 \mu\text{J}$) and the remaining pump (12400 cm^{-1} , 1.1 mJ) for the ω_2 and ω_1 fields, respectively, as shown in Fig. 3.1. After having been split and recombined for time-overlap, the pulses were collimated to a diameter of approximately 2 mm before interacting in a 4-mm-thick CaF_2 or BaF_2 plate. Because of the properties of the $\chi^{(3)}$ tensor, the intensity of the generated ω_3 field is 9 times higher for parallel ω_1 and ω_2 pump fields than for perpendicular pump fields.¹⁰⁹ Therefore, we used a wave plate to make the polarizations of the pump and signal pulses parallel.

A delay stage enabled adjustment of the time overlap between the pump and signal pulses. At time overlap, we generated pulses with typical energies of 100–200 nJ.

If the laser pulses are focused in air in a collinear geometry, similar to Ref. 18, a measurable amount of infrared is generated as well, but with a typical energy of only 3 nJ and

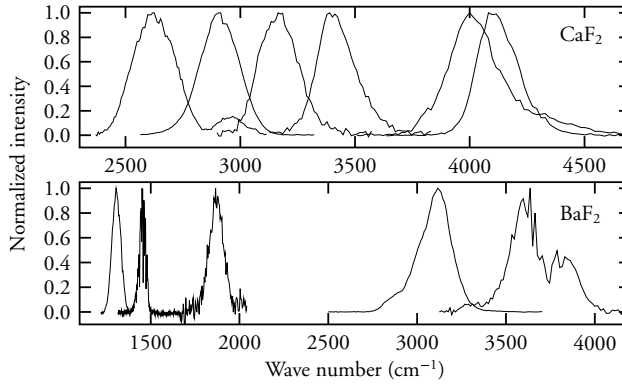


FIGURE 3.2. Typical spectra of the generated pulses in CaF_2 (top) and BaF_2 (bottom). The structure in the spectra at 1500 and 3700 cm^{-1} is caused by absorption lines of water vapor (see also Fig. 1.2).

a bandwidth of 400 cm^{-1} FWHM. Also, a visible amount of light at frequency $2\omega_1 - \omega_2$ is generated in that case.

3.3 RESULTS

Figure 3.2 shows typical spectra of the pulses generated in CaF_2 and BaF_2 . We obtained these spectra with a scanning monochromator and PbSe (for the CaF_2 data) and HgCdTe (for BaF_2) detectors. We chose these detectors for their different spectral responses. In order to tune ω_3 , we adjusted both ω_2 (defines the difference frequency ω_3) and the angle between \mathbf{k}_1 and \mathbf{k}_2 (phase-matching). The FWHM bandwidth of the generated spectra is about 200 cm^{-1} for CaF_2 and 40–300 cm^{-1} for BaF_2 , respectively. The maximum frequency ω_3 is approximately 4100 cm^{-1} , limited by ω_2 , which could not be tuned higher than about 8250 cm^{-1} in our OPG/OPA.

Figure 3.3 shows an autocorrelate for pulses generated in CaF_2 at 2580 cm^{-1} . We measured this by generating the second harmonic of the infrared pulses in a LiIO_4 ($\theta = 20$ deg) crystal. The FWHM autocorrelate width is 298 fs, which corresponds to a 211 fs pulse duration if we assume a Gaussian pulse shape. With a bandwidth of 200 cm^{-1} FWHM, this pulse duration implies $\Delta\nu\Delta\tau = 1.3$ for the frequency–bandwidth product.

Figure 3.4 shows the tuning curve with the generated frequency ω_3 versus the angle $\beta = \angle(\mathbf{k}_1, \mathbf{k}_3)$. Calculated tuning curves are shown as well; we obtain these by substituting $k_x = n_x\omega_x$ in the phase-matching condition $\mathbf{k}_3 = 2\mathbf{k}_2 - \mathbf{k}_1$, which yields

$$\cos(\beta) = \frac{4n_2^2\omega_2^2 - n_1^2\omega_1^2 - n_3^2\omega_3^2}{2n_1n_3\omega_1\omega_3}, \quad (3.1)$$

where n_i are the indexes of refraction as calculated from the Sellmeier equations for CaF_2 ^{58,80} and BaF_2 .^{58,81} Due to the dispersive properties of these materials, Eq. (3.1) imposes a lower limit on the frequency ω_3 that can be generated in this process. This cut-off occurs at $\beta = 0$ deg.

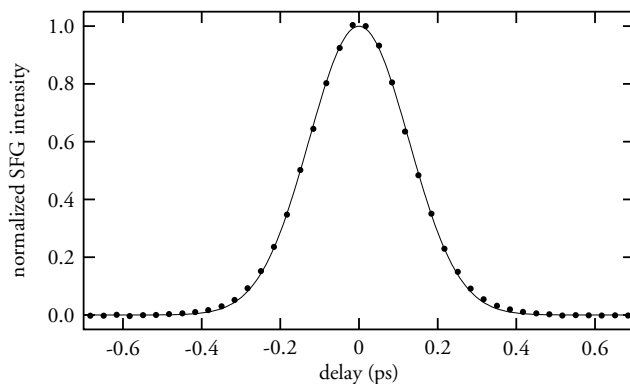


FIGURE 3.3. Autocorrelate of pulses generated in CaF_2 at 2580 cm^{-1} with a fit to a Gaussian pulse shape.

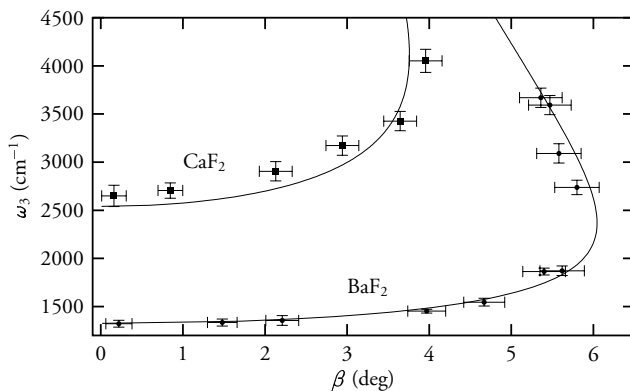


FIGURE 3.4. Tuning curves for BaF_2 and CaF_2 . Data points: experiment with the FWHM bandwidth as the vertical errorbar. Drawn lines: calculated tuning curve for $\omega_1 = 12400 \text{ cm}^{-1}$.

For BaF_2 , we obtained a better agreement between experiment and calculated tuning curve if we increased the index of refraction at frequency ω_1 by 1.0×10^{-4} . Instead of 1286 cm^{-1} ($7.8 \mu\text{m}$) and 6.5 deg for the cut-off frequency and maximum angle, respectively, this yields 1325 cm^{-1} and 6.0 deg , respectively (as shown in Fig. 3.4). In CaF_2 , the difference between experiment and theory can result from a frequency-dependent deviation less than 10^{-4} in the refractive index for the ω_2 field. We note that experimental values of the index of refraction are known to differ by similar amounts from the calculated values.^{58,80,81}

3.4 CONCLUSIONS

We have shown that a $\chi^{(3)}$ difference frequency generation process with two pump fields can be phase-matched in the common infrared window materials CaF_2 and BaF_2 , which have no special birefringent or crystal symmetry properties. An 806 nm laser pulse as the high-frequency (ω_1) pump enables the generation of difference frequencies over the range 2.4–7.6 μm with the angle between the pumping fields as a tuning parameter. We obtained pulse energies up to 200 nJ.

As a final note we would like to point out that the presented type of $\chi^{(3)}$ difference frequency generation can be phase matched in *any* material with a normal dispersion relation, although the angles and cut-off wavelengths vary. A common material especially worth mentioning in this respect is NaCl, with $\omega_3 > 600 \text{ cm}^{-1}$ and $\beta < 17 \text{ deg}$.

4 VIBRATIONAL RELAXATION IN HDO:D₂O

We present a study on the relaxation of the OH stretch vibration in a dilute HDO:D₂O solution using femtosecond mid-infrared pump-probe spectroscopy. We performed one-color experiments in which the $0 \rightarrow 1$ vibrational transition is probed at different frequencies and two-color experiments in which the $1 \rightarrow 2$ transition is probed. In the one-color experiments, it is observed that the relaxation is faster at the blue side than at the center of the absorption band. Furthermore it is observed that the vibrational relaxation time T_1 shows an anomalous temperature dependence and increases from 0.74(1) ps at 298 K to 0.90(2) ps at 363 K. These results indicate that the OH \cdots O hydrogen bond forms the dominant accepting mode in the vibrational relaxation of the OH stretch vibration.

4.1 INTRODUCTION

In any pump-probe experiment (§1.2) on the OH stretch vibration of an aqueous system, the most prominent feature is vibrational relaxation: vibrationally excited OH bonds stay excited during a few picoseconds at most. Because vibrational relaxation means that energy is transferred to other degrees of freedom, a measurement of the vibrational lifetime T_1 provides information on inelastic interactions. The temperature dependence of T_1 can help to identify the modes to which the energy of the excited OH stretch vibration is transferred.⁹⁰ Typically, the lifetime decreases with increasing temperature.

A wide range of vibrational lifetimes has been reported for the OH stretch vibration of HDO dissolved in D₂O. The first experiments on its vibrational relaxation reported $T_1 = 8(2)$ ps (based on time-resolved experiments with 11 ps pulses⁴⁵) and $T_1 = 0.45(15)$ ps (based on saturation with high-intensity light¹²⁴). More recently, experiments with shorter pulses (0.2–0.5 ps) yielded values ranging from 0.7 to 1.0 ps.^{33,67,132}

This chapter presents a detailed investigation of the relaxation mechanism of the OH stretch vibration of HDO dissolved in D₂O. We measured the relaxation rate as a function of temperature for both the $0 \rightarrow 1$ and the $1 \rightarrow 2$ vibrational transitions. The combination of these experiments enables us to identify the vibrational relaxation mechanism.

4.2 EXPERIMENT

The experiments were pump-probe measurements where a femtosecond infrared laser pulse excited the $\nu = 0 \rightarrow 1$ transition of the OH stretch vibration of HDO molecules dissolved in D₂O. The transmittance of a subsequent probe pulse is a measure of the degree of excitation of the OH groups in the solution. The probe pulse was either at the same frequency (one-color experiments) or at a different frequency (two-color experiments). The general background on pump-probe experiments is discussed in §1.2; the details of the pulse generation in §2.2.3 and §2.2.4; and the pump-probe setup in §2.4.2. The sample was a 500 μm -thick layer of a HDO:D₂O solution in a sample cell that was continuously

rotated to eliminate local accumulation of heat (§2.8) and that was equipped with a heater that enabled us to control the temperature within 1 K. For the data in Fig. 4.2 we employed a cryostatic cell that was not rotated. To prevent local heating in this cell, we lowered the repetition rate of the laser from 1 kHz to 70 Hz. By use of polarizers (in the one-color experiments) or a magic-angle polarization (in the two-color experiments), we ensured that the measured signals are not sensitive to the reorientational motions of the individual HDO molecules.

4.3 RESULTS

In order to investigate the lifetime of the OH stretch vibration, we first carried out two-color experiments in which the $0 \rightarrow 1$ transition is pumped and the $1 \rightarrow 2$ transition is probed. Figure 4.1 shows typical measurements at different temperatures. In this experiment, the time constant of the decay is equal to the vibrational relaxation time, since the absorbance change is directly proportional to the excited population in the $\nu = 1$ state. The relaxation time T_1 is thus obtained by fitting the data to a single-exponential decay.

For small delay times the measured signals can be influenced by effects other than the vibrational relaxation. (i) The signals are strongly affected by spectral diffusion: due to the inhomogeneous broadening of the absorption band, the pump pulse excites only a part of the absorption band, which leads to the formation of a spectral hole. In liquid water the spectral diffusion takes place on a sub-picosecond timescale^{33,134} and is virtually complete after 1 ps. In Chapter 8, we will discuss this spectral diffusion in more detail. (ii) Not unlikely, the vibrational relaxation rate varies over the absorption band, which can affect the measured signals at small delay times. However, when the spectral relaxation is complete, one will observe only one effective average decay time, independent of the probing frequency. (iii) We cannot completely exclude the artifacts mentioned in §2.6 under point 6 and 7 (the former for the one-color experiments discussed later).

Because of these effects at short delay times, we fitted our data on liquid water only for delay values larger than 1.0 ps. Since the relaxation in ice turns out to be much faster, we fitted the data obtained for ice for delays larger than 0.4 ps.

Figure 4.2 shows the vibrational relaxation times measured in the two-color experiments for both frozen and liquid HDO:D₂O.¹³⁴ It shows that in the solid phase (ice-*Ih*), the relaxation time is virtually independent of temperature with an average value of 0.37(2) ps, and in liquid water the relaxation time increases with temperature from 0.74(1) ps at 270 K to 0.90(2) ps at 363 K.

Figure 4.3 shows typical measurements for a one- and a two-color experiment, at a temperature of 363 K. The decay times are 1.05(2) and 0.90(2) ps, respectively. Clearly, the one-color data show a slower decay than the two-color data.

Figure 4.4 shows an overview of the decay times for different frequencies and temperatures above the melting point of D₂O (277 K). It shows that for all temperatures, the decay of the absorbance change $\Delta\alpha$ is slower in the one-color measurements as compared to the data of the two-color experiments. Moreover, in the one-color experiments, the decay time constant increases as the frequency is shifted from the blue side (3500 cm⁻¹) to the center (3400 cm⁻¹) of the absorption band.

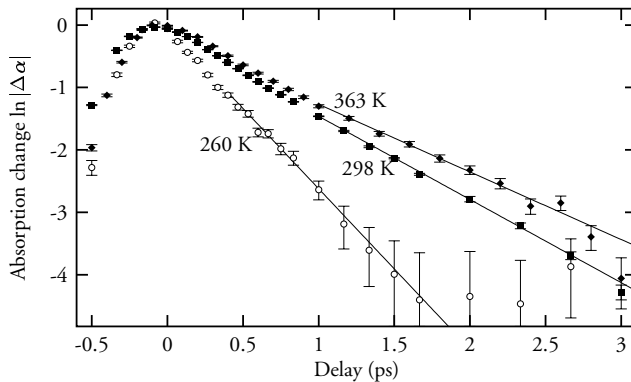


FIGURE 4.1. Typical normalized magic angle two-color measurements on solid (260 K) and liquid (298 and 363 K) HDO in D₂O at different temperatures. In liquid water, the pump and probe frequencies were 3400 and 3150 cm⁻¹, respectively. In ice, the frequencies were 3330 and 3090 cm⁻¹, respectively.

4.4 INTERMEDIATE-STATE MODEL

The results from the one-color experiments at 3400 cm⁻¹ and 3500 cm⁻¹, shown in Fig. 4.4, suggest a frequency dependence of the vibrational relaxation time. However, due to the fast spectral relaxation, discussed in Section 4.3,^{33,134} this cannot cause a different decay rate of the observed signal for delays larger than 1 ps.

We can explain the one-color data having a slower decay than the two-color data if the excited HDO molecule does not relax directly to the ground state, but rather to an intermediate state. This can be shown as follows. The absorbance change for a transition $a \rightarrow b$ is

$$\Delta\alpha_{a \rightarrow b} = \rho\sigma_{ab}(\Delta n_a - \Delta n_b), \quad (4.1)$$

where ρ is the number of molecules per unit area, σ_{ab} is the cross-section for a radiative transition and Δn_a and Δn_b are the changes in populations of the two levels with respect to the equilibrium populations. In a two-color experiment, the decay of the absorbance change $\Delta\alpha_{1 \rightarrow 2}$ induced by the pump only depends on the decay of Δn_1 , since the $\nu = 2$ state is not populated. However, in a one-color experiment, the absorbance change $\Delta\alpha_{0 \rightarrow 1}$ depends on both Δn_1 and Δn_0 . If, due to an intermediate state, the decays of Δn_0 and Δn_1 are not equal, this will influence the relaxation of the observed absorbance change.

In the following quantitative description, we label the intermediate state as $|o^*\rangle$. This intermediate state $|o^*\rangle$ is a combination of the ground state of the OH stretch mode and other modes that were excited by the energy release from the $\nu = 1$ state decay. Consequently, the $|o^*\rangle$ state can be excited to a $|1^*\rangle$ state, where both the OH stretch mode and the unknown other modes are excited. Due to anharmonic coupling, the center frequency of this $o^* \rightarrow 1^*$ transition can differ from the ordinary $o \rightarrow 1$ transition. Hence, the cross sections at a given laser frequency can differ. With cross sections σ^* for the $o^* \rightarrow 1^*$ and σ for the $o \rightarrow 1$ transitions, we can extend Eq. (4.1) to

$$-\Delta\alpha_{01}(t) = \rho\sigma[\Delta n_o(t) - \Delta n_1(t) + (\sigma^*/\sigma)\Delta n_{o^*}(t)] \quad (4.2)$$

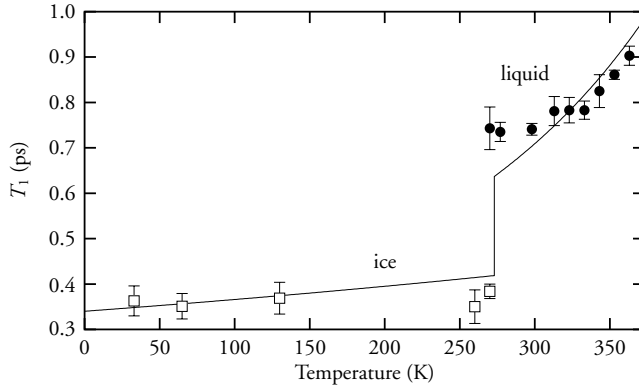


FIGURE 4.2. Vibrational relaxation time of the OH-stretch vibration of HDO in D₂O, measured in two-color measurements. The open and closed symbols denote results in ice and liquid water, respectively. The drawn line corresponds to Eq. (4.7).

Clearly, the measured decay depends on the value of the cross-section ratio σ^*/σ at the probing frequency.

If the rate for the $1 \rightarrow o^*$ relaxation process is given by k_A , and for the $o^* \rightarrow o$ relaxation by k_B (See Fig. 4.5), the dynamics of the population changes of the states satisfy the differential equation

$$\frac{d}{dt} \begin{pmatrix} \Delta n_1(t) \\ \Delta n_{o^*}(t) \\ \Delta n_o(t) \end{pmatrix} = \begin{pmatrix} -k_A & 0 & 0 \\ k_A & -k_B & 0 \\ 0 & k_B & 0 \end{pmatrix} \begin{pmatrix} \Delta n_1(t) \\ \Delta n_{o^*}(t) \\ \Delta n_o(t) \end{pmatrix}. \quad (4.3)$$

Its solution, expressed in the population changes at $t = 0$, is

$$\begin{pmatrix} \Delta n_1(t) \\ \Delta n_{o^*}(t) \\ \Delta n_o(t) \end{pmatrix} = M(t) \begin{pmatrix} \Delta n_1(0) \\ \Delta n_{o^*}(0) \\ \Delta n_o(0) \end{pmatrix}, \quad (4.4)$$

where

$$M(t) = \begin{pmatrix} e^{-k_A t} & 0 & 0 \\ \frac{k_A}{k_B - k_A} (e^{-k_A t} - e^{-k_B t}) & e^{-k_B t} & 0 \\ \frac{1}{k_A - k_B} (k_B e^{-k_A t} - k_A e^{-k_B t}) + 1 & 1 - e^{-k_B t} & 1 \end{pmatrix}. \quad (4.5)$$

We can combine Eqs. (4.2) and (4.4) with the initial values

$$(\Delta n_1(0), \Delta n_{o^*}(0), \Delta n_o(0)) = a(1, 0, -1) \quad (4.6)$$

defined by the pump pulse excitation, where a is an arbitrary amplitude. The parameters k_A , k_B , and σ^*/σ must be derived from the actual data. The value k_A follows directly from the two-color experiments in which the $1 \rightarrow 2$ transition is probed ($k_A = 1/T_1$ as in Fig. 4.2). Knowing k_A , we can use the one-color data to find the values for k_B and σ^*/σ . As

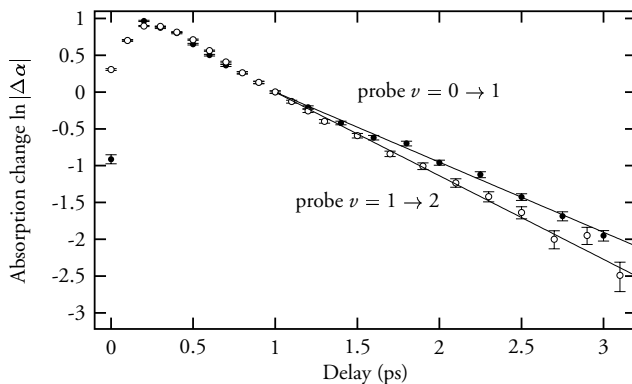


FIGURE 4.3. Typical delay scans for the isotropic absorbance change in dilute HDO:D₂O, after excitation at 3400 cm⁻¹. The temperature was 363 K and the data are normalized at $t = 1.0$ ps. The drawn lines are fits to exponentials. Note the difference in decay rates.

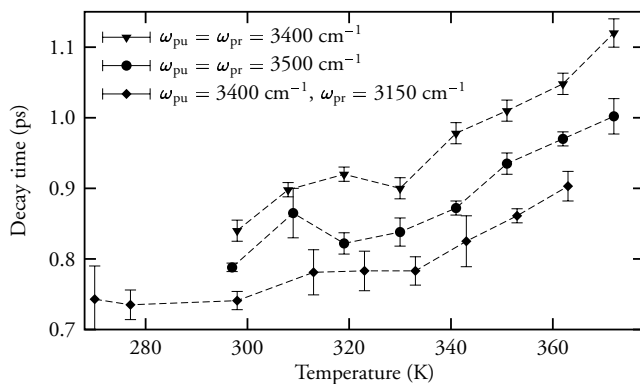
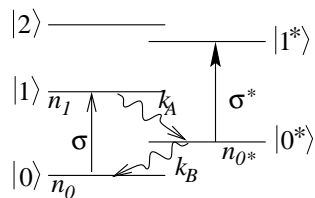


FIGURE 4.4. Vibrational decay time constant for different temperatures as found in one- and two-color experiments.

FIGURE 4.5. States and quantities used in the analysis. The states on the left are pure excitations of the OH vibration, while the states on the right are combinations of OH vibrational excitations and excitations of other modes.



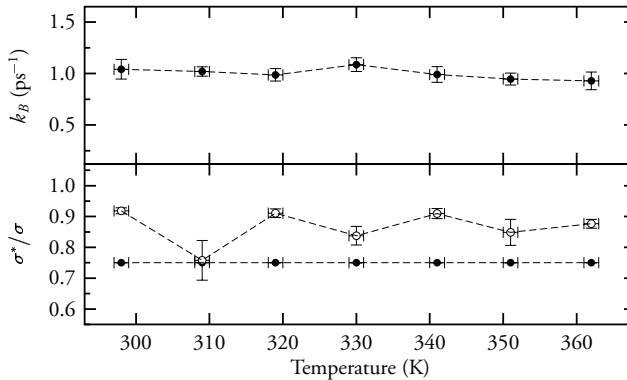


FIGURE 4.6. The decay rate k_B and the cross-section ratio σ^*/σ as a function of temperature. In the upper half, the decay rate k_B is shown that results from fitting the data at 3400 cm^{-1} , with the cross-section ratio σ^*/σ fixed at 0.75 . These k_B values are used to find the cross sections at 3500 cm^{-1} in the bottom half (open symbols). For comparison, the fixed cross-section at 3400 cm^{-1} is shown as well (closed symbols).

the difference between the one-color and two-color data is most prominent at the center of the absorption band (3400 cm^{-1}), a first attempt is to fit values for k_B and σ^*/σ at that frequency. Since the two-color data were obtained at slightly different temperatures, we interpolated the k_A values linearly from the nearest temperatures above and below. However, because the quantities k_B and σ^*/σ are mathematically strongly correlated, it is difficult to determine them independently from each other within the accuracy of the experimental data.

It is reasonable to assume that the cross-section ratio σ^*/σ does not depend strongly on temperature. The vibrational relaxation of the OH vibration leads to a transfer of approximately 3400 cm^{-1} to a few accepting modes. If there would be only one accepting mode, the resulting degree of excitation of this mode would correspond to a thermal distribution at a temperature of approximately 5000 K . We can therefore expect that the comparatively small range of temperatures in our measurements does not have much influence on the cross-section ratio σ^*/σ of the intermediate state and we assume that σ^*/σ has a constant value. The values for σ^*/σ obtained from the first fit varied between 0.55 and 0.95 ps; we therefore assume that $\sigma^*/\sigma = 0.75(20)$ and use this value as a fixed parameter to fit all data with pump and probe frequency at 3400 cm^{-1} . This procedure yields values for k_B as a function of temperature, as shown in the upper half of Fig. 4.4. With this approach, there is clearly no significant temperature dependence. Using these k_B values, we can now fit the cross-sections at the 3500 cm^{-1} probe frequency, as shown in Fig. 4.4. At 3500 cm^{-1} , the cross section σ^* is systematically larger compared to 3400 cm^{-1} , with no significant temperature dependence. The latter confirms that both k_B and σ^*/σ are not significantly dependent. However, the uncertainty in σ^*/σ of approximately ± 0.2 causes an error in the value of k_B . By repeating the procedure for the 3400 cm^{-1} data with $\sigma^*/\sigma = 0.55$ and 0.95 , we find that $k_B = 1.0(5)\text{ ps}^{-1}$. In all three cases, we find that the cross-section σ^* at 3500 cm^{-1} is systematically larger than the cross-section at 3400 cm^{-1} .

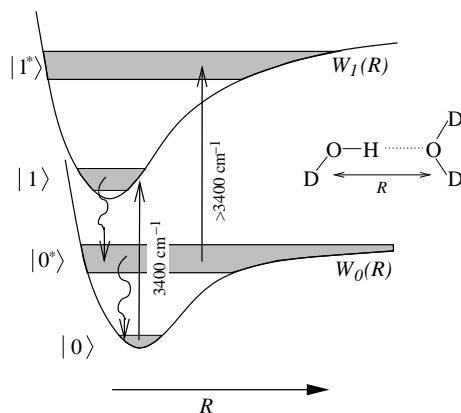


FIGURE 4.7. Schematic potentials $W_v(R)$ of the hydrogen bond mode, for the $\nu = 0$ and $\nu = 1$ OH stretch states. Shown are the proposed $|0\rangle$, $|1\rangle$, $|0^*\rangle$, and $|1^*\rangle$ states, the central excitation frequencies and the non-radiative decay paths.

4.5 DISCUSSION

The systematically larger cross-sections at 3500 cm^{-1} compared to 3400 cm^{-1} suggest that the $0^* \rightarrow 1^*$ transition has a blue-shifted frequency with respect to the normal OH stretch excitation. This is quite surprising, since excitation of other anharmonically coupled molecular modes leads normally to a redshift of the vibrational frequency^{43,42}. However, the blueshift can be well explained if the $|0^*\rangle$ state is an OH-stretch $\nu = 0$ state in combination with a highly excited hydrogen-bond stretch state. The $|1^*\rangle$ state then corresponds to the case where both the hydrogen bond and the OH bond are excited. A qualitative picture of the energy levels involved is shown in Fig. 4.7. Figure 8.3 on page 91 shows a more quantitative calculation of these potentials.

In principle, the hydrogen-bond dynamics within each of the hydrogen-bond potentials $W_v(R)$ could be calculated by solving the one-dimensional Schrödinger equation in R with $W_v(R)$ as the potential. This type of description would be appropriate for gas-phase hydrogen-bonded clusters in which the hydrogen-bond vibration is nearly undamped. For these systems, the coupling between the OH stretch vibration and the hydrogen-bond mode leads to a hydrogen-bond vibrational (Franck-Condon) progression of the absorption spectrum of the OH stretch vibration.¹⁰¹ However, in the liquid phase, the transient (Chapter 8) and linear absorption spectra of HDO:D₂O (Fig. 1.3 on page 13) do not contain sidebands and are very broad. This indicates that the hydrogen-bond vibrations of liquid water are strongly overdamped, which implies that the wavefunctions in R are strongly coupled to each other and to other low-frequency liquid modes. The dynamics in R are therefore not determined by the level spacing of the unperturbed vibrational levels of the hydrogen-bond mode, but result rather from a stochastic modulation of the value of R due to the interactions with the surrounding liquid. This type of dynamics can best be described as a diffusion process in the potential $W_v(R)$, as we will see in Chapter 5.

We must note here that it is a conceptual simplification to regard $|0^*\rangle$ as a single and well-defined state. A more accurate description would involve a broad band of hydrogen bond energy levels, each of which causes a different blueshift and cross-section of the OH stretch transition. In principle, application of such a model would give more detailed information on the lifetime of each individual excited quantum state of the hydrogen bond. However, the fact that the data can be described satisfactorily with a single intermediate

state $|0^*\rangle$) and a single relaxation rate constant $k_B = 1.0(5) \text{ ps}^{-1}$ shows that our experimental limitations do not allow us to obtain information about these more subtle details. Therefore we limit ourselves to a lifetime for the average excitation level of the hydrogen bond.

Apart from the relaxation through the hydrogen bond, there may be other relaxation channels, in which either all OH stretch energy is transferred to a low-frequency mode other than the hydrogen-bond stretch, or in which the OH stretch energy is distributed over several modes, amongst which the hydrogen-bond mode. In the latter case, the hydrogen-bond mode does not receive the entire 3400 cm^{-1} of the OH stretch energy, but only some fraction. However, other accepting modes such as the intramolecular bend mode are likely to cause a small transient redshift,^{42,43} as opposed to the present blueshift, while modes in neighboring D₂O molecules would not cause any significant frequency shift at all. Therefore, the hydrogen-bond stretch mode must account for a significant fraction of the OH-stretch decay. Other candidates for accepting modes include the OD stretch of HDO (further denoted as ν_{1a}) at 2500 cm^{-1} , the OD stretch of D₂O (ν_{1b} , 2500 cm^{-1}), the HOD bend (δ_1 , 1450 cm^{-1}), and the DOD bend (δ_2 , 1210 cm^{-1}). Recently, Deák et al.²¹ showed in a time-resolved anti-Stokes Raman study that relaxation following the excitation of the OH stretch in HDO:D₂O results in a population of ν_1 (1a and 1b are spectrally indistinguishable), of δ_1 , and of δ_2 . Upon decay of the OH stretch vibration, approximately 3400 cm^{-1} of energy must be transferred to its environment, the first step of which is normally the excitation of several other modes, that can be the hydrogen-bond stretch (which we have proposed in this chapter) or the mentioned ν and δ modes. In principle, several different relaxation pathways may occur with different probabilities. Deák et al.²¹ estimated that de-excitation of one OH stretch mode results in ≥ 0.6 quanta of δ_1 , ≥ 0.6 of δ_2 , and 0.1 of ν_1 . These estimates indicate that, on the average, still up to 1550 cm^{-1} of the energy of the OH stretch mode is donated to the hydrogen-bond stretch mode.

With the hydrogen bond as the dominant accepting mode, the anomalous temperature dependence of the vibrational relaxation time T_1 can also be explained. A theoretical model of the energy transfer from the OH stretch vibration to the OH \cdots O hydrogen bond was developed by Staib and Hynes.¹¹⁴ Their model system consists of a single OH bond coupled to a single hydrogen bond. The coupling is described by Lippincott-Schroeder potentials, that incorporate the gas-phase OH-bond potential, the hydrogen bond, and the Van der Waals and electrostatic interactions. (these potentials will be discussed in detail in Chapter 8.) The hydrogen bond causes the OH stretch frequency to shift from the gas-phase frequency ω_{gas} to a condensed-phase frequency ω . The model shows that the vibrational lifetime $T_1(\text{OH})$ depends on this redshift as

$$T_1(\text{OH}) \propto (1 - \omega/\omega_{\text{gas}})^{-1.8}. \quad (4.7)$$

This relation has been verified experimentally for a wide range of hydrogen-bonded complexes⁸⁶ and can be understood qualitatively in the following way. The redshift of the absorption band of the OH stretch vibration induced by the hydrogen bond is a measure for the strength of the interaction between the hydrogen bond and the OH stretch vibration. If the interaction gets stronger, the rate of energy transfer to the hydrogen bond will be faster, leading to a shorter T_1 . When the temperature is increased, the absorption spectrum of the OH stretch vibration shifts towards higher frequencies, which implies that

the average hydrogen-bond strength in water decreases. This explains the increase of T_1 with temperature. By combining Eq. (4.7) with the known temperature dependence of the OH absorption band redshift²⁸, we can describe the T_1 data quite well (see Fig. 4.2).

The relaxation mechanism observed for HDO is to some extent analogous to the relaxation of the OH stretch vibration of ethanol clusters dissolved in carbon tetrachloride (CCl₄).^{46,66,133} In this system, the hydrogen bond is the main accepting mode in the relaxation of the OH stretch vibration. The energy that is transferred from the OH stretch vibration to the hydrogen bond causes the hydrogen bond to dissociate with a transient blue-shifted absorption of dissociated ethanol cluster fragments as a result. The hydrogen bond reassociation in the ethanol clusters is relatively slow and has a time constant of approximately 20 ps. For water, as we have seen, the relaxation of the hydrogen bond is much faster and has a time constant $1/k_B \approx 1$ ps. A likely reason for the fast hydrogen-bond relaxation in water is that, due to the network of hydrogen bonds, the energy can be dispersed very fast over the environment of the initially excited molecule. In contrast, in the experiment on ethanol dissolved in CCl₄, the CCl₄ environment does not provide efficient accepting modes and thus the hydrogen bond relaxes much slower.

4.6 CONCLUSIONS

Using femtosecond mid-infrared pump-probe experiments, we have measured the lifetime of the OH stretch vibration in liquid HDO in D₂O. For ice-*Ih*, the lifetime has a constant value of 0.37(2) ps over the range 33–270 K, while for liquid water, the lifetime increases from 0.74(2) ps at 270 K to 0.90(2) ps at 363 K. This temperature dependence is quite anomalous since in general it is observed that the vibrational lifetime decreases with temperature. If the 0 → 1 transition is probed, it is observed that the relaxation of the bleaching is faster at the blue side of the absorption band than at the center of the absorption band. Both this observation and the anomalous temperature dependence of the vibrational lifetime can be well explained if the OH...O hydrogen bond forms the main accepting mode in the vibrational relaxation of the OH stretch vibration. From a detailed analysis of the data we find that the excited hydrogen bond relaxes with a time constant of 1.0(5) ps. This relaxation is relatively fast compared to other hydrogen-bonded systems, which can be explained from the fact that the network of hydrogen bonds in liquid water allows a very rapid dissipation of energy.

5 ISOTOPE EFFECTS ON VIBRATIONAL RELAXATION AND HYDROGEN-BOND DYNAMICS IN WATER

Pump–probe experiments HDO dissolved in liquid H₂O show the spectral dynamics and the vibrational relaxation of the OD stretch vibration. We find a correlation time $\tau_c = 0.40$ ps for the spectral diffusion and a lifetime $T_1 = 1.8$ ps for the vibrational relaxation. These values differ significantly from those of the OH stretch vibration of HDO:D₂O.

5.1 INTRODUCTION

Most time-resolved experiments on water in this thesis and in the literature^{33,129,135,132} are devoted to isotopically diluted aqueous systems, i.e. HDO in D₂O instead of H₂O. This is to avoid strong heating effects and to be able to study the behavior of an ‘isolated’ OH group (§1.1, §1.2, §2.8). The OD stretch vibration in D₂O has a frequency of ≈ 2500 cm⁻¹, compared to ≈ 3400 cm⁻¹ for the OH stretch vibration in H₂O. Thus, resonant energy-transfer from an excited OH group to an OD group is not possible.

However, though chemically very similar, H₂O and D₂O are not identical. Because the mass of the D atom is twice as large as the H atom, many processes that involve hydrogen bonds or the transfer of a proton have different kinetics if the proton is replaced by a deuteron. One consequence of this difference is that animals, including humans, cannot live if more than 20% of the water in their body is replaced by heavy water.⁶⁴ In the previous chapter, we saw that the vibrational lifetime of the OH stretch vibration of HDO in D₂O is $T_1 = 740$ fs. Further, the frequency of an individual OH group is known to vary in time with a time constant of ≈ 600 fs.^{33,129} (Chapter 8 will discuss this in more detail). This so-called spectral diffusion is the direct result of hydrogen-bond length fluctuations, i.e. the O–O distance R in the DO–H···OD₂. Though the OH group contains a proton, for R to vary, the hydrogen-bond accepting D₂O molecule must move, which necessarily changes the surrounding ‘deuteron-bond’ structure. Therefore, the timescale of spectral diffusion in HDO:D₂O is likely to be more representative of the deuteron-bond dynamics of the solvent, D₂O, than of the hydrogen-bond dynamics in ordinary water.

Time-resolved experiments on the OH stretch vibration in pure H₂O have been done, but it is difficult to extract information on the hydrogen-bond dynamics due to rapid resonant energy transfer between the OH groups^{21,131} and the overwhelmingly strong thermal effects.⁷⁴ However, in the same way that the experiments on the OH stretch vibration of HDO in D₂O provide information on the deuteron-bond dynamics of the solvent, an experiment on the OD stretch vibration of HDO in H₂O will yield information on the hydrogen-bond dynamics of ordinary water.

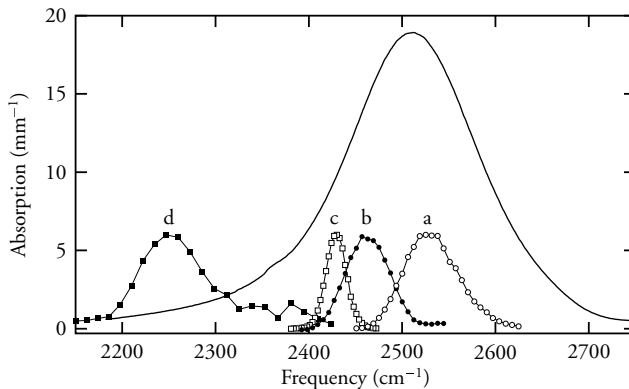


FIGURE 5.1. Absorption band of the OD stretch vibration in HDO:H₂O (solid line), corrected for the H₂O background. The data points indicate the spectra of the probe pulses, the letters a–d correspond to those in Fig. 5.2.

5.2 EXPERIMENT

The experiments were pump–probe measurements where a femtosecond infrared laser pulse excited the $\nu = 0 \rightarrow 1$ transition of the OD stretch vibration of HDO molecules dissolved in H₂O. The frequency of this transition is approximately 2500 cm⁻¹. The transmittance of a subsequent probe pulse with an independently tunable frequency is a measure of the degree of excitation of the OD groups in the solution.

The general background on pump–probe experiments is discussed in §1.2; the details of the pulse generation in §2.2.5; and the pump–probe setup in §2.4.1. The sample was a 50- μ m-thick layer of about 5% HDO in H₂O. Sample thickness and concentration were chosen such that the transmittance at the center of the OD absorption band was approximately 5%. The concentration is necessarily relatively high, compared to the concentration in the HDO:D₂O experiments in this thesis, because pure H₂O contributes significantly to the absorbance around 2500 cm⁻¹. The high HDO concentration ensures that most of the pump energy is actually used to excite the OD vibration. During the measurements, the sample was continuously rotated to avoid heating effects due to previous pulses (see also §2.8). The experiments were conducted at room temperature (298 K).

Basically, each measurement yields a transient absorbance change $\Delta\alpha(t)$ that changes with the time t after excitation of the OD stretch vibration by the pump pulse. Between measurements, we varied the pump frequency and/or probe frequency.

5.3 RESULTS

The absorption band of the OD stretch vibration is centered at 2500 cm⁻¹ and has an FWHM of 170 cm⁻¹ (see Fig. 5.1). Figure 5.2 shows the time dependence of the absorbance change $\Delta\alpha(t)$ for different pump and probe frequencies. Clearly, the pump–probe signal depends strongly on the employed frequencies.

At delays shorter than 1 ps, the signals display very complex behavior: in Figs. 5.2a

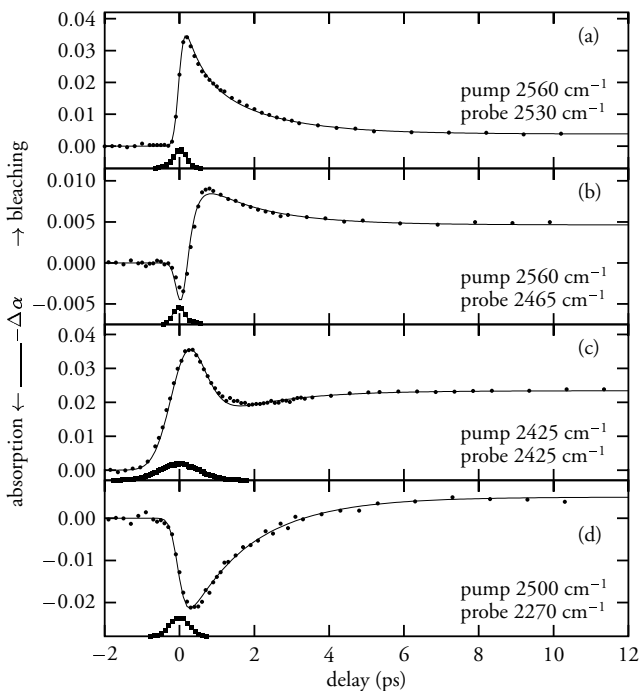


FIGURE 5.2. Measured pump-probe transients of HDO:H₂O at different pump and probe frequencies. The solid line is a fit to the data [Eq. (5.14)]. Also shown are cross-correlation traces of the pump and probe pulses.

and 5.2c, a bleaching signal is observed; Fig. 5.2d shows an induced absorption due to the $1 \rightarrow 2$ transition. In Fig. 5.2b, within 1 ps, the initial absorbance changes into a bleaching signal. The initial behavior, within ~ 1 ps after excitation, depends strongly on both pump and probe frequencies. For instance, the initial absorption at a 2465 cm^{-1} probe frequency (Fig. 5.2b) is not visible with a pump frequency of 2465 or 2500 cm^{-1} (not shown), instead of 2560 cm^{-1} . The bleaching at 2425 cm^{-1} (Fig. 5.2c) is not visible with a pump frequency of 2560 cm^{-1} ; an induced absorption appears instead. The fact that the initial behavior depends on both pump and probe frequencies, suggests that spectral diffusion significantly affects the signals at $t < 1$ ps.

More than ~ 1 ps after excitation, all signals either increase (Figs. 5.2c and 5.2d) or decrease (Figs. 5.2a and 5.2b) exponentially to a nonzero level, all with the same time constant of 1.8 ps. The persistent absorbance change at large delays is due to the temperature increase that results from the thermalisation of the pump pulse energy. Raising the temperature causes the absorption band to shift to the blue and become weaker.³¹ At most frequencies, a temperature increase leads to a decrease in absorption, except at the frequencies far in the high-frequency wing of the absorption band, where the absorption increases. The facts that, for $t > 1$ ps, all signals have an equal decay time and their signs are independent of the pump frequency, indicate that the distribution of excited OD groups over the spectrum is equilibrated due to spectral diffusion. The decay time of 1.8 ps

is therefore equal to the vibrational lifetime T_1 .

5.4 THE BROWNIAN-OSCILLATOR MODEL

To describe the pump–probe signals on a distribution of OD groups that is subject to spectral modulation, we use a modified¹²⁹ Brownian-oscillator⁸⁸ model. The Brownian-oscillator model describes the frequency modulation of an ensemble of OD groups, each of which has a certain bandwidth around a central frequency ω_B for its $\nu = 0 \rightarrow 1$ transition. The idea behind this model is that spectral diffusion of the frequency of a particle corresponds to diffusion in a harmonic potential, or ‘Brownian oscillation’ (analogous to ‘Brownian motion’) of a low-frequency coordinate. In this case, the low-frequency coordinate is the ‘hydrogen’ bond length R , i.e. the O–D···O length. In more isolated hydrogen-bonded systems, such an oscillation can take place.⁷⁸ The present model is a Brownian oscillator in the overdamped limit, which excludes oscillations in R . In thermal equilibrium, the population of the $\nu = 0$ state corresponds to an absorption spectrum

$$f_d(\omega) \propto \exp\left(-(\omega - \omega_B)/2\Delta_d^2\right), \quad (5.1)$$

where Δ_d defines the diffusive bandwidth. The fact that the excitation frequency of the OD group depends on R implies that the excited-state potential $W_1(R)$ has its minimum at a value of R that differs from that of the minimum of the ground-state potential $W_0(R)$ (see Fig. 5.3). In a pump–probe experiment, the bleaching of the $\nu = 0 \rightarrow 1$ transition depends on both the populations of the $\nu = 0$ and the $\nu = 1$ states. This means that, if the excited-state population is equilibrated within the $\nu = 1$ potential, the $\nu = 1 \rightarrow 0$ contribution to the bleaching is centered at a frequency $\omega_B - \delta\omega_{\text{sto}}$, where $\delta\omega_{\text{sto}}$ is the Stokes shift. This Stokes shift and the diffusive bandwidth Δ_d have the relation

$$\delta\omega_{\text{sto}} = \hbar\Delta_d^2/k_B T, \quad (5.2)$$

where \hbar is Planck’s constant divided by 2π and k_B is Boltzmann’s constant. If we assume that the modulation of the spectral frequency is a diffusive process, the correlation time τ_c is defined by the statistical behavior of the frequency $\omega(t)$ of an individual OD group:

$$\langle(\omega(t) - \omega_B)(\omega(0) - \omega_B)\rangle = \Delta_d^2 e^{-t/\tau_c}. \quad (5.3)$$

The absorbance change in a pump–probe experiment has three contributions: ground-state depletion, stimulated emission from the excited-state population, and excited-state absorption. These three contributions correspond to the $\nu = 0 \rightarrow 1$, the $\nu = 1 \rightarrow 0$, and the $\nu = 1 \rightarrow 2$ transitions, respectively. We assume that the pump and probe pulses have Gaussian shapes with central frequencies ω_{pu} and ω_{pr} , and RMS bandwidths Δ_{pu} and Δ_{pr} , e.g. $\exp([\omega - \omega_{\text{pu}}]^2/2\Delta_{\text{pu}}^2)$. The spectral dynamics of the bleaching signal at delay t , with pump frequency ω_{pu} and probe frequency ω_{pr} , are described by

$$B(\omega_{\text{pu}}, \omega_{\text{pr}}, t) = A [B_{01}(t) + B_{10}(t) - \sigma B_{12}(t)] \quad (t > 0). \quad (5.4)$$

where ω_{pu} and ω_{pr} are the pump and probe frequency, respectively; A is the amplitude of the signal that depends on how efficiently the pump pulse excites the Brownian oscillator

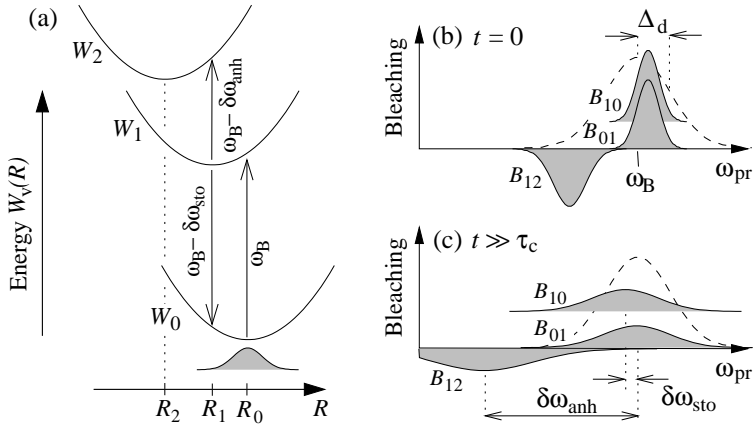


FIGURE 5.3. In (a), schematic potentials of the Brownian oscillator model. The potential energy is a parabolic function of the hydrogen bond length R for every state ν of the OH stretch vibration. The central frequency for a thermal population (shaded area) in the ground-state potential is ω_B . For a thermal population at the bottom of the $\nu = 1$ potential, the $\nu = 1 \rightarrow 0$ transition frequency has a Stokes shift $\delta\omega_{sto}$ and the $\nu = 1 \rightarrow 2$ transition frequency has an anharmonic red-shift $\delta\omega_{anh}$. The relative position of the $\nu = 2$ potential is defined by $a = (R_2 - R_1)/(R_1 - R_0)$. In (b) and (c), the contributions B_{ij} to the transient spectrum [Eq. (5.4)] are shown schematically, for a pump frequency slightly larger than ω_B . The dashed line indicates the linear absorption spectrum.

ensemble. The terms B_{ij} represent the contributions to the probe signal for the $\nu = i \rightarrow j$ transitions. Equation (5.4) does not yet incorporate vibrational relaxation. If we assume that pump and probe pulses have Gaussian spectra with standard deviations Δ_{pu} and Δ_{pr} , respectively, the components in Eq. (5.4) are

$$A = \exp\left(-(\omega_{pu} - \omega_B)^2/2(\Delta_d^2 + \Delta_{pu}^2)\right), \quad (5.5)$$

$$B_{01}(t) = D^{-1}(t) \exp\left(-[\omega_{pr} - \omega_{01}(t)]^2/2D^2(t)\right) \quad (5.6)$$

$$B_{10}(t) = D^{-1}(t) \exp\left(-[\omega_{pr} - \omega_{10}(t)]^2/2D^2(t)\right) \quad (5.7)$$

$$B_{12}(t) = D^{-1}(t) \exp\left(-[\omega_{pr} - \omega_{12}(t)]^2/2a^2D^2(t)\right) \quad (5.8)$$

$$D^2(t) = \Delta_d^2 \left(1 - \frac{\Delta_d^2}{\Delta_d^2 + \Delta_{pu}^2} e^{-2t/\tau_c}\right) + \Delta_{pr}^2. \quad (5.9)$$

The B_{01} and B_{10} contributions have identical widths $D(t)$, and the B_{12} contribution has a width $aD(t)$, where a is a scaling factor (see Fig. 5.3). The quantity σ is the relative cross-section of the $\nu = 1 \rightarrow 2$ transition as compared to the $\nu = 0 \rightarrow 1$ transition. The time-dependent frequencies $\omega_{ij}(t)$ are

$$\omega_{01}(t) = \omega_B + e^{-t/\tau_c}(\omega_{hl}^0 - \omega_B), \quad (5.10A)$$

$$\omega_{10}(t) = \omega_B - \delta\omega_{sto} + e^{-t/\tau_c}(\omega_{hl}^0 + \delta\omega_{sto} - \omega_B), \quad (5.10B)$$

$$\omega_{12}(t) = \omega_B - \delta\omega_{anh} + ae^{-t/\tau_c}(\omega_{hl}^0 + \delta\omega_{sto} - \omega_B), \quad (5.10C)$$

with the correlation time τ_c , the anharmonic shift $\delta\omega_{\text{anh}}$, and the Stokes shift $\delta\omega_{\text{sto}}$, and the initial frequency of the bleaching

$$\omega_{\text{hl}}^{\circ} = \frac{\Delta_{\text{pu}}^2}{\Delta_{\text{pu}}^2 + \Delta_{\text{d}}^2} \omega_{\text{B}} + \frac{\Delta_{\text{d}}^2}{\Delta_{\text{pu}}^2 + \Delta_{\text{d}}^2} \omega_{\text{pu}}, \quad (5.11)$$

where we assume a sample that is not optically dense. In the present chapter, we corrected for the high optical density, which means that the initial hole distribution is the product of the pump spectrum $f_{\text{pu}}(\omega)$ and the absorption spectrum $1 - T_{\text{o}}(\omega)$. The effect of this correction on the resulting hole is rather small, though. The width $D(t = 0)$ and the frequency $\omega_{\text{hl}}^{\circ}$ define the Gaussian shape of spectral hole directly after excitation. This Gaussian shaped hole is the product of the excitation spectrum and the population distribution, which are both assumed Gaussian as well. Equation (5.4) does not yet incorporate vibrational relaxation, which we include as an exponentially decaying factor in the expression

$$\Delta\alpha_{\text{B}}(\omega_{\text{pu}}, \omega_{\text{pr}}, t) = -e^{-t/T_1} B(\omega_{\text{pu}}, \omega_{\text{pr}}, t) \quad (t > 0) \quad (5.12)$$

for the absorbance change.

5.5 THERMALIZATION AND FITS

Equation (5.12) does not yet incorporate the effects of thermalization, i.e. the persistent absorbance change at larger delays that is visible in the experimental data in Fig. 5.2. We assume that thermalization is a separate term in the experimental absorbance change $\Delta\alpha$ that is proportional to the total amount of energy released by vibrational relaxation. Hence, this term reads

$$\Delta\alpha_{\text{T}}(t) = \sigma_{\text{T}} \left(1 - e^{-t/T_1}\right) \quad (t > 0), \quad (5.13)$$

where σ_{T} is an amplitude that is different for each measurement, because it depends on the probe frequency and the exact amount of absorbed pump pulse energy. Thus, the absorbance change as measured in an experiment is described by the convolution of the pump–probe pulse cross-correlate and the sum of Eqs. (5.12) and (5.13), resulting in

$$\begin{aligned} \Delta\alpha(\omega_{\text{pu}}, \omega_{\text{pr}}, t) &= \int_{-\infty}^{\infty} dt' \left[\Delta\alpha_{\text{B}}(\omega_{\text{pu}}, \omega_{\text{pr}}, t') + \Delta\alpha_{\text{T}}(t') \right] \exp\left(-\frac{(t-t')^2}{2\tau_{\text{p}}^2}\right), \quad (5.14) \end{aligned}$$

which can be evaluated numerically. The quantity τ_{p} defines the width of the pump–probe pulse cross-correlate.

All data can be described by Eq. (5.14) with the parameters in Table 5.1, as resulting from a fit. The solid lines in Fig. 5.2 correspond to the fit, which accurately describe all features of the experimental data. For example, pumping at the low-frequency side of the absorption band (2425 cm^{-1} , Fig. 5.2c) affects molecules with a short hydrogen-bond length R that corresponds to the frequency of the pump pulse (see Fig. 5.3). At short delays, the probe pulse, having the same frequency as the pump pulse, experiences a

TABLE 5.1. Fitted model parameters. The rightmost column shows the parameters for the OH stretch vibration of HDO:D₂O from Ref. 129.

Parameter		HDO:H ₂ O OD stretch	HDO:D ₂ O OH stretch
Vibrational lifetime	T_1 (ps)	1.8	0.74
Spectral correlation time	τ_c (ps)	0.40	0.5
Central frequency	ω_B (cm ⁻¹)	2520	3400
Spectral RMS deviation	Δ_d (cm ⁻¹)	72	101
Anharmonic redshift	$\delta\omega_{\text{anh}}$ (cm ⁻¹)	170	270
Stokes shift	$\delta\omega_{\text{sto}}$	24 ^b	74
R shift for $\nu = 2$ potential	a	1.4	2
Relative $\nu = 1 \rightarrow 2$ cross-section	σ	1.38	1.54

^b this value is not a fit parameter, but results from Eq. (5.2)

bleaching. However, both the $\nu = 0$ depletion ('hole') and the $\nu = 1$ population ('particle') distributions evolve in time, predominantly towards the minima of their potentials. The time evolution of the particle and hole distributions is such that the $\nu = 0 \rightarrow 1$ bleaching contributions shift out of the frequency window of the probe, while the $\nu = 1 \rightarrow 2$ absorption moves into the probe window. Both processes result in the rapid increase of $\Delta\alpha$ for $t < 1.5$ ps. At the same time, the thermalization of the vibrational excitation causes a slowly-growing ($T_1 = 1.8$ ps) negative contribution, which is superimposed on the fast initial processes resulting from spectral diffusion.

In Fig. 5.2b, the excitation frequency is at the high-frequency side of the OD absorption band, while the probe frequency is at the low-frequency side. Here, the situation is the reverse of that in Fig. 5.2c: initially, the probe experiences an induced absorption due to the $\nu = 1 \rightarrow 2$ transition. During the spectral diffusion in the first ~ 1 ps, this induced absorption contribution shifts out of the probe window, while the bleaching of the $\nu = 0 \rightarrow 1$ state shifts into the probe window. Again, the thermalization of the excitation causes a slow decay of the bleaching to an equilibrium value corresponding to a higher temperature of the sample.

5.6 DISCUSSION

The observed lifetime $T_1 = 1.8$ ps of the OD stretch vibration of HDO:H₂O is in agreement to the value of approximately 2 ps for the lifetime of the OD stretch vibration in pure D₂O that was measured by time-resolved anti-Stokes Raman experiments.²¹ The similarity of these numbers for the pure liquid and the isotopically diluted solution is quite surprising, since for the OH stretch vibration, the lifetime in pure H₂O is much shorter than in the diluted solution: ~ 200 fs versus 740 fs.⁷⁴ The latter difference can be explained from the fact that in pure H₂O, where the distance between adjacent OH groups is small, the energy of an OH oscillator is rapidly transferred to nearby oscillators. This Förster energy transfer²⁹ causes very fast spectral diffusion, and enables the vibration to find its most efficient relaxation path.¹³⁰ Comparison of the OD stretch lifetime in HDO:H₂O

(this chapter) and in pure D₂O (Ref. 21) thus seems to indicate that intermolecular energy transfer plays a much smaller role for the OD stretch vibration than for the OH stretch. The less important role of intermolecular energy transfer in the vibrational relaxation of D₂O can be at least partly explained from the somewhat smaller transition dipole moment of the OD stretch vibration.

The lifetime of the OD stretch vibration is more than twice as long as the lifetime of the OH stretch vibration. This is an interesting observation, since it conflicts with the energy-gap law,⁹¹ which states that the vibrational relaxation time is proportional to δ^{-N} , where $\delta \ll 1$ and N is the number of quanta dissipated in a particular accepting mode. For a lower-frequency vibration (e.g. the OD stretch vibration compared to the OH stretch vibration), N is generally smaller, which would imply a shorter lifetime. In this case, however, the lower-frequency OD vibration lives *longer* than the higher-frequency OH vibration. It should be noted that, in addition to energy gap considerations, there are several other effects that determine the isotope effect in the vibrational lifetime, such as coupling strengths and the density-of-states of combined accepting modes.

In most vibrational relaxation processes, the energy is not transferred to a single accepting mode, but rather to a combination of modes, that may consist of one high-frequency mode that accepts the major part of the energy (e.g. the bending mode, ~ 1450 cm⁻¹) and several low-frequency modes to compensate for the energy difference, or many low-frequency modes (e.g. the hydrogen-bond stretch mode, ~ 200 cm⁻¹). For high-frequency vibrations in the condensed phase, there are many combinations of accepting modes that match the energy to be dissipated. The sheer number of combinations may compensate for the larger number N of quanta and can therefore cause the higher relaxation rate of the OH stretch mode compared to the lower-frequency OD stretch mode.

Apparently, the number of accepting modes for the OH stretch mode in HDO:D₂O is larger than those for the OD stretch mode of HDO:H₂O by an amount sufficiently large for the OH stretch lifetime to be shorter than the OD stretch lifetime, despite the larger energy gap.

In zeolites,¹⁰ an OD stretch mode relaxes about three times as fast as an OH mode. From the temperature dependence of the vibrational lifetime, the numbers of quanta of accepting modes were determined to be 5 and 3, respectively. The energy-gap law would predict a much larger difference in lifetime than the observed factor 3. Again, the difference in the number of accepting mode combinations may explain the small difference in vibrational lifetimes.

It is not yet clear which are the accepting modes in the relaxation of an excited OD or OH stretch vibration in water. Two likely accepting modes are the HOD bending vibration, and the hydrogen-bond mode. In Chapter 4, we saw that the temperature and frequency dependence of the OH stretch lifetime for HDO:D₂O can be well explained if the relaxation involves energy transfer to the hydrogen bond. However, the Raman experiments²¹ showed that the energy relaxation of both the OH and OD stretch modes leads to a transient excitation of the bending mode. Unfortunately, in the present experiments, we are not able to determine the precise relaxation mechanism. Probably, both the HOD bending mode and the hydrogen-bond mode play a role in the relaxation mechanism.

For the OH stretch vibration of HDO:D₂O, pump-probe experiments similar to the ones discussed here yielded values for the spectral diffusion correlation time of 500 fs¹²⁹ and

700 fs.³³ (In Chapter 8, we will discuss spectral diffusion in HDO:D₂O in more detail). Since the frequency of the OH vibration is determined by the length of the hydrogen bond that binds the hydrogen atom to the oxygen atom of a nearby water molecule (see §1.1 and Fig. 8.2 on page 90) its dynamics result from the motion of the bulk D₂O molecules. In the present experiment, we studied the OD stretch vibration in a dilute solution of HDO in H₂O. The value $\tau_c = 0.40$ ps for the spectral correlation time is directly related to the motion of H₂O molecules. In measuring this value, the OD excitation serves only as a label to follow these motions. The fact that the vibrational lifetime T_1 is relatively large allows for a very precise determination of τ_c . The difference with HDO:D₂O implies that H₂O molecules show significantly faster hydrogen-bond dynamics than D₂O.

5.7 CONCLUSIONS

We performed two-color mid-infrared pump-probe experiments on the OD stretch vibration in HDO:H₂O. The data displayed the effects of spectral diffusion, which were modeled with a Brownian-oscillator model. The vibrational lifetime of the OD stretch vibration is 1.8 ps and its spectral correlation time is 400 fs. The vibrational lifetime of the OD stretch vibration is significantly longer than that of the OH stretch vibration. The spectral diffusion correlation time is shorter than previously obtained for D₂O, which means that the hydrogen-bond dynamics is faster in H₂O than in D₂O.

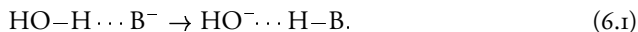
6 DYNAMICS OF WATER MOLECULES IN AN ALKALINE ENVIRONMENT

We report on two-color mid-infrared pump–probe spectroscopy experiments on the OH stretch vibration of HDO molecules in a concentrated (10 M) solution of NaOD in D₂O. The results indicate that the broad absorption band consists of two separate classes of OH groups: (I) OH groups with DO–H···OD₂-like hydrogen bonds, surprisingly similar to those in HDO:D₂O. (II) OH groups with DO–H···OD[−]-like hydrogen bonds, which show a very rapid vibrational relaxation, possibly due to deuteron transfers. For component I, the lifetime of the OH stretch vibration is observed to increase with frequency, which can be explained from the accompanying decrease in the strength of the hydrogen-bond interaction. Spectral holes can be created that change neither position nor width on a picosecond timescale. This behavior differs strongly from that of pure HDO:D₂O where rapid spectral diffusion ($\tau \approx 600$ fs) occurs. The spectral inhomogeneity indicates that, in this solution, the hydrogen bond network is very static.

6.1 INTRODUCTION

It is well-known that in solutions of salts in water, the ions are embedded in a shell that consists of a small number of water molecules. The presence of these solvation shells has a strong effect on the structure of the hydrogen-bond network that links the water molecules. For this reason, ions have been categorized as either structure-breaking or structure-making.^{30,125,126} More recently, experiments showed that water molecules in the solvation shells of negative ions (e.g. Cl[−]) behave very differently from those in bulk water.⁶² For example, the hydrogen bond length DO–H···Cl[−] varies on a much slower time scale (~ 12 ps) than the otherwise comparable hydrogen bond DO–H···OD₂ between two water molecules (~ 600 fs).^{33,129}

An interesting question is what happens if the negative ion is a base B[−] that can accept protons or deuterons from neighboring water molecules according to



Even for a weak base, the hydrogen bond between water and the base ion is much stronger than that among water molecules or between water molecules and halide ions. As a result, the difference between the hydrogen bond and the covalent O–H bond gets blurred. A special example of this blurring is when the left and right side of the reaction [Eq. (6.1)] are identical, which happens if the base is a hydroxyl (OH[−]) ion.

Figure 6.1 shows the infrared absorption spectrum of OH groups in a 10 mol/l NaOD in D₂O solution in which a small fraction of D atoms is substituted by H atoms. Here, we obtain a mixture (further denoted as ‘NaOX solution’) containing OH groups both in OH[−] ions and in HDO molecules. The high concentration of OD[−] ions has a remarkable

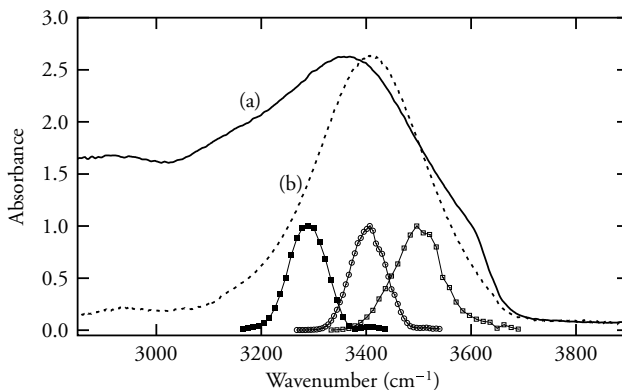


FIGURE 6.1. Absorbance ($= -\ln(T_0)$) spectra of O–H groups in (a) 10 M NaOD in D_2O in which a small fraction of D atoms is substituted by H atoms (referred to as NaOX solution). A background of a pure (unsubstituted) sample was subtracted. For comparison, (b) shows the spectrum of OH groups in HDO: D_2O . The small curves on the bottom indicate the excitation spectra used in the experiments.

effect on the OH stretch absorption band, compared to the case of HDO in D_2O (§1.1 and other chapters), with an OH stretch absorption spectrum that has a width of 270 cm^{-1} and a central frequency of 3405 cm^{-1} . Compared to water, the spectrum of the NaOX solution is strongly broadened towards lower frequencies, and shows a shoulder around 3600 cm^{-1} .

The very broad absorption spectrum of the NaOX solution is not understood in detail, but has been interpreted as follows.^{38,108} The Na^+ ions have no direct effect on the OH stretch spectrum, because water molecules do not form hydrogen bonds with these positive ions. In contrast, the OX^- ions are embedded in the hydrogen-bond network, and the OH groups can have many possible configurations with respect to their direct environment. Roughly, we can distinguish three categories for these OH groups. In the range $3200\text{--}3500\text{ cm}^{-1}$, we see the majority of HDO molecules, which donate hydrogen bonds to other HDO or D_2O molecules (as in Fig. 6.2a). This is comparable to the situation of HDO dissolved in D_2O (compare the spectra in Fig. 6.1a), except that the central frequency is shifted to a somewhat lower value. This means that hydrogen bonds are, on the average, shorter (and stronger) in the NaOX solution than in HDO: D_2O . This is not surprising, given the overall higher density of oxygen atoms at this NaOD concentration (62 mol/l , compared to 56 mol/l in plain water).

At lower frequencies, the absorption results from HDO molecules that form strong hydrogen bonds with OD^- ions (Fig. 6.2b). Depending on the exact geometry and the relevant interactions, the complex may also be described as an $HD_4O_3^-$, $HD_6O_4^-$, or $HD_8O_5^-$ complex.^{108,118,119,123,127} The OD^- ion can easily accept protons or deuterons from neighboring HDO or D_2O molecules.

Finally, the shoulder at 3600 cm^{-1} is attributed to the OH^- ions (Fig. 6.2c). OH^- ions are only weak donors of hydrogen bonds because of their negative charge.¹¹⁸ The resulting length and weakness of the $OH^- \cdots OD_2$ hydrogen bonds^{118,127} cause their frequency to be rather high.³⁸

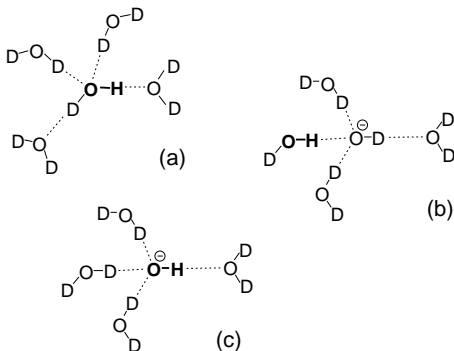


FIGURE 6.2. Different classes of OH groups in the NaOX solution. (a) $\text{DO-H} \cdots \text{OD}_2$; (b) $\text{DO-H} \cdots \text{OD}^-$; (c) $\text{DOD} \cdots \text{O-H}^-$. These are limiting cases; in reality, there may be intermediate cases as well with a more delocalized charge.

Up to now, most knowledge on the effect of OH^- ions in a liquid solution results from non-time-resolved experiments, such as infrared¹⁰⁸ and Raman⁸⁷ spectroscopy, dielectric relaxation,¹² and neutron diffraction.¹¹ Extensive data on the geometry and thermodynamic properties of the solvated OH^- ion are available from calculations; see for example Refs. 17, 99, 123, 127 and the references to experimental work therein. Direct information on the dynamics has only been provided by *ab initio* molecular dynamics simulations. These simulations showed that the structure of the hydrogen-bond network is strongly related to proton/deuteron transfer,^{118,117} and they showed also to what extent the proton is delocalized in a H_3O_2^- complex.¹¹⁹

In this paper, we study the microscopic structure and dynamics of water in a strongly alkaline solution. The method of choice is time-resolved mid-infrared spectroscopy, which will provide more knowledge on the dynamics and structure of the water molecules in this strongly alkaline environment than conventional non-time-resolved techniques.

6.2 EXPERIMENT

The experiments were pump-probe measurements where a femtosecond infrared laser pulse excited the $\nu = 0 \rightarrow 1$ transition of the OH stretch vibration in the NaOX solution. The transmittance of a subsequent probe pulse with an independently tunable frequency is a measure of the degree of excitation of the OH groups in the solution.

The general background on pump-probe experiments is discussed in §1.2, the details of the pulse generation in §2.2.4, and the pump-probe setup in §2.4.1. The sample consists of a 200 μm -thick layer of a 10 mol/l solution of NaOD in D_2O (a concentrated NaOD: D_2O solution was obtained from Sigma-Aldrich, which was appropriately diluted), in which a small amount of the deuterium was replaced by hydrogen, such that the transmittance of this sample in the range 2900–3600 cm^{-1} was approximately 4%, corresponding to a D:H ratio of about 100:1. The sample was at room temperature and at a fixed position in the laser beam focus. See §2.8 for an estimate of the thermal effects in such a sample.

In each measurement, we measured the absorbance change $\Delta\alpha(t)$ for a large number of delay values t , while we kept the pump and probe frequencies (ω_{pu} and ω_{pr} , respectively) fixed. This procedure was repeated for a number of pump and probe frequencies, which yielded a 3-dimensional data set $\Delta\alpha(\omega_{\text{pu}}, \omega_{\text{pr}}, t)$.

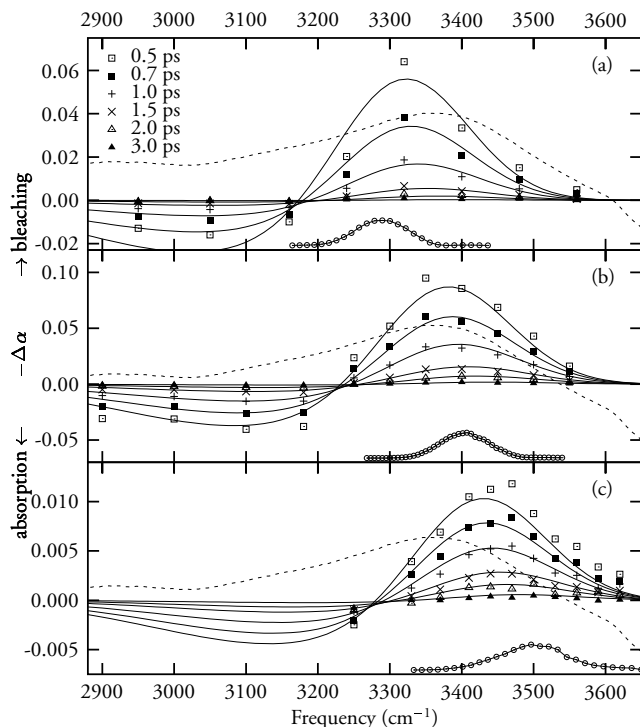


FIGURE 6.3. Transient spectra of the 10 M NaOX solution (data points) at several different pump–probe delays, for excitation at (a) 3290, (b) 3405, and (c) 3500 cm^{-1} . The data points at the bottom of each plot indicate the pump pulse spectra. The drawn curves result from Eq. (6.5) with the parameters from Table 6.1 and the dashed curves, also relative to the bottom of each plot, indicate the linear absorption spectrum (see also Fig. 6.1), that is obviously much broader than the bleaching bands.

6.3 RESULTS

6.3.1 TRANSIENT SPECTRA

By combining experimental data for different probe frequencies, we constructed transient spectra of the NaOX solution for excitation at pump frequencies $\omega_{\text{pu}} = 3290, 3405,$ and 3500 cm^{-1} . Figure 6.3 shows these transient spectra for delays $t \geq 0.5 \text{ ps}$. From these spectra it follows that the OH absorption band of the NaOX solution is strongly inhomogeneous: the bleaching signals are much narrower than the linear absorption spectrum and the frequency of the maximum bleaching signal depends strongly on the pump frequency, even at larger delay times ($\geq 2 \text{ ps}$). This means that the excitation leads to the formation of a spectral hole that persists on a picosecond timescale. This is in contrast to the situation in plain HDO:D₂O (see Refs. 33, 129 and Chapter 8), where such a strong dependence on the pump frequency exists only for delay times $< 1 \text{ ps}$.

The fact that the NaOX solution is inhomogeneous means that the absorption band in the linear spectrum in Fig. 6.1 corresponds to a population distribution function $f_i(\omega)$ that

represents the number of OH groups that absorb at a particular frequency ω . Excitation of a purely inhomogeneous system with a pump pulse spectrum $f_{\text{pu}}(\omega)$ with a nonzero width results in a spectral hole with a line shape that is the product of $f_i(\omega)$ and $f_{\text{pu}}(\omega)$. If we assume that f_i and f_{pu} are Gaussians with central frequencies ω_i and ω_{pu} and widths (defined as the standard deviation of a Gaussian) Δ_i and Δ_{pu} , respectively, the spectral hole is a Gaussian with central frequency

$$\omega_{\text{hole}} = \frac{\Delta_{\text{pu}}^2}{\Delta_{\text{pu}}^2 + \Delta_i^2} \omega_i + \frac{\Delta_i^2}{\Delta_{\text{pu}}^2 + \Delta_i^2} \omega_{\text{pu}}, \quad (6.2)$$

i.e. somewhere between ω_i and ω_{pu} , where we assume a sample with a weak absorption.^d The standard deviation of this Gaussian is $\Delta_{\text{hole}} = \Delta_i \Delta_{\text{pu}} / (\Delta_i^2 + \Delta_{\text{pu}}^2)^{1/2}$, which is narrower than both Δ_{pu} and Δ . From the cw spectra in Fig. 6.1, we estimate $\omega_i = 3370 \text{ cm}^{-1}$ and $\Delta = 170 \text{ cm}^{-1}$. With $\Delta_{\text{pu}} = 34 \text{ cm}^{-1}$ and $\omega_{\text{pu}} = 3500 \text{ cm}^{-1}$, we would expect a spectral hole centered at $\omega_{\text{hl}} = 3495 \text{ cm}^{-1}$, with $\Delta_{\text{hl}} = 33 \text{ cm}^{-1}$. This is nowhere near the experimental data in Fig. 6.3c, where the hole is centered at 3450 cm^{-1} and has a standard deviation of $\sim 98 \text{ cm}^{-1}$ (corrected for the broadening effect of the probe pulse bandwidth). Therefore, there must be a broadening effect due to a rapid spectral modulation process. In other words, an individual molecule that was excited at a particular frequency subsequently affects the transient absorption at a slightly different frequency. The timescale of this spectral modulation process must be very short, because no significant broadening occurs after 0.5 ps.

6.3.2 THE OH BAND AS A DISTRIBUTION OF BROWNIAN OSCILLATORS

To describe an inhomogeneous distribution of OH groups that is subject to spectral modulation, we use the modified¹²⁹ Brownian-oscillator⁸⁸ model, of which details are given in §5.4, although it now applies to OH groups instead of OD groups. In the absence of vibrational relaxation, the bleaching signal at delay $t \geq 0$, with pump and probe frequencies ω_{pr} and bandwidths Δ_{pu} and Δ_{pr} , is given by Eq. (5.4), which we repeat here:

$$B(\omega_{\text{B}}, \omega_{\text{pu}}, \omega_{\text{pr}}, t) = A [B_{01}(t) + B_{10}(t) - \sigma B_{12}(t)]. \quad (6.3)$$

Here, A is the amplitude of the signal that depends on how efficiently the pump pulse excites the ground-state molecules. The terms B_{ij} represent the contributions to the probe signal for the $\nu = i \rightarrow j$ transitions. Equation (6.3) describes the pump–probe signal for an ensemble of Brownian oscillators each of which has the same central frequency ω_{B} and in which there is no vibrational relaxation from the $\nu = 1$ to the $\nu = 0$ state. We saw in Chapter 4 that the vibrational lifetime T_1 depends on the OH stretch frequency ω_{B} as

$$T_1(\omega_{\text{B}}) = \tau_{\text{OH}} (1 - \omega_{\text{B}}/\omega_{\text{gas}})^{-1.8}, \quad (6.4)$$

where $\omega_{\text{gas}} = 3707 \text{ cm}^{-1}$ is the frequency of the OH stretch vibration in gas-phase HDO (Ref. 110) and τ_{OH} is a proportionality constant. To incorporate the inhomogeneous

^d For an optically thick sample (absorbance $\gg 1$), all pump energy would be absorbed, resulting in $\omega_{\text{hole}} = \omega_{\text{pu}}$ and $\Delta_{\text{hole}} = \Delta_{\text{pu}}$. In this case, the difference is negligible.

TABLE 6.1. Model parameters [Eqs. (5.1)–(5.11), (6.4)–(6.7)] for the NaOX solution. The parameter T'_I is discussed in §6.3.3. Section 6.3.4 describes how we obtained the parameter values.

Parameter		Value
Spectral correlation time ^b	τ_c	0.05 ps
Band central frequency	ω_o	3332 cm ⁻¹
Diffusive bandwidth [‡]	Δ_d	65 cm ⁻¹
Inhomogeneous bandwidth [‡]	Δ_i	77 cm ⁻¹
Anharmonic redshift	$\delta\omega_{\text{anh}}$	283 cm ⁻¹
Stokes shift	$\delta\omega_{\text{sto}}$	20 cm ⁻¹
R shift for $\nu = 2$ potential	a	2.6
$\nu = 1 \rightarrow 2$ relative cross-section	σ	1.5
Component I lifetime prefactor	τ_{OH}	6.7 fs
Component II decay time	T'_I	0.14 ps

^bAny value smaller than approximately 0.10 ps can describe the experimental data.

[‡]Bandwidths refer to standard deviations of Gaussian line shapes. To obtain the FWHM, multiply by 2.35.

character and the frequency-dependent relaxation time, we integrate Eq. (6.3) over the inhomogeneous line shape $f_i(\omega_B)$ and obtain the expression

$$S_I(\omega_{\text{pu}}, \omega_{\text{pr}}, t) = \int d\omega_B f_i(\omega_B) e^{-t/T_I(\omega_B)} B(\omega_B, \omega_{\text{pu}}, \omega_{\text{pr}}, t). \quad (6.5)$$

We assume here that, due to vibrational relaxation, the bleaching decays with a lifetime T_I . As discussed in Chapter 4, it is likely that the decay time of the bleaching is slightly longer than the ‘true’ vibrational lifetime, but in the remainder, we use the symbol T_I for the decay time of the bleaching. Since we do not have any *a priori* information on the exact composition of the linear absorption spectrum of the NaOX solution in Fig. 6.1, we use a simple Gaussian

$$f_i(\omega_B) = \exp\left(-(\omega_B - \omega_o)^2/2\Delta_i^2\right) \quad (6.6)$$

for the inhomogeneous line shape in Eq. (6.5). We find that Eq. (6.5), convolved with the pump–probe pulse cross-correlate, can very well describe the experimental data in Fig. 6.3 with the parameter values in Table 6.1.

The effect of T_I being frequency-dependent [Eq. (6.4)] is more clearly visible when we plot the bleaching signals as a function of delay. Figure 6.4 shows typical pump–probe delay scans at various $(\omega_{\text{pu}}, \omega_{\text{pr}})$ combinations. The experimental data show indeed a more rapid decay for lower probe frequencies than for higher frequencies, in both the bleaching band and the induced-absorption band. The frequency dependence of the vibrational lifetime causes the transient spectra to shift slightly towards higher frequencies with increasing delay, because the lower-frequency parts of both the bleaching bands and the induced-absorption bands decay slightly faster than their higher-frequency counterparts. This means also that the frequency with zero absorbance change shifts towards higher frequencies. This effect causes the singularities in the (logarithmically plotted) curves for $\omega_{\text{pr}} = 3250$ cm⁻¹ in Fig. 6.4b and $\omega_{\text{pr}} = 3330$ cm⁻¹ in Fig. 6.4c, which show a transition from bleaching to induced absorption. The delay value at which the bleaching and induced absorption at a particular frequency compensate each other is extremely sensitive to

the exact line shapes of the $\nu = 0 \rightarrow 1$ and $\nu = 1 \rightarrow 2$ contributions, which explains why the singularity in the experimental data and the model are at different time delays. The data for $\omega_{\text{pr}} = 3250 \text{ cm}^{-1}$ in Fig. 6.4b show an additional feature around $t = 0$ ps. The signal starts as a small induced absorption that changes into a bleaching at $t = 0$ ps. This is the effect of a negative and fast-decaying contribution that we will discuss in the next section.

6.3.3 DYNAMICS AT SMALL DELAYS

The data in Fig. 6.4 deviate strongly from single-exponential decays. Nearly all measurements show a decay that is significantly faster at small delays. This fast initial decay is also visible for high pump and probe frequencies. Hence, the frequency dependence of T_1 as described by Eq. (6.4) cannot explain this initial decay. One might think that this fast initial decay results from the spectral modulation of the Brownian oscillators. Spectral modulation implies that directly after excitation, a relatively narrow bleaching band appears in the transient spectrum, that subsequently broadens and decreases in amplitude. For equal pump and probe frequencies, the spectral modulation would thus cause an initially rapid decay of the absorbance change, since the decay is caused by both spectral diffusion and vibrational relaxation, while at larger delay times, the decay rate decreases. For pump and probe frequencies that differ, the initial decay would be slower, because then the molecules would diffuse into the spectral window of the probe: the decay caused by vibrational relaxation would (partially) be compensated. However, in many data sets where pump and probe frequencies differ, a fast initial decay is visible, comparable to the case where pump and probe are equal. Hence, spectral modulation cannot cause the the initial fast decay.

Interestingly, the initial fast decay has a rapid decay constant T_1' that is more or less independent of the pump and probe frequencies. In contrast, the amplitude of this fast component does depend on the pump–probe combination. We add the rapid decay as a phenomenological term to Eq. (6.5), which yields the absorbance change

$$\Delta \alpha(\omega_{\text{pu}}, \omega_{\text{pr}}, t) = - \left[c_{\text{I}}(\omega_{\text{pu}}) S_{\text{I}}(\omega_{\text{pu}}, \omega_{\text{pr}}, t) + c_{\text{II}}(\omega_{\text{pu}}, \omega_{\text{pr}}) e^{-t/T_1'} \right]. \quad (6.7)$$

Here, $c_{\text{I}}(\omega_{\text{pu}})$ is an amplitude factor that depends on the exact pump intensity in the focus. The amplitude factor $c_{\text{II}}(\omega_{\text{pu}}, \omega_{\text{pr}})$ is different for each curve in Fig. 6.4. We convolve the above function (defined for $t \geq 0$) with the pump–probe pulse cross-correlate in order to account for the nonzero pulse duration. Thus, Eq. (6.7) describes pump–probe signals of a phenomenological fast decaying component (further denoted as component II) and an inhomogeneous distribution of Brownian oscillators (further denoted as component I) over frequencies ω_{B} with lifetimes T_1 that depend on the frequency ω_{B} . Component I includes the $\nu = 0 \rightarrow 1$, the Stokes-shifted $\nu = 1 \rightarrow 0$, and the anharmonically red-shifted $\nu = 1 \rightarrow 2$ transitions.

From fitting the experimental data (see §6.3.4), we find that component II has a lifetime $T_1' = 140 \pm 20$ fs. Figure 6.5 shows spectra of component II, which are qualitatively similar to the transient spectra of component I, with a bleaching at high frequencies and an induced absorption at lower frequencies.

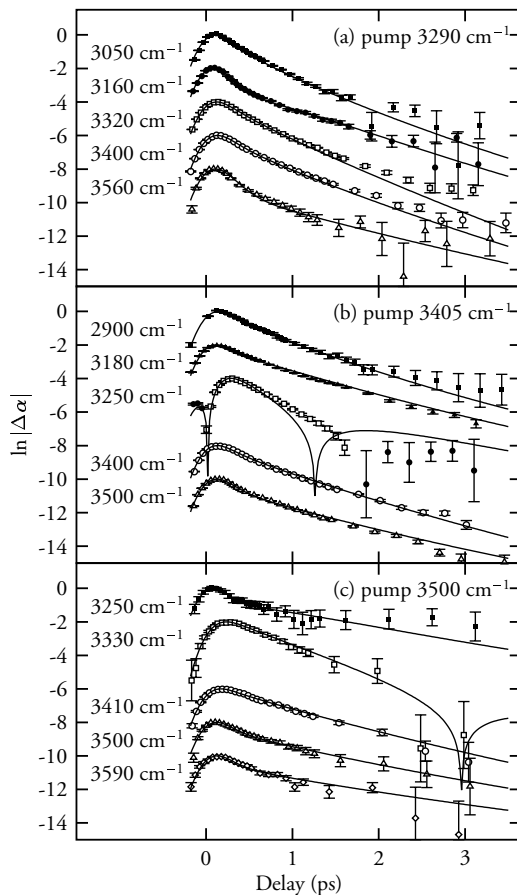


FIGURE 6.4. Pump-probe scans on the NaOX solution for a few different pump and probe pulse frequencies (data points). The data are plotted logarithmically as $\ln|\Delta\alpha|$. Data points with filled symbols correspond to induced absorption ($\Delta\alpha > 0$); open symbols correspond to bleaching ($\Delta\alpha < 0$). To aid comparison, the curves and data points are shifted vertically—the true amplitudes can be read from Fig. 6.3. The curves result from Eq. (6.7) with parameters from Table 6.1; the amplitudes of component II, which affects the signal for $t < 0.5$ ps, are shown in Fig. 6.5. For delays $t > 0.5$ ps, Eq. (6.7) and Eq. (6.5) do not differ significantly. The two curves with singularities are elucidated in the last paragraph of §6.3.2.

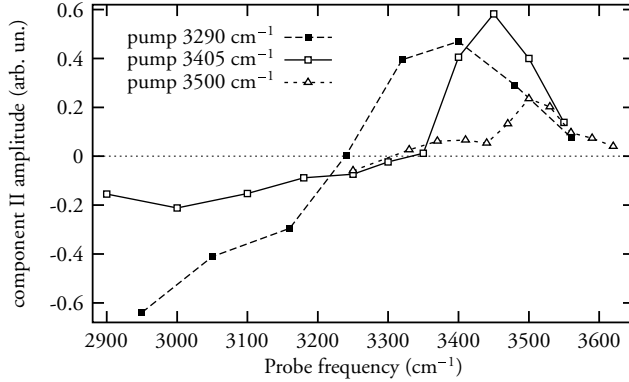


FIGURE 6.5. Transient spectra of component II, defined as the ratio c_{II}/c_I (c_I is the overall amplitude of the spectrum of component I).

6.3.4 FIT DETAILS

The parameters τ_c , $c_{II}(\omega_{pu}, \omega_{pr})$, and T_I' mainly affect the data for short delays. From the absence of broadening in time of the transient spectra in Fig. 6.3 for delays $t \geq 0.5$ ps, we conclude that the spectral correlation time τ_c [Eq. (5.3)] is shorter than the pulse duration (i.e. ~ 250 fs).

For delays $t \geq 0.5$ ps, the shapes of the transient spectra are nearly entirely determined by component I, with parameters ω_o , Δ_d , Δ_i , $\delta\omega_{anh}$, a , τ_{OH} , τ_c , and $c_I(\omega_{pu})$. The Stokes shift $\delta\omega_{sto}$ follows from Δ_d [Eq. (5.2)]. In order to determine these parameters, we did a simultaneous least-squares fit on transient spectra at a large number of delays $t \geq 0.5$ ps, while we set $c_{II} = 0$ for all data sets.

Subsequently, we used the fit results in a simultaneous fit on the transients as a function of delay time (as in Fig. 6.4), where only c_I , c_{II} , and T_I' were allowed to vary. (c_I needs only minor adjustments to account for the spatial overlap between pump and probe pulses, that is not exactly the same for different probe frequencies.)

To determine how sensitive the fit results are for the exact value of τ_c , we repeated the entire fit procedure for $\tau_c = 0.05, 0.1, 0.2$, and 0.4 ps. This yielded very similar values for the parameters in Table 6.1, but caused c_{II} to have a physically highly improbable probe frequency dependence if $\tau_c > 0.10$ ps, with zero amplitudes at the central frequencies of the bleaching bands in Fig. 6.3. By virtue of Ockham's razor, we conclude therefore that $\tau_c \leq 0.10$ ps; we used the value $\tau_c = 0.05$ ps. The formal errors in the parameters in the fits were fairly small (typically a fraction 10^{-3} of the parameter value). However, the model assumes that the pulse spectra, pulse time envelopes, and inhomogeneous and diffusive bandwidths all have ideal Gaussian shapes. The fact that the true shapes are not Gaussian is most likely a more significant, but very difficult to calculate quantitatively, source of errors. Therefore, we do not show the formal errors, because these are not representative of the true uncertainties.

6.4 DISCUSSION

In plain HDO:D₂O, spectral diffusion covers the entire OH stretch absorption band of the linear spectrum, with a correlation time of ≈ 600 fs. Such a type of spectral diffusion is completely absent in component I of the NaOX solution, where the absorption spectrum is inhomogeneously broadened on at least a picosecond timescale. This means that the hydrogen-bond network, which is the main responsible for the spectrum of the OH stretch vibration, is effectively immobilized due to the presence of a high concentration of Na⁺ and OX⁻ ions. Neutron diffraction experiments¹¹ recently showed that the O–O radial distribution function, which is related to the structure of the NaOX solution, is indeed very different from that of water. Apparently, the disturbed structure of the hydrogen-bond network allows only small fluctuations, that are very rapid, judging from the nearly instantaneous broadening of the spectral holes. The NaOX solution has a high density (62 M O atoms) with respect to plain water (56 M O atoms). However, this high density is not likely the direct cause of the slow hydrogen-bond dynamics; from the compressibility $\kappa = 45 \times 10^{-6} \text{ bar}^{-1}$ (Ref. 72) of water, we can estimate that water reaches a 62 M O-atom density at a pressure of 2.6 kbar. From the neutron diffraction data,¹¹ the equivalent pressure was estimated to be even higher, 9 kbar. However, the reorientation time of water, that is closely related to the hydrogen-bond dynamics (changing the orientation of a water molecule requires stretching and/or breaking its hydrogen bond, see Chapter 7) changes by only $\sim 17\%$ going from ambient pressure to 4 kbar, or by 20% at 9 kbar.⁵⁵ This small effect of the density is confirmed by the behavior of the viscosity. The viscosity of water, also related to the making and breaking of hydrogen bonds, increases by 20% and 80% for 4 and 9 kbar, respectively.⁵⁵ The viscosity of a 10 M NaOH solution is a factor 13.5 larger than the viscosity of pure water.⁷² These considerations suggest that high charge density, rather than the high particle density, is responsible for the absence of sub-picosecond hydrogen-bond dynamics.

Additional support for the observed absence of hydrogen-bond dynamics is provided by data on the reorientation of OH groups in the NaOX mixture. We performed polarization-resolved measurements similar to the pump–probe delay scans in Fig. 6.4 on a 10 M NaOX solution, where we excited with a pump frequency of 3400 cm^{-1} and measured the absorbance change $\Delta\alpha(t)$ separately for parallel (\parallel) and perpendicular (\perp) probe polarizations. From these data, we calculated the rotational anisotropy,

$$A(t) = \frac{\Delta\alpha_{\parallel}(t) - \Delta\alpha_{\perp}(t)}{\Delta\alpha_{\parallel}(t) + 2\Delta\alpha_{\perp}(t)}. \quad (6.8)$$

The pump pulse preferentially excites OH groups that are approximately parallel to the polarization of the pump pulse, such that $A = 0.4$ at $t = 0$. The decay of A indicates to what extent the OH groups can change reorientation; free orientation motion would result in $A \rightarrow 0$. More details on this polarization-resolved technique will be discussed in Chapter 7. Figure 6.6 shows the decay of the anisotropy for probe frequencies centered at 3400 and 3280 cm^{-1} . Clearly, the decay of the anisotropy is limited to a small decrease at delays $t \lesssim 0.5$ ps, which indicates that each individual OH group can only change its orientation within a limited angular range. This observation is in contrast to similar experiments on HDO dissolved in D₂O, which we will discuss in detail in Chapter 7. In HDO:D₂O, the anisotropy decays with a time constant of 2.6 ps. The present limited

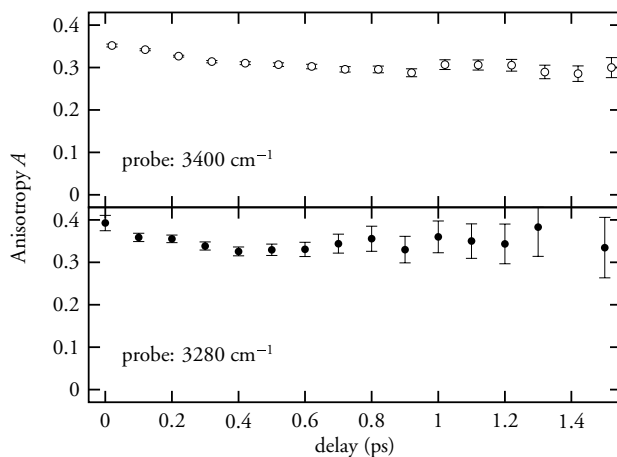


FIGURE 6.6. Rotational anisotropy of the 10 M NaOH mixture pumped at 3400 cm^{-1} . Only at small delays, a very small decay of the anisotropy is visible, after which the anisotropy stays nearly constant.

decay of the anisotropy is in agreement with the observed absence of hydrogen-bond dynamics, since large changes in the orientation of an OH group must involve stretching, making, and/or breaking of hydrogen bonds. We can therefore regard the structure of the hydrogen-bond network as a ‘gel’-like state.

The small and rapid fluctuations in the immobilized hydrogen-bond network in the NaOH solution are represented by the Brownian-oscillator model [Eq. (6.5)]. These fluctuations cause a spectral modulation with a correlation time τ_c and an (unknown) amplitude Δ_m around the central frequency ω_B of each OH group. This spectral modulation results in an almost instantaneous broadening of the spectral holes; the line shape of this broadening has a width defined by Δ_d . We remark that our modelling assumes a relatively slow spectral modulation, i.e. the quantity $\epsilon \equiv \tau_c \Delta_m$ is $\gg 1$, in which case $\Delta_m \approx \Delta_d$. However, the value range $\tau_c \leq 100\text{ fs}$ implies that $\epsilon \leq 1.2$. Therefore, the interpretation of Δ_d requires additional attention. It is impossible to know from the present experimental data whether (1) $\epsilon \ll 1$ or (2) $\epsilon \approx 1$. Case (1) would mean that the line shape of the broadening is the Lorentzian $(1 - \omega^2/\Delta_h^2)^{-1}$ with a half-width $\Delta_h = \epsilon \Delta_m$, which is narrower than Δ_m due to motional narrowing. In this limit, we should compare the value $\Delta_d = 65\text{ cm}^{-1}$ to the homogeneous broadening Δ_h due to pure dephasing (commonly written as $\Delta_h = 1/T_2^*$), with the remark that the present model assumes Gaussian line shapes instead of Lorentzian line shapes. Homogeneous broadening is always instantaneous and not dependent on the pump-probe delay. In this case, Δ_m is unknown because it depends on the unknown value of τ_c . Case (2) is the intermediate modulation regime, where the line broadening is almost instantaneous and the line shape of the broadening is between a Gaussian and a Lorentzian, with width defined by Δ_d , with $\Delta_d < \min(\epsilon, 1)\Delta_m$.

Recently, infrared photon-echo experiments¹¹⁵ showed that the absorption band of the OH stretch vibration of HDO in D_2O contains a homogeneously broadened component

with a half-width $\Delta_h = 60 \text{ cm}^{-1}$, where it was estimated that $\tau_c \sim 30 \text{ fs}$. Likely, the rapid fluctuations that are responsible for the instantaneous broadening in the NaOX solution are of the same nature as those causing the homogeneous broadening in HDO:D₂O. This is in good agreement with our finding that $\tau_c < 100 \text{ fs}$ and $\Delta_d = 65 \text{ cm}^{-1}$. This homogeneous broadening can also explain why Eq. (6.5) systematically yields amplitudes that are too small at the high-frequency side of the transient spectra in Fig. 6.3: the tails of a Gaussian lineshape (as in the model) are smaller than those resulting from $\epsilon \sim 1$. However, it is not likely that the line shape is purely homogeneously broadened ($\epsilon \ll 1$), since the resulting Voigt lineshape [i.e., a convolution of a Lorentzian with a half-width of 65 cm^{-1} (due to spectral modulation) and Gaussian with a half-width of 77 cm^{-1} (due to the inhomogeneous distribution)] would have a significant absorbance around 3700 cm^{-1} in the linear spectrum.

Apparently, component II consists of a class of OH groups that differ from those in component I in that they have a very fast vibrational relaxation ($\sim 0.14 \text{ ps}$). Their transient spectra (Fig. 6.5) show both bleachings and induced absorptions at frequencies similar to those of component I (curves in Fig. 6.3), which suggests that these OH groups have O–H···O hydrogen bond lengths similar to those of component I. Therefore the mechanism of vibrational relaxation of component II must be different from that of component I or that of water (see Chapter 4). Since, apart from the absence of spectral diffusion, component I behaves similarly to HDO in D₂O, it is likely that component I corresponds to HDO molecules that are hydrogen bonded to D₂O molecules (Fig. 6.2a). Component II is likely related to OH groups of HDO molecules that are hydrogen-bonded to OD[−] ions, as in Fig. 6.2b. According to *ab initio* molecular dynamics simulations on the solvation of OD[−] (Ref. 117, 118), there are two solvation structures of the OD[−] ion: (a) D₉O₅[−], which is relatively stable, and (b) D₇O₄[−], in which rapid deuteron hopping can occur. Structures (a) and (b) transform into each other typically every 2–3 ps. The deuteron transfers in structure (b) occur typically with intervals of 40–100 fs and require only very small changes of the positions of the individual oxygen atoms. At each deuteron transfer, a D₂O molecule is transformed into an OD[−] ion (and vice versa), which effectively changes the position of the complex in the global hydrogen bond network, since with each hop, one D₂O molecule leaves the complex and another enters. Such a deuteron transfer has a strong impact on any excited OH vibrations in participating HDO molecules, as the hydrogen bonds inside the complex are shorter ($R = 2.6 \text{ \AA}$) than between the surrounding water molecules (2.8 \AA). This change in hydrogen-bond length corresponds to large jumps in the OH frequency, and is apparently accompanied by a rapid vibrational relaxation. Since this mechanism means that excitation at 3030 cm^{-1} should result in a bleaching at much higher frequencies, we have done an experiment in which we excited the NaOX solution at 3030 cm^{-1} and where we probed at 3330 cm^{-1} (Fig. 6.4). Indeed, the excitation results in a bleaching that decays rapidly, with a rate comparable to that of component II. This provides support for the hypothesis that component II consists of HDO molecules that are affected by deuteron hopping.

It is interesting to note that the linear absorption spectrum in Fig. 6.1 is much wider ($\sim 400 \text{ cm}^{-1}$ FWHM) than one would expect from the convolution of the diffusive and inhomogeneous bandwidths of component I (i.e. 235 cm^{-1} FWHM). This is in agreement with the picture that component II has a very broad spectral distribution that apparently contributes significantly to the linear spectrum. Further, the fact that the components I

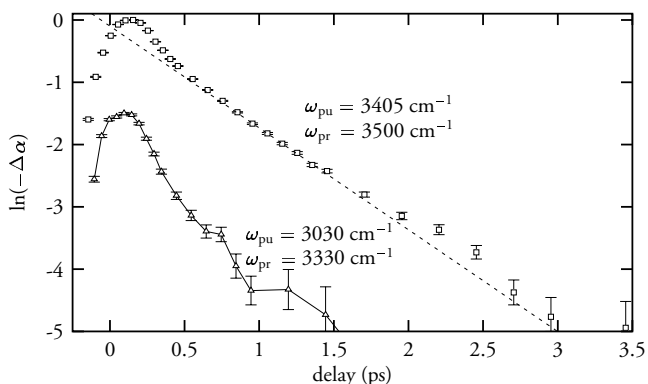


FIGURE 6.7. Pump-probe transients with different pulse frequencies. Pumping at 3030 cm^{-1} results in a bleaching at 3330 cm^{-1} that has a decay rate comparable to component II. The line is a guide to the eye to indicate a purely exponential decay ($\tau = 0.61\text{ ps}$).

and II are so distinctly visible in the experimental data suggests that very little exchange between component I and II occurs, even though there is one OX^- ion available for every 5.6 water molecules, of which 3 or 4 are needed to form the HD_6O_4^- or HD_8O_5^- complexes. It seems therefore that the deuteron exchange in component II is confined to certain regions in the hydrogen bond network, and that deuteron exchange is not possible to other regions, that constitute component I.

Of course on a longer timescale exchange does occur, which may be responsible for the fact that, for equal frequencies, the vibrational lifetime T_1 of component I is somewhat faster than in $\text{HDO}:\text{D}_2\text{O}$, i.e. 0.6 ps versus 0.74 ps , both at 3400 cm^{-1} . A small amount of exchange would not be directly visible in the transient spectra in Fig. 6.3, since any excited OH group that switches from component I to component II would disappear almost instantaneously due to the fast relaxation of component II. Vice versa, the bleaching signal of component II does not live long enough to influence component I significantly.

6.5 CONCLUSIONS

We have shown that the linear absorption spectrum of the OH stretch vibration of HDO molecules in a 10 M NaOD in D_2O solution consists of two components. Component I consists of HDO molecules that are hydrogen bonded as $\text{DO}-\text{H}\cdots\text{OD}_2$ (Fig. 6.2a). These differ from HDO molecules dissolved in D_2O , because the OH groups in component I do not show slow spectral diffusion ($\tau_c \approx 600\text{ fs}$ for $\text{HDO}:\text{D}_2\text{O}$), they have a lower central frequency (3332 cm^{-1} instead of 3400 cm^{-1}), and they have a vibrational relaxation rate that is slightly faster. Component II consists of HDO molecules such as in Fig. 6.2b, that participate in deuteron hopping between OD^-/OH^- ions and $\text{HDO}/\text{D}_2\text{O}$ molecules, which is accompanied by large jumps in the frequency. These molecules show a very rapid vibrational relaxation. The difference in vibrational relaxation rates between HDO in D_2O and HDO in the NaOX solution suggests that there is a small amount of exchange between components I and II. This small amount of exchange and the absence

of spectral diffusion in component I on the experimental picosecond time scale show that the structure of the hydrogen bond network is very static in the NaOX solution.

7 ORIENTATIONAL RELAXATION OF HDO:D₂O AS AN ACTIVATED PROCESS

The orientational relaxation of HDO molecules dissolved in liquid D₂O is studied with polarization-resolved pump-probe experiments. The excitation of the OH stretch vibration is used as a label in order to follow the orientational motion of the HDO molecules in time. The decay of the anisotropy is nonexponential with a typical time scale of 1 ps and can be described with a model involving both a reorientation rate that depends on the OH stretch frequency and spectral diffusion. The dependencies of the anisotropy decay on frequency and temperature provide information on the activation energy for reorientation. This activation energy increases with the hydrogen bond strength.

7.1 INTRODUCTION

Oriental diffusion of water molecules is likely to be related to hydrogen-bond breaking and formation, since a hydrogen bond is directional, i.e. the O–H···O group is approximately linear.⁷⁵ The orientation vector of a particle that is subject to orientational diffusion changes by 1 rad typically in a time $3\tau_r$, where τ_r is the orientational correlation time. (See §7.6.1 for an exact definition.) Already in 1929, Debye^{2,22} used the viscosity $\eta \approx 10^{-3}$ Pa·s of water and the radius $a \approx 2 \text{ \AA}$ of a water molecule for the estimate

$$\tau_r = 3\tau_r = \frac{4\pi a^3 \eta}{k_B T} = 25 \text{ ps}, \quad (7.1)$$

at $T = 293$ K. This equation is now known as the Debye-Stokes-Einstein equation. Debye formulated a theory that relates the time constant τ_r (now known as the Debye time) to the dependence of the dielectric constant ϵ of a liquid medium on frequency ω ,

$$\epsilon(\omega) = \epsilon(\infty) + \frac{c}{1 - i\omega\tau_r}. \quad (7.2)$$

From the dielectric properties in the microwave (GHz) range, τ_r can be estimated to be 8.1 ps, as mentioned by Bloembergen in 1948.⁴ Bloembergen showed on theoretical grounds that reorientation constitutes a major contribution to the relaxation time of the proton spin in NMR experiments on liquid water. The theoretical relationship between the experiment and the underlying orientational (and translational) diffusion of water molecules involves a number of microscopic parameters that are difficult to estimate. Since Bloembergen, the reorientation time τ_r of water (H₂O) has been estimated in NMR experiments with values ranging from 1.7 to 2.8 ps.^{41,50,53,55,68,111} This reorientation time decreases with temperature due to the increased thermal energy that is available, in a way that cannot be described by Eq. (7.1), which suggests that it is an activated process that might be

described by the Arrhenius equation

$$\frac{1}{\tau_r(T)} = \frac{1}{\tau_{r,0}} e^{-E_{\text{act}}/k_B T}, \quad (7.3)$$

where E_{act} is the activation energy. However, the observed temperature dependence of τ_r shows a small, but significant deviation from a pure Arrhenius behavior. The temperature dependence is described more accurately by the fractional power law^{50,104}

$$\frac{1}{\tau_r(T)} \propto (T/T_s - 1)^\gamma, \quad (7.4)$$

where $T_s \approx 228$ K and $\gamma \approx 1.78$, which is equivalent to an activation energy that decreases with increasing temperature. Equation (7.4) was originally based on measurements of thermodynamic properties such as the isothermal compressibility and the density, that can all be described by the same critical temperature $T_s = 228$ K.¹¹² In NMR, reorientation on a picosecond timescale results in a proton spin relaxation time that is on the order of seconds. It is clear that such a measurement concerns the average reorientation time over long timespans. It does not provide information on whether the orientational motion of a water molecule is truly a diffusive process, or occurs in relatively large jumps.

More recently, experimental techniques became available that act on a timescale comparable to the reorientation time, contrary to the relatively low frequencies (10^8 – 10^9 Hz) employed in NMR and older dielectric measurements. For example, Eq. (7.2) has been applied to measurements at THz frequencies, where the oscillation period of the electric field is comparable to the Debye time. These measurements showed that water has actually *two* simultaneous Debye processes, with time constants τ_1 of 8 and 0.2 ps.⁵⁷ The time constant of the slower component has a temperature dependence satisfying Eq. (7.4).^{104,103} This two-component structure was also observed in optical Kerr effect studies, with time constants of 0.5 and 1.7 ps.^{16,96} However, it was not clear to what structural relaxation processes, amongst them reorientation, these time constants exactly apply. More recently, similar experiments did show an orientational decay with $\tau_r = 0.9$ and 3 ps.¹²⁸

Pump–probe experiments on the OH stretch vibration make it possible to directly follow the reorientation of water molecules in time. Moreover, it is possible to probe selectively those molecules with either strong or weak hydrogen bonds. The first experiments of this kind on water employed 250 fs pulses and showed distinct time constants τ_r of 700 fs and 13 ps.¹³² The component with the shorter time constant was predominantly visible at the high-frequency side (3500 cm^{-1}) of the OH stretch absorption band, and was completely absent at the low-frequency side of the absorption band. In another recent study, it was found that the reorientational time constant varied from 3.0(1.5) ps at 3500 cm^{-1} to 13(5) ps at 3330 cm^{-1} .⁶⁷ In this study, however, 2 ps pulses were employed, which renders the determination of short time constants more difficult.

It must be noted that different experimental techniques act on different orientation vectors \mathbf{e} with respect to the molecule frame. In pump–probe experiments on the OH stretch vibration, as in this thesis, \mathbf{e} coincides with the O–H bond in an HDO molecule. In proton-NMR experiments, \mathbf{e} is the HH vector of a water molecule. Dielectric relaxation measurements refer to the dipole moment vector of an H₂O molecule. The orientational diffusion constants for these vectors may differ slightly from each other; they correspond to the eigenvalues of the orientational diffusion tensor.¹³⁸

This chapter presents a detailed study on the orientational motion of HDO molecules in liquid D₂O. We describe the experimental results with a model that includes the effects of spectral relaxation. By varying the temperature, we obtain information on the activation energy that limits the rate of reorientation.

7.2 EXPERIMENT

The difference between the experiments described here and in Chapter 4 concerns only the way the data is treated. The experiments were pump–probe measurements where a femtosecond infrared laser pulse excited the $\nu = 0 \rightarrow 1$ transition of the OH stretch vibration of HDO molecules dissolved in D₂O. The probe pulse has a polarization of 45 deg with respect to the pump pulse polarization; the difference in transmittance between the parallel and perpendicular component enables a measurement of the rotational anisotropy. The general background on pump–probe experiments is discussed in §1.2, the details of the pulse generation in §2.2.3, and the pump–probe setup in §2.4.2.

Directly after excitation, the population of excited molecules per unit of solid angle will be proportional to $\cos^2 \theta$, where θ is the angle between the O–H bond and the pump polarization. Due to this anisotropic population of excited molecules, the absorbance changes for probe parallel to pump and perpendicular to pump are different: $\Delta\alpha_{\parallel}/\Delta\alpha_{\perp} > 1$. From $\Delta\alpha_{\parallel}$ and $\Delta\alpha_{\perp}$, we can calculate the rotational anisotropy⁴⁴

$$A = \frac{\Delta\alpha_{\parallel} - \Delta\alpha_{\perp}}{\Delta\alpha_{\parallel} + 2\Delta\alpha_{\perp}}. \quad (7.5)$$

The denominator here corresponds to the isotropic absorbance change, that is not affected by reorientation. For the initial $\cos^2 \theta$ distribution, it can be shown that $A = 2/5$. As this highly anisotropic distribution becomes more and more isotropic as a result of reorientation of the individual HDO molecules, the value of A decays to zero with the time constant τ_r (§7.6.1). By measuring A as a function of the delay between pump and probe pulses, we obtain information on the orientational motion of the HDO molecules. See also §2.7.1 for details on evaluating Eq. (7.5) with high accuracy. Note that A is not affected by the relaxation of excited molecules to the ground state, since this affects the numerator and the denominator of Eq. (7.5) in the same way.

The probe and pump pulses have equal frequencies. The sample was a 500 μm -thick layer of a HDO:D₂O solution in a sample cell that was continuously rotated to eliminate local accumulation of heat (§2.8) and that was equipped with a heater that enabled us to control the sample temperature within 1 K.

7.3 RESULTS

Figure 7.1 shows a typical measurement of the transmittance changes $T_{\epsilon}/T_{\epsilon}^{\circ}$ and D/D° in HDO:D₂O as a function of the delay between the pump and probe pulses. We repeated these measurements as a function of both the temperature (in the range 298–362 K) and the pulse frequency (3400 and 3500 cm^{-1}).

Due to scattered light from the pump pulses, the data in Fig. 7.1 have a significant background. As is clear from Eq. (7.5), any tiny background contribution has a large

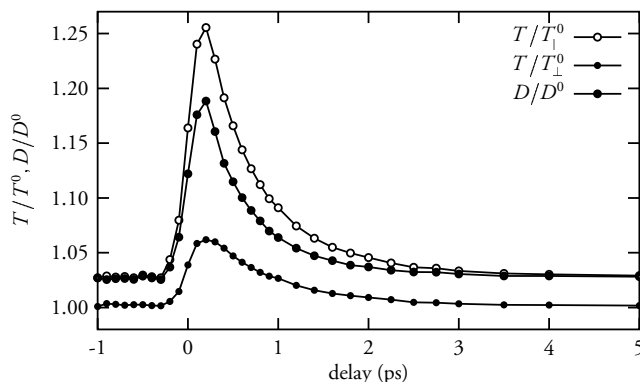


FIGURE 7.1. Raw data of $T_{\parallel}/T_{\parallel}^0$, T_{\perp}/T_{\perp}^0 and D/D^0 (see §2.7.1). The frequency was 3400 cm^{-1} and the temperature was 298 K. The different background levels are caused by scattered light from the pump pulses. The smooth increase of the signal around $t = 0$ ps is caused by the nonzero pulse duration.

effect on the value of the rotational anisotropy A . Since the bleaching decays with a time constant of 850 fs (Chapter 4) the residual bleaching at $t = 5$ ps is of the same magnitude as the error in the data points. In order to evaluate the background with the highest possible accuracy, we assumed an exponential decay of the raw T/T^0 values in Fig. 7.1 in the range 1.5–5 ps. The assumption of exponential decay is justified, since the resulting rotational anisotropy A in Fig. 7.2 decays exponentially for $t > 1.5$ ps.

The data in Fig. 7.2 display several facts. (i) This decay is faster in the experiments at 3500 cm^{-1} than in the experiments at 3400 cm^{-1} . (ii) The decays are not exponential, which is best visible at delay times less than 1.5 ps. (iii) The decay of the rotational anisotropy becomes faster as the temperature increases.

7.4 ACTIVATED REORIENTATION AND SPECTRAL DIFFUSION

7.4.1 MODEL

The frequency dependence of the anisotropy decay suggests that the reorientation rate of an individual molecule depends on its resonance frequency. This can be expected in view of the relation between OH stretch frequency and hydrogen bond strength: a higher OH vibration frequency implies a weaker hydrogen bond,^{85,92} which must lead to a larger freedom for the OH group to change its orientation. Since it is likely that, in order to change its orientation, a water molecule must stretch or break the hydrogen bond, this activation energy E_{act} is expected to decrease with increasing OH stretch frequency ω . The reorientation time τ_r should satisfy Eq. (7.3) where E_{act} is replaced by $E_{\text{act}}(\omega)$, which results in a frequency-dependent reorientation time $\tau_r(\omega)$. The prefactor $\tau_{r,0}$ is an indication for the reorientation time in absence of any activation energies, i.e. the gas-phase rotation time. For an HDO molecule at 298 K, the classical angular frequency corresponding to a rotational energy of $k_B T$ is approximately 10 ps^{-1} .

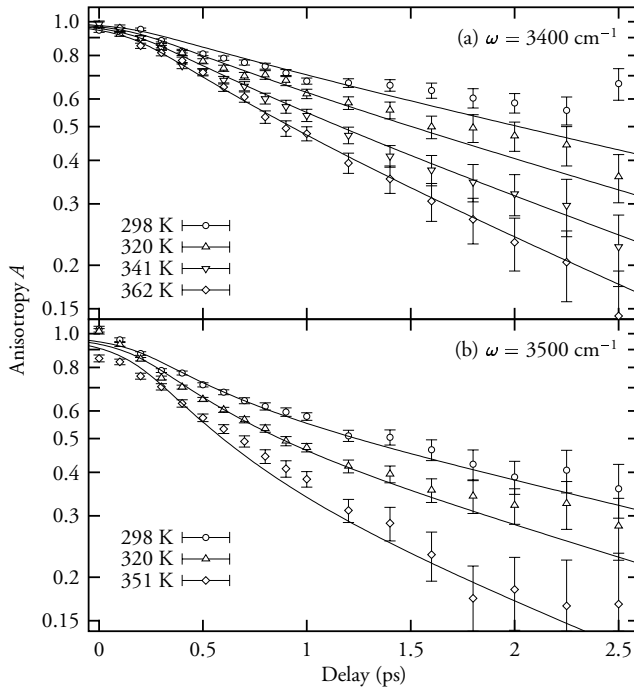


FIGURE 7.2. The decay of the rotational anisotropy A in HDO:D₂O for a series of temperatures, measured at excitation frequencies 3400 and 3500 cm^{-1} . The data are normalized at $t = 9$ ps. The lines represent our model calculations, discussed in §7.4.

A frequency dependence of the reorientation time τ_r cannot provide a complete description of the observed reorientation in water, since the OH stretch frequencies of individual HDO molecules fluctuate rapidly in time. (See also Refs. 33, 129 and Chapter 5.) We must therefore incorporate this spectral diffusion process into our model. We assume that we can describe the spectral diffusion by the Brownian-oscillator model in §5.4.^d The spectral diffusion has a correlation time τ_c that is 500 fs according to Ref. 129 or 700 fs according to Ref. 33.

The combination of spectral diffusion and a frequency-dependent reorientation rate is too complicated for an analytical treatment such as in Eq. (5.4). Therefore, we used numerical methods to evaluate the reorientational dynamics. The absorbance changes in Eq. (7.5) depend on the difference in population of the vibrational ground and excited state before and after the pump pulse. Equation (1.3) described the absorbance change for a probe polarization ε , which depends on the orientational distribution parameter ξ_ε . Due to the Stokes shift, the spectral relaxation of the n_o population differs from that of the n_i population. Hence, we refine Eq. (1.3) to account for the different frequency- and time-dependent contributions of the ground-state depletion $-\Delta n_o(\omega, t)$ and the excited-state

^d Section 5.4 discusses the spectral relaxation of the OD stretch vibration. It applies to the present chapter up to Eq. (5.3), if one reads 'OH' for every occurrence of 'OD'.

population $\Delta n_i(\omega, t)$, which gives us

$$\Delta \alpha_\varepsilon(\omega, t) = \bar{\sigma} e^{-t/T_1} [\Delta n_o(\omega, t) \xi_{o,\varepsilon}(\omega, t) + \Delta n_i(\omega, t) \xi_{i,\varepsilon}(\omega, t)], \quad (7.6)$$

where $\bar{\sigma}$ defines the amplitude of the bleaching [see also Eq. (1.6)]. If we take the spectrum and duration of the probe pulse into account, we can write the measured rotational anisotropy as

$$A(t) = \frac{\int I_{\text{probe}}(\omega, t) * [\Delta \alpha_{\parallel}(\omega, t) - \Delta \alpha_{\perp}(\omega, t)] d\omega}{\int I_{\text{probe}}(\omega, t) * [\Delta \alpha_{\parallel}(\omega, t) + 2\Delta \alpha_{\perp}(\omega, t)] d\omega}, \quad (7.7)$$

where $I_{\text{probe}}(\omega, t)$ is the power spectrum of the probe pulses at time t and the $*$ operator indicates time convolution. For the analysis, it is more convenient to write

$$\Delta \alpha_{\parallel}(\omega, t) - \Delta \alpha_{\perp}(\omega, t) = \bar{\sigma} [a_-(\omega, t) + b_-(\omega, t)], \quad (7.8A)$$

$$\Delta \alpha_{\parallel}(\omega, t) + 2\Delta \alpha_{\perp}(\omega, t) = \bar{\sigma} [a_+(\omega, t) + b_+(\omega, t)], \quad (7.8B)$$

where a_{\pm} and b_{\pm} are defined as

$$a_-(\omega, t) = \Delta n_o(\omega, t) [\xi_{o,\parallel}(\omega, t) - \xi_{o,\perp}(\omega, t)], \quad (7.9A)$$

$$b_-(\omega, t) = \Delta n_i(\omega, t) [\xi_{i,\parallel}(\omega, t) - \xi_{i,\perp}(\omega, t)], \quad (7.9B)$$

$$a_+(\omega, t) = \Delta n_o(\omega, t) [\xi_{o,\parallel}(\omega, t) + 2\xi_{o,\perp}(\omega, t)], \quad (7.9C)$$

$$b_+(\omega, t) = \Delta n_i(\omega, t) [\xi_{i,\parallel}(\omega, t) + 2\xi_{i,\perp}(\omega, t)]. \quad (7.9D)$$

The excitation by the pump pulse, spectral diffusion, and reorientation, affect a_{\pm} and b_{\pm} according to the partial differential equations

$$\frac{\partial a_-}{\partial t} = \frac{2}{5} I_{\text{pump}}(\omega, t) + \mathcal{D}_o a_- - \frac{a_-}{\tau_r(\omega)}, \quad (7.10A)$$

$$\frac{\partial b_-}{\partial t} = \frac{2}{5} I_{\text{pump}}(\omega, t) + \mathcal{D}_1 b_- - \frac{b_-}{\tau_r(\omega)}, \quad (7.10B)$$

$$\frac{\partial a_+}{\partial t} = I_{\text{pump}}(\omega, t) + \mathcal{D}_o a_+, \quad (7.10C)$$

$$\frac{\partial b_+}{\partial t} = I_{\text{pump}}(\omega, t) + \mathcal{D}_1 b_+. \quad (7.10D)$$

Here, $I_{\text{pump}}(\omega, t)$ is the normalized pump intensity (the absolute magnitude is not relevant, since this does not affect the value of A). The operators \mathcal{D}_o and \mathcal{D}_1 act on ω and describe spectral diffusion in the $\nu = 0$ and $\nu = 1$ states (See §7.6.2 for details). The coefficient $2/5$ in Eqs. (7.10a–b) ensures that the initial anisotropy is $2/5$ in absence of spectral diffusion and orientational relaxation. Equations (7.10) are integrated numerically. Using the solutions of Eqs. (7.10), we calculate the decay of the measured anisotropy A in Eq. (7.7). We find that the experimental data can be well described if the activation energy E_{act} depends on the frequency as

$$E_{\text{act}}(\omega) = \begin{cases} 600 + 1.81(3675 - \omega) & (\omega \leq 3675) \\ 600 & (\omega \geq 3675) \end{cases}, \quad (7.11)$$

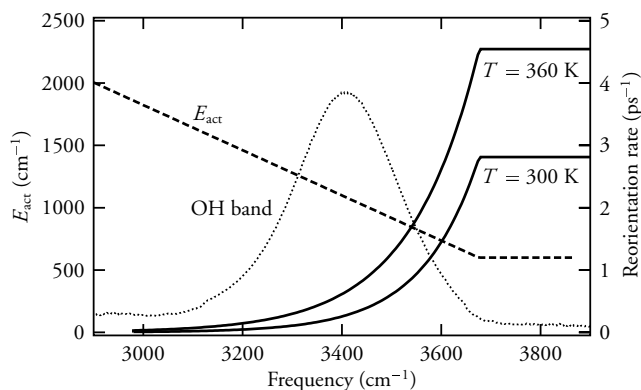


FIGURE 7.3. Reorientation rate, defined as $1/\tau_r$, at 300 and 360 K (solid lines, right-hand scale), the rotational activation energy as a function of the OH stretch frequency (dashed line, left-hand scale), and the shape of the OH absorption band (dotted line). To convert cm^{-1} to J/mol , multiply by 11.96.

where E_{act} and ω are expressed in cm^{-1} units.[†] The constant of 600 cm^{-1} corresponds to the activation energy caused by effects such as steric hindering and other hydrogen bonds that do not affect the OH stretch frequency. The 3675 cm^{-1} cut-off frequency is approximately equal to the gas-phase frequency where no $\text{DO}-\text{H}\cdots\text{O}$ hydrogen bond is present. Furthermore, the pre-exponential time constant is $\tau_{r,0} = 20 \text{ fs}$, which is of the same order as the thermal rotation time of 100 fs in the gas phase.

The resulting frequency and temperature dependence of the reorientation rate in Fig. 7.3 increases rather steeply. It is not possible to describe the experimental results with a smoother frequency dependence of the reorientation rate. Further, we describe the spectral diffusion with a 60 cm^{-1} Stokes redshift and a spectral correlation time $\tau_c = 500 \text{ fs}$, in agreement with earlier results.¹²⁹ The resulting decays of the anisotropy are shown in Fig. 7.2.

7.4.2 DISCUSSION OF THE MODEL

For very small delays ($t < 0.2 \text{ ps}$), the anisotropy decays more slowly than at larger delays, both in the calculations and the experiment. This is simply due to the fact that for these small delays, the creation of ‘new anisotropy’ by the pump pulse compensates the decay of anisotropy due to reorientation. In addition, it can be expected that during the temporal overlap between pump and probe pulses around $t = 0 \text{ ps}$, coherent coupling effects cause a small additional contribution to the anisotropy signal. Although there appears to be no coherent peak in the anisotropy, we did not draw definite conclusions about the reorientation from the data around zero delay.

At delays $< 1.5 \text{ ps}$, the anisotropy decay depends strongly on frequency. At 3500 cm^{-1} , most excited molecules will initially be in the fast-reorienting part of the spectrum and thus cause a relatively high anisotropy decay rate. At 3400 cm^{-1} , the initial decay rate is only

[†]To obtain an activation energy in J/mol , replace the numbers 600 and 1.81 by 7176 and 21.6, respectively

TABLE 7.1. Reorientation times after equilibration of the transient spectrum for the $\nu = 0$ and $\nu = 1$ vibrational states, calculated from the model. The values for $\tau_{r,\text{eq}}(\nu = 0)$ correspond to the reorientation times of water molecules in the absence of excitation by laser pulses.

T (K)	$\tau_{r,\text{eq}}(\nu = 0)$ (ps)	$\tau_{r,\text{eq}}(\nu = 1)$ (ps)
298	2.59	4.16
320	1.98	3.04
341	1.59	2.36
351	1.45	2.12
361	1.32	1.90

slightly faster than the average decay rate that is effective at larger delays (i.e. $t > 1.5$ ps). At these larger delays, the absolute value of the anisotropy is systematically lower at the high-frequency. However, the anisotropy decay rate does not depend on the frequency at these larger delay times (See §7.6.3 for the proof). This final decay rate depends on the spectral relaxation constant, the fraction of molecules with a large reorientation rate, and the maximum value of the reorientation rate at the high-frequency side of the spectrum (which increases with temperature). This final decay of the anisotropy is determined by both the anisotropy decay of the $\nu = 0$ state and that of the $\nu = 1$ state. The fraction of fast-reorienting molecules in the $\nu = 1$ state [the b_{\pm} components in Eqs. (7.8)] is smaller than the fraction of fast-reorienting molecules in the $\nu = 0$ state (the a_{\pm} components), due to the Stokes redshift in the $\nu = 1$ spectrum. This results in slightly different anisotropy decay rates for these two contributions to the anisotropy signal.

To summarize, there are three time constants that contribute to the anisotropy decay at a given frequency and temperature. The first time constant is the inverse of the reorientation rate at the excitation frequency; it mainly affects the decay at smaller delays. The value for this time constant can be read from Fig. 7.3. The second and the third time constants $\tau_{r,\text{eq}}(\nu = 0)$ and $\tau_{r,\text{eq}}(\nu = 1)$, that determine the decay at larger delays, are the reorientation time constants for the $\nu = 0$ and $\nu = 1$ states, respectively, after equilibration of the shape of the transient spectrum. By calculating the a and b contributions in Eq. (7.8) separately, we found the time constants for these slow processes as shown in Table 7.1. From Fig. 7.3, it is clear that only OH groups with a weak hydrogen bond are able to change orientation. This implies that a molecule with a low OH frequency and a strong hydrogen bond can only change orientation if the hydrogen bond is temporarily stretched, which corresponds to spectral diffusion to higher frequencies. In other words, only spectral diffusion enables low-frequency molecules to change their orientation.

In our model, we have used the 500 fs time constant for spectral relaxation from Ref. 129. However, it is possible to describe our data with the 700 fs time constant measured by Gale et al.³³ In that case, we find a slightly different activation energy, resulting in a reorientation rate curve in Fig. 7.3 that is shifted towards lower frequencies by less than 10 cm^{-1} . This shows that the model is not extremely sensitive to the spectral relaxation time constant.

Although our model can account well for both the frequency and the temperature dependence of the anisotropy decay, some refinements of the model are still possible. First, it is known that the OH stretch absorbance line shape changes with temperature.²⁸

In principle, this could be accounted for by modifying the spectral diffusion operators in Eqs. (7.10). Second, we assume that there is a single, well-defined, activation energy at a given OH stretch frequency. However, this activation energy may very well depend on the strength of the other hydrogen bonds to other neighboring water molecules. Therefore, it would be more correct to assume a distribution of activation energies (and a resulting distribution of reorientation rates) at each frequency. Finally, in our model we explicitly account for the fact that the reorientation of the water molecules is enabled by the spectral diffusion. However, we do not take into account that in turn the spectral diffusion may be affected by the reorientation. When an OH group changes its orientation, it is likely that the length of its hydrogen bond will change simultaneously. In other words, reorientation by itself contributes to spectral diffusion. In principle, the model could be refined by assuming that the spectral diffusion time constant has a frequency-dependence that is linked to the reorientation time constant, e.g. $1/\tau_c(\omega) = 1/\tau_{\min} + K/\tau_r(\omega)$, where τ_{\min} and K are to be determined from our data. However, this refinement will have little effect, since at lower frequencies, the reorientation takes place on a much slower time scale than the spectral diffusion, whereas at high frequencies, the hydrogen-bond length is large and any rotations will not strongly influence the frequency of an OH vibration. In addition, the spectral relaxation in water can be well described as a Gauss-Markov process, as was shown by Woutersen and Bakker¹²⁹ and Gale et al.³³ We will discuss this in more detail in Chapter 8. This means that there is no evidence for a significant frequency dependence of spectral diffusion.

7.4.3 COMPARISON WITH OTHER STUDIES

In a previous publication,¹³² time constants τ_r of 0.7 and 13 ps were obtained with the same method as presented here. The 0.7 ps time constant corresponds to a spectral average of the initial fast process at the high-frequency side of the spectrum (approximately 1 ps), while the 13 ps time constant corresponds to the slower time constants $\tau_{r,\text{eq}}(\nu = 0) = 2.6$ ps and $\tau_{r,\text{eq}}(\nu = 1) = 4.2$ ps that result after equilibration of the transient spectral line shapes. The time constants differ from the earlier results due to the improved signal-to-noise ratio.

The reorientational dynamics of liquid water have also been investigated with molecular dynamics simulations. These calculations yield time constants that depend strongly on the simulation method. In *ab initio* density functional theory calculations, values for τ_2 have been reported that range from 1.2 to 9 ps.¹¹³ In classical molecular dynamics studies, time constants between 0.7 and 1.7 ps were found.^{15,122} In one study, a bi-exponential decay of $C_2(t)$ was found with 1.0 and 13 ps time constants.¹³⁷

According to NMR experiments,¹⁰⁵ the reorientation time τ_r of HDO in D₂O decreases from 2.7 ps at 298 K to 0.81 ps at 350 K.[♮] These values are slightly smaller than those for $\tau_{r,\text{eq}}(\nu = 0)$ in Table 7.1. In both H₂O and D₂O, the Debye time τ_1 varies from approximately 8 ps at 300 K to 3 ps at 360 K, with a small isotopic effect.^{57,103,104} These values correspond to $\tau_r = 2.7$ and 1.0 ps, respectively. Interestingly, the reorientation time $\tau_{r,\text{eq}}(\nu = 0)$ in Table 7.1 satisfies Eq. (7.3) with $E_{\text{act}} = 1147 \text{ cm}^{-1}$ (13.7 kJ/mol) and $\tau_{r,0} = 55$ fs. Hence, the model discussed in this chapter does not show the behavior of Eq. (7.4), which predicts a activation energy that decreases with increasing temperature. Two things must be noted. (i) The present model does not take into account that the OH

[♮]Isotopic correction factors from Refs. 68 and 50 were applied to obtain numbers for HDO in D₂O.

absorption band of HDO:D₂O shifts towards higher frequencies with increasing temperature due to a weakening of the hydrogen bonds.²⁸ In the present context, the OH band in Fig. 7.3 shifts to the right, which corresponds to an overall lower rotational activation energy. (ii) In the temperature range of the present study, the critical temperature equation, Eq. (7.4), differs by less than a fraction 0.02 from a pure Arrhenius-like behavior [Eq. (7.3)]. Hence, the time constants found in NMR and dielectric relaxation measurements are in agreement with the value of $\tau_{r,\text{eq}}(\nu = 0)$ that we observe after the transient spectrum has equilibrated. This $\tau_{r,\text{eq}}(\nu = 0)$ represents an effective reorientation time scale that forms an average over *all* water molecules. An important advantage of the femtosecond nonlinear spectroscopic method employed in this work is that the reorientational dynamics of a *subensemble* of the water molecules can be investigated. This enables a determination of the mechanism behind the effective reorientation time of liquid water as observed in NMR and dielectric relaxation experiments. This work shows that the effective reorientation rate in liquid water is governed by the fraction of water molecules for which reorientation is not hindered by the OH ··· O hydrogen bond, the rate of this unhindered reorientation, and the rate at which the strength of the hydrogen bonds is stochastically modulated.

7.5 CONCLUSIONS

We have measured the orientational relaxation of HDO molecules dissolved in liquid D₂O by creating an anisotropic population of excited OH stretch vibrations with femtosecond mid-infrared pulses and by subsequently measuring the decay of this anisotropy. The decay of the anisotropy is nonexponential and takes place on a typical time scale of 1 ps. At the blue side of the inhomogeneously broadened OH stretch vibration absorption band (3500 cm⁻¹), the anisotropy decays faster than at the center of the absorption band (3400 cm⁻¹).

We find that the frequency and temperature dependence of the anisotropy decay can be well described with a model in which the reorientation is an activated process. The activation energy for reorientation decreases linearly with increasing hydrogen-bond length. This yields a reorientation rate as a function of frequency that increases steeply. By varying the temperature, we find that the maximum reorientation rate at the high-frequency side of the absorption band increases from 2.8 ps⁻¹ at 298 K to 4.5 ps⁻¹ at 360 K.

The model also includes the effects of spectral diffusion that results from the stochastic modulation of the hydrogen-bond length. It is found that the reorientation of strongly hydrogen-bonded water molecules is enabled by the weakening of the hydrogen bond.

7.6 APPENDIX: MATHEMATICAL DETAILS

7.6.1 ROTATIONAL DIFFUSION

Oriental diffusion describes the time dependence of the orientation vectors \mathbf{e} of an ensemble of molecules. The vector \mathbf{e} is fixed in the molecular frame and has a time-dependent angular distribution in the laboratory frame $\psi(\theta, \phi, t)$, which represents the

number of particles in a solid angle $d\Omega = \sin\theta d\theta d\phi$. Its time evolution is described by

$$\frac{\partial}{\partial t}\psi(\theta, \phi, t) = D_r \mathcal{R}\psi(\theta, \phi, t), \quad (7.12)$$

where D_r is the rotational diffusion constant and \mathcal{R} is the Laplace operator in polar coordinates,

$$\mathcal{R} = \frac{1}{\sin\theta} \left(\cos\theta \frac{\partial}{\partial\theta} + \sin\theta \frac{\partial^2}{\partial\theta^2} + \frac{1}{\sin^2\theta} \frac{\partial^2}{\partial\phi^2} \right). \quad (7.13)$$

We can construct the solutions of Eq. (7.12) by noting that \mathcal{R} has the spherical harmonics $Y_{lm}(\theta, \phi)$ as eigenfunctions,⁵⁴ that have eigenvalues $-l(l+1)$ with $l = 0, 1, 2, \dots$. The generic solution of Eq. (7.12) is therefore an expansion in eigenfunctions,

$$\psi(\theta, \phi, t) = \sum_{l \geq 0} \sum_{m=-l}^l c_{lm} Y_{lm}(\theta, \phi) e^{-D_r l(l+1)t}, \quad (7.14)$$

where c_{lm} are arbitrary constants. In experimental geometries, there is usually no ϕ dependence, which means that $m = 0$ and

$$\psi(\theta, \phi, t) = \sum_{l \geq 0} c_l P_l(\cos\theta) e^{-D_r l(l+1)t}, \quad (7.15)$$

where $P_l(x)$ are Legendre polynomials [i.e., $P_0(x) = 1$, $P_1(x) = x$, $P_2(x) = (3x^2 - 1)/2$]. It can be shown that the rotational anisotropy $A = \langle P_2(\cos\theta) \rangle$, with $\theta = 0$ corresponding to the pump pulse polarization. Due to the orthogonality of the Legendre polynomials, A decays with a time constant $\tau_r = \tau_2 = 1/6D_r$. The subscript 2 indicates that $l = 2$. The time constants obtained in NMR measurements also refer to τ_2 . However, the Debye time obtained in dielectric relaxation measurements corresponds to $\tau_1 = 3\tau_2$.

7.6.2 SPECTRAL DIFFUSION

The operators \mathcal{D}_v originate from the Brownian oscillator model in §5.4, that describes diffusion in a harmonic potential and the resulting spectral diffusion. The equations in §5.4 are a limiting case of the original description in a more general but highly complicated formalism.⁸⁸ For the purposes in this chapter and Chapter 8, it is more convenient to treat the Brownian oscillator as a diffusion problem.

A time-dependent distribution $n(R, t)$ of diffusing particles in a potential $W(R)$ satisfies the diffusion equation⁶³

$$\frac{\partial n}{\partial t} = D_R \left(\frac{\partial^2}{\partial R^2} + \beta \frac{dW}{dR} \frac{\partial}{\partial R} + \beta \frac{d^2 W}{dR^2} \right) n, \quad (7.16)$$

where $\beta = 1/k_B T$ and D_R is the diffusion constant. If we assume a harmonic potential $W_v(R)$ for vibrational state v , we can write

$$D_R = \frac{\tilde{\Delta}^2}{\tau_c}, \quad (7.17)$$

where $\tilde{\Delta}$ is the RMS deviation of R from its central value R_0 , or

$$W_0(R_0 \pm \tilde{\Delta}) - W_0(R_0) = k_B T/2. \quad (7.18)$$

With the potentials for the $v = 0$ and $v = 1$ states in Fig. 5.3, we can use Eq. (7.16) to obtain the diffusion equation

$$\frac{\partial a}{\partial t} = \mathcal{D}_0 a, \quad (7.19)$$

which is in terms of the spectral response $a(\omega, t)$ of the bleaching contribution of the $v = 0$ state (i.e. the B_{01} contribution in Eq. (5.4) before convolution with the spectrum of the probe pulses), where

$$\mathcal{D}_0 = \frac{1}{\tau_c} \left(\Delta_d^2 \frac{\partial^2}{\partial \omega^2} + (\omega - \omega_B) \frac{\partial}{\partial \omega} + 1 \right). \quad (7.20)$$

Here, Δ_d is the standard deviation of the Gaussian linear absorption spectrum, centered at $\omega = \omega_B$, that results from the parabolic potentials $V_v(R)$. The operator \mathcal{D}_1 for the bleaching contribution $b(\omega, t)$ of the $v = 1$ state (similar to B_{10} in Eq. (5.4)) is very similar, i.e.

$$\mathcal{D}_1 = \frac{1}{\tau_c} \left(\Delta_d^2 \frac{\partial^2}{\partial \omega^2} + (\omega - \omega_B + \delta\omega_{\text{sto}}) \frac{\partial}{\partial \omega} + 1 \right), \quad (7.21)$$

where $\delta\omega_{\text{sto}}$ is the Stokes shift.

7.6.3 ANISOTROPY DECAY AT LARGE DELAYS

It is relatively easy to see that the anisotropy A decays exponentially at large delays. Similar to the rotational-diffusion operator in §7.6.1, the spectral-diffusion operator \mathcal{D}_0 has eigenfunctions $\phi_j(\omega)$ with eigenvalues λ_j . All eigenvalues are negative, except for $\lambda_0 = 0$, which corresponds to the distribution in thermal equilibrium. Thus, the isotropic signal [see Eq. (7.10c)], for delays t much larger than the pulse duration, has the general form

$$a_+(\omega, t) = c_0 \phi_0(\omega) + \sum_{j \geq 1} c_j \phi_j e^{\lambda_j t}. \quad (7.22)$$

The anisotropic signal a_- has a different set of eigenfunctions $\chi_j(\omega)$ with eigenvalues μ_j , which are all negative due to the loss term in Eq. (7.10a); its expansion is

$$a_-(\omega, t) = \sum_{j \geq 1} d_j \chi_j e^{\mu_j t}. \quad (7.23)$$

If we define k as the index for the largest eigenvalue μ_k , the rotational anisotropy $A_0 = a_-/a_+$ for the ground state contributions will approach

$$A_0(t) \rightarrow d_k e^{\mu_k t} / c_0 \quad (7.24)$$

asymptotically for $t \gg \tau_c$. The coefficients d_k and c_0 depend on the initial distributions of a_{\pm} (that depend on the pump pulse spectrum), but the decay rate $\mu_k = -1/\tau_{r,\text{eq}}(v = 0)$ is independent on these initial distributions. Similar arguments apply to the overall anisotropy A in Eq. (7.7).

7.6.4 NUMERICAL IMPLEMENTATION

Calculating the time-evolution of the diffusion equation (7.16) can be done with a forward time centered space (FTCS) algorithm.¹⁰⁰ If a function $f(R)$ (representing either V or n) is discretized as f_i with steps δR , then derivatives to R can be approximated as

$$f'_i \equiv \frac{\partial f}{\partial R} \approx \frac{1}{2\delta R}(f_{i+1} - f_{i-1}), \quad (7.25)$$

$$f''_i \equiv \frac{\partial^2 f}{\partial R^2} \approx \frac{1}{\delta R^2}(f_{i+1} + f_{i-1} - 2f_i). \quad (7.26)$$

For numerically stable behavior, it is usually sufficient to set

$$\delta t = (1 - \epsilon)\delta R^2/2D_R, \quad (7.27)$$

with $\epsilon \approx 0.1$. The diffusion equations for the $v = 0$ and $v = 1$ vibrational states should be solved independently from each other yielding solutions $n_0(R)$ and $n_1(R)$. The spectral response, including the induced absorption due to the $v = 1 \rightarrow 2$ transition, is

$$a(\omega) = [n_0(R_{01}(\omega)) + n_1(R_{01}(\omega))] \frac{dR_{01}}{d\omega} - \sigma n_1(R_{12}(\omega)) \frac{dR_{12}}{d\omega} \quad (7.28)$$

where σ is the relative cross-section of the $v = 1 \rightarrow 2$ transition and $R_{jk}(\omega)$ are mappings of the $v = j \rightarrow k$ transition frequency to R , i.e. the inverse functions of

$$\omega_{jk}(R) = V_k(R) - V_j(R), \quad (7.29)$$

where we assume $\hbar = 1$. If i has a finite range $0 \cdots N - 1$, boundary conditions can be implemented by assuming $n_0 = n_{N-1} = 0$; after each timestep, add the new value n_0 to n_1 and add the new value n_{N-1} to n_{N-2} .

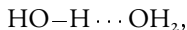
Equation (7.20) is useful if harmonic potentials can be assumed and no contribution of the $v = 1 \rightarrow 2$ transition is used. The former is the case in this chapter. To conserve the number of particles upon numerical integration, the factor $(\omega - \omega_B)$ in Eq. (7.20) should be written as the numerical approximation of $d[(\omega - \omega_B)^2/2]/d\omega$ and not as $\omega - \omega_B$.

8 SPECTRAL DIFFUSION AND MECHANISM FOR AUTODISSOCIATION

We study the spectral response of the transition between the first and the second excited state of the O–H stretch vibration of HDO dissolved in liquid D₂O with two-color femtosecond mid-infrared spectroscopy. The spectral response of this transition differs strongly from the fundamental absorption spectrum of the O–H stretch vibration. In addition, excitation of the O–H stretch vibration is observed to lead to a change of the hydrogen-bond dynamics of liquid water. We show that both these observations can be described with a refined quantum-mechanical version of the Lippincott-Schroeder model for hydrogen-bonded OH···O systems. An important implication is that excitation of the $\nu = 2$ state of the OH stretch vibration can initiate the autodissociation reaction $2\text{H}_2\text{O} \rightarrow \text{H}_3\text{O}^+ + \text{OH}^-$.

8.1 INTRODUCTION

In the previous chapters, we saw that the hydrogen bonds in liquid water,



or the equivalent in the isotopically labeled HDO:D₂O solution, are not static, but undergo fluctuations around their equilibrium length on a time scale of about one picosecond. Since separating two hydrogen-bonded water molecules requires energy, these length fluctuations are bounded by the available thermal energy at a given temperature. We have modeled these dynamics by assuming that the length fluctuations can be interpreted as diffusion of a particle in a parabolic potential, that represents the energy of the OH···O system $W(R)$ as a function of the hydrogen-bond length R , defined as the O···O distance (about 2.85 Å in water). These potentials $W_\nu(R)$ for vibrational states $\nu = 0, 1, 2$ were shown schematically in Fig. 5.3, with the roles of D and H swapped. The assumption of a parabolic, or harmonic, potential is justified, since the typical thermal energy is $k_B T \approx 207 \text{ cm}^{-1}$, while the dissociation energy of the hydrogen bond is around 1900 cm^{-1} (23 kJ/mol). As a probe for the hydrogen-bond length, we use the OH stretch vibration in an HDO molecule, whose frequency depends parametrically on R . The fact that the OH stretch mode has discrete ground and excited states implies that it must be described quantum-mechanically. In this description, each vibrational state corresponds to a solution of the Schrödinger equation that describes the probability amplitude of the proton (the nucleus of the H atom) as a function of the proton coordinate r (defined as the O–H distance), with a potential energy $V(r, R)$. For $R \rightarrow \infty$, this potential has a shape similar to the curve shown in Fig. 2.6, for which a harmonic potential with a small anharmonic correction is a good approximation for the lowest few vibrational states. However, the potential $V(r, R)$ is obviously different for the typical value $R \approx 2.8 \text{ Å}$: it must go to infinity

for $r \rightarrow R$. Such a strong anharmonicity must affect even the lowest vibrational states of the OH stretch vibration. We will relate this anharmonicity to the shape of the transient spectrum of vibrationally excited HDO molecules and refine the description of spectral diffusion (Ref. 129 and §5.4). Finally, we will discuss the implications of the anharmonicity of the OH stretch mode on the autodissociation reaction $2\text{H}_2\text{O} \rightarrow \text{H}_3\text{O}^+ + \text{OH}^-$.

8.2 EXPERIMENT

The experiments were pump-probe measurements where a femtosecond infrared laser pulse excited the $\nu = 0 \rightarrow 1$ transition of the OH stretch vibration of HDO molecules dissolved in D_2O . The sample consists of a $200 \mu\text{m}$ -thick layer of HDO dissolved in D_2O with a transmittance of approximately 5% at 3400 cm^{-1} , the center of the $\nu = 0 \rightarrow 1$ absorption band. The sample was at room temperature and at a fixed position in the laser beam focus (see §2.8 for an estimate of the accumulated heat) Apart from the sample, the setup is identical to the setup described in §6.2, which yielded the absorbance change $\Delta\alpha(\omega_{\text{pr}}, t)$ for a fixed pump frequency of 3420 cm^{-1} and a range of probe frequencies ω_{pr} and pump-probe delays t .

8.3 THE EQUILIBRATED TRANSIENT SPECTRUM

We saw in Chapter 5 that the spectral correlation time for the OD stretch vibration is 400 fs , which is a measure for the solvent relaxation time. For the OH stretch vibration of HDO in D_2O , other studies^{33,36,129} showed spectral relaxation times of 0.5 and 0.7 ps , which means that after 1 – 2 ps , the distributions of the hydrogen-bond lengths for populations in the $\nu = 0$ and $\nu = 1$ states will have nearly equilibrated within the $W_0(R)$ and $W_1(R)$ potentials, respectively. At these larger delays, the transient spectrum decreases in amplitude due to vibrational relaxation, but does not change its shape significantly. Figure 8.1 presents transient absorption spectra of the OH stretch vibration delays of 0.5 , 1 , and 2 ps for a pump spectrum centered at 3420 cm^{-1} .

For probe frequencies $>3300 \text{ cm}^{-1}$, the signal is positive and results from the bleaching of the $\nu = 0 \rightarrow 1$ transition. For frequencies $<3300 \text{ cm}^{-1}$, the signal is negative and results from the induced $\nu = 1 \rightarrow 2$ absorption. For both pump frequencies, the width of the bleaching band increases with the pump-probe delay, which indicates a spectral hole that broadens due to spectral relaxation. Because of the relation between the hydrogen-bond length R and the vibrational frequency ω (§1.1), we see here directly how the initial narrow distribution of hydrogen-bond lengths that was selected by the spectrum of the pump pulse broadens in time due to the rapid length fluctuations.

At larger delays t , the bleaching has the nearly-Gaussian shape of the linear absorption spectrum in Fig. 1.3. In contrast, the spectral shape of the $\nu = 1 \rightarrow 2$ absorption is much broader and much steeper on the high-frequency side than on the low-frequency side. The steep high-frequency side can partly be explained from the cancellation of the bleaching and the induced absorption in this frequency region. However, even after correction for this effect, the resulting induced absorption remains strongly asymmetric. The asymmetry and the width of the $\nu = 1 \rightarrow 2$ band are surprising, because the anharmonicity at the

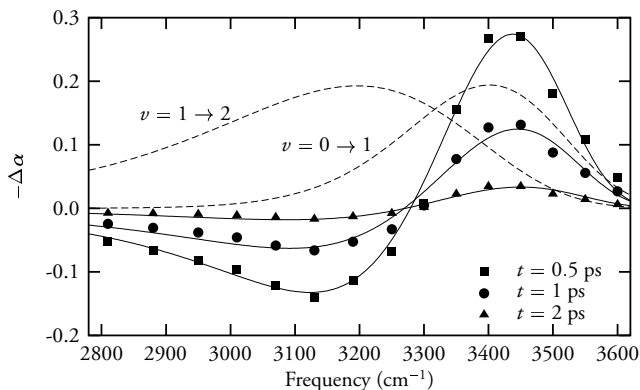


FIGURE 8.1. Transient spectra of HDO dissolved in D_2O after excitation of the OH stretch mode at 3420 cm^{-1} , for three pump-probe delays t . The solid curves represent transient spectra that are calculated with the modified quantum-mechanical Lippincott-Schroeder (QLS) model (§8.3.1). The dashed curves represent calculated absorption spectra for the $\nu = 0 \rightarrow 1$ and $\nu = 1 \rightarrow 2$ transitions in thermal equilibrium.

lowest vibrational levels is normally small for strong chemical bonds,⁹⁵ such as the CO stretch,^{1,49,94} the CH stretch,¹²⁰ and even the weakly hydrogen-bonded OD stretch.⁵

8.3.1 QUANTUM-MECHANICAL LIPPINCOTT-SCHROEDER MODEL

The assumption of harmonic hydrogen-bond potentials $W(R)$, mentioned in §8.1, results in a Gaussian-shaped linear absorption spectrum, in quite good agreement with the empirical linear OH-stretch spectrum of HDO in D_2O (Fig. 1.3). A correlation-function approach^{8,9} yields similar spectra. However, from Fig. 8.1, it is clear that the $\nu = 1 \rightarrow 2$ absorption spectrum has a strongly non-Gaussian shape that cannot be accounted for by the Brownian oscillator model. The description of the $\nu = 1 \rightarrow 2$ absorption spectrum requires a more advanced model that, in contrast to the Brownian oscillator model, includes strong anharmonicities for the potentials of the OH stretch and the $OH \cdots O$ hydrogen-bond coordinates.

As a starting point for a description of the anharmonic coupling between the OH stretch vibration and the hydrogen-bond mode, we use the so-called Lippincott-Schroeder (LS) model.⁷³ This model is based on the empirical correlation between the frequency of the OH stretch vibration and the length of the $OH \cdots O$ hydrogen bond R (§1.1). This correlation is surprisingly similar for systems that differ in the strength of local electric fields and in the presence of other interaction than the hydrogen bond. This universal behavior can be explained from the fact that most interactions affect the OH stretch mode of a hydrogen-bonded system mainly by changing the length of the polarizable $OH \cdots O$ hydrogen bond. These interactions thus have very little effect on the relation between the OH stretch vibration and the $OH \cdots O$ hydrogen bond, and mainly express themselves in a change of the length of this bond. Hence, the interactions between the OH stretch mode of the HDO molecule and its surroundings is well approximated with a single well-defined relation between the vibrational potential $V(r, R)$ and the hydrogen-bond length

R . Such a relation is provided by the LS model.

We write the potential energy $V(r, R) = V_I(r, R) + V_{II}(R)$ as the sum of two terms. The first term is the original LS potential,⁷³

$$V_I(r, R) = D_{Ia}[1 - e^{-n_{Ia}(r-r_o)^2/2r}] + D_{Ib}[1 - e^{-n_{Ib}(R-r-r_o)^2/2(R-r)}]. \quad (8.1)$$

The parameters of $V_I(r, R)$ follow from various known parameters. The energy $D_{Ia} = 38750 \text{ cm}^{-1}$ is the binding energy of the OH bond of water (463 kJ/mol), $n_{Ia} = 9.8 \text{ \AA}^{-1}$ defines the frequency of the OH stretch vibration, $r_o = 0.97 \text{ \AA}$ is the OH bond length in the gas phase (absence of a hydrogen bond), and D_{Ib} is determined by the empirical relations between r , R , and the OH stretch frequency. An excellent description of these relations is obtained with $D_{Ia}/D_{Ib} \approx 1.5$.⁷³ Here we use $D_{Ib} = 25000 \text{ cm}^{-1}$. The validity of the LS model has been supported by a quantum-mechanical calculation⁷⁶ of $V_I(r, R)$ for the H_5O_2^- ion, that showed behavior similar to the Lippincott-Schroeder potential.

In the past, the LS model has mostly been used classically. Only more recently, the model was used quantum-mechanically to calculate the vibrational lifetime of the OH stretch vibration.¹⁴ In the original treatment, the frequency of the OH stretch vibration was calculated from a harmonic approximation around the minimum of V_I . Clearly, this procedure cannot account for the anharmonicity that causes the lower frequency of the $\nu = 1 \rightarrow 2$ transition compared to the $\nu = 0 \rightarrow 1$ transition. Therefore, we perform a quantum-mechanical calculation by solving the one-dimensional Schrödinger equation for the OH coordinate r in the LS potential $V_I(r, R)$. We will refer to this quantum-mechanical LS model as the QLS model.

We use an adiabatic approximation with R as a parameter, which implies that the first and second derivative of the vibrational wavefunctions of the OH stretch vibration with respect to R are neglected. This type of adiabatic approach is commonly used in describing the coupling between a high-frequency OH stretch vibration and a low-frequency OH \cdots O hydrogen bond.^{7,82} We used the Numerov method¹⁹ to calculate the vibrational eigenfunctions $\phi_\nu(r, R)$ as a function of R for all states ν . The eigenfunctions have energies $E_\nu(R)$. The adiabatic approximation will be valid if the motion in R is much slower than that in r . The corresponding characteristic frequencies of 200 cm^{-1} (hydrogen-bond vibration)⁴⁷ and 3400 cm^{-1} (OH stretch) are sufficiently different to justify this approximation. This approximation implies that eigenstates of the entire O–H \cdots O system are product states $\phi_\nu(r, R)\psi_{\nu'}(R)$, where ν' is the (possibly high) hydrogen-bond quantum number and ν is the OH stretch quantum number (0, 1, or 2). Without the adiabatic approximation, these product states would not be pure eigenstates, with the result that an excited OH stretch state ($\nu = 1$) decays to its ground state ($\nu = 0$), during which the energy is transferred to the hydrogen-bond mode. In other words, the adiabatic approach does not describe vibrational relaxation, which was discussed in Chapter 4 (see especially Fig. 4.5).

In V_I , the original LS potential, R was treated as an externally imposed parameter, i.e. the distance two molecules happened to have in a solution. The second potential term, $V_{II}(R)$, is necessary to describe the electrostatic attraction of two water molecules at large distances and their repulsion at short distances. Such an attraction can usually be described by the Morse potential

$$V_{II}(R) = D_{II}[1 - e^{-n_{II}(R-R_o)}]^2. \quad (8.2)$$

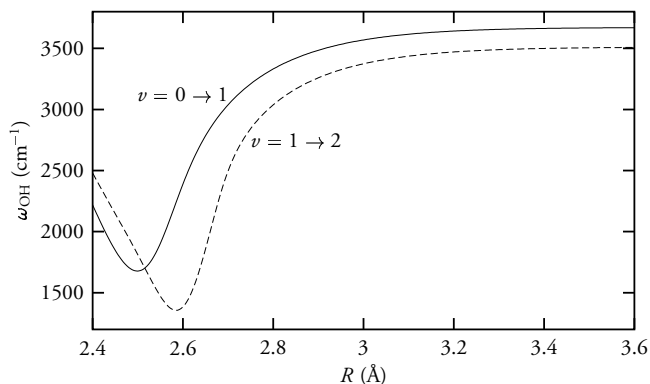


FIGURE 8.2. Frequencies of the $\nu = 0 \rightarrow 1$ and the $\nu = 1 \rightarrow 2$ transitions as a function of the oxygen-oxygen distance R of the $\text{OH} \cdots \text{O}$ hydrogen bond, calculated with the QLS model (§8.3.1).

However, $V_{\text{II}}(R)$ is not yet equivalent to the hydrogen-bond potential $W_v(R)$, because the latter involves the energy $E_v(R)$ of the OH stretch vibration state ν as well. Thus, $W_v(R) = E_v(R) + V_{\text{II}}(R)$. The yet unknown parameters in the potentials V_{I} and V_{II} are now n_{lb} [Eq. (8.1)], D_{II} , n_{II} , and R_{O} . Since the potential $W_0(R)$ for the vibrational ground state must describe the empirical values²⁵ for the hydrogen-bond dissociation energy (1900 cm^{-1}), the equilibrium length $R_{\text{eq},0} = 2.85 \text{ \AA}$, and the hydrogen-bond stretch frequency of $\sim 2000 \text{ cm}^{-1}$ (Ref. 47), there is effectively only one independent parameter left that must be determined from a fit to the transient spectra in Fig. 8.1 (details follow in §8.3.2). We find: $n_{\text{lb}} = 16.5(1.0) \text{ \AA}^{-1}$, $D_{\text{II}} = 2000 \text{ cm}^{-1}$, $n_{\text{II}} = 2.9(2) \text{ \AA}^{-1}$, and $R_{\text{O}} = 2.88 \text{ cm}^{-1}$. We note that the values for D_{II} and R_{O} affect the transient spectra only weakly. However, the values of n_{lb} and n_{II} have a strong effect on the transient spectra. The asymmetry of the $\nu = 0 \rightarrow 1$ and $\nu = 1 \rightarrow 2$ absorption bands is strongly determined by n_{lb} , and the width of these bands depends on n_{II} .

The transition $\nu = i \rightarrow j$ has an associated frequency $\omega_{ij}(R) = [W_j(R) - W_i(R)]/\hbar$ as a function of the oxygen-oxygen distance R . Figure 8.2 shows the calculated frequencies $\omega_{01}(R)$ and $\omega_{12}(R)$. The calculated $\omega_{01}(R)$ shows a strongly nonlinear dependence on R , in good agreement with experimental observations.^{85,92} Figure 8.3 shows the hydrogen-bond potentials $W_0(R)$, $W_1(R)$ and $W_2(R)$ (corresponding to $\nu = 0, 1, 2$ states), together with the V_{I} potential.

The origin of the large width and asymmetric shape of the $\nu = 1 \rightarrow 2$ absorption spectrum is the change of the distribution in R upon excitation of the OH stretch vibration. We find that the equilibrium lengths $R_{\text{eq},\nu}$ of the hydrogen bond decreases with increasing quantum number ν of the OH stretch mode: $R_{\text{eq},0} = 2.85 \text{ \AA}$, $R_{\text{eq},1} = 2.80 \text{ \AA}$, and $R_{\text{eq},2} = 2.70 \text{ \AA}$. The derivatives $d\omega_{01}/dR$ and $d\omega_{12}/dR$ of the $\nu = 0 \rightarrow 1$ and $\nu = 1 \rightarrow 2$ transitions are largest for smaller R , as can be seen from Fig. 8.2. Hence, a given distribution of R results in a $\nu = 1 \rightarrow 2$ spectrum that is broader than the $\nu = 0 \rightarrow 1$ spectrum. For R in the range 2.6–2.9 \AA , which corresponds to the thermal distribution in the $\nu = 1$ state, the derivative $d\omega_{12}/dR$ is very large. We can understand the latter from the shape of the r -dependent potential-energy contribution $V_{\text{I}}(r, R)$. Figure 8.4 shows the poten-

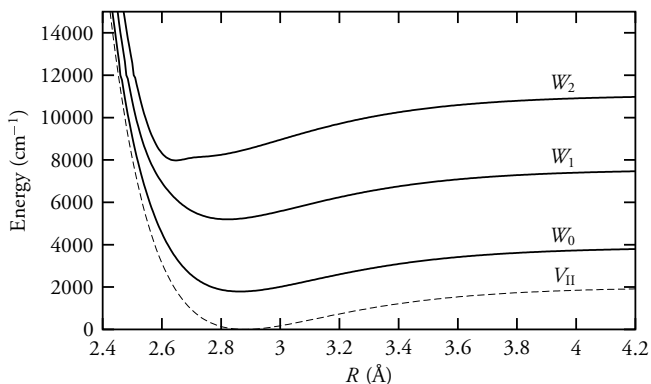


FIGURE 8.3. Hydrogen-bond potentials $W_\nu(R)$ for the $\nu = 0, 1, 2$ states of the OH stretch mode, together with the Morse potential $V_{II}(R)$. These functions are obtained by fitting the parameters of the QLS model (§8.3.1) to the transient spectra in Fig. 8.1.

tial $V_1(r, R)$ as a function of the OH bond length for a few values of the oxygen-oxygen distance R .

At oxygen-oxygen distances R below 2.7 \AA , the potential $V_1(r, R)$ becomes very broad at the $\nu = 2$ energy level. This broadening of the potential leads to a strongly delocalized $\nu = 2$ state and a decrease of E_2 . Hence, in this region of R , a small variation in R leads to a large change of E_2 . As a result, the transition frequency of the $\nu = 1 \rightarrow 2$ transition varies strongly over the thermal distribution of R (with a width of $\approx 0.36 \text{ \AA}$ at 300 K), which leads to a strong broadening of the $\nu = 1 \rightarrow 2$ transition. The delocalization of the $\nu = 2$ state for $R \leq 2.7 \text{ \AA}$ also affects the shape of the $\nu = 0 \rightarrow 2$ overtone transition of the OH stretch vibration. This overtone spectrum has been extensively studied for different isotopes of ice^{61,107} and water.⁷¹ For water, the $\nu = 0 \rightarrow 2$ overtone transition is indeed strongly asymmetrically broadened to lower frequencies,⁷¹ similar to the $\nu = 1 \rightarrow 2$ transition in Fig. 8.1.

8.3.2 CALCULATION OF TRANSIENT SPECTRA

To calculate the transient spectra, we evaluated the potentials $W_\nu(R)$ numerically for R in the range $2.2\text{--}3.8 \text{ \AA}$ with a step size $\delta R = 0.004 \text{ \AA}$. For every value of R , we calculated the transition dipole matrix elements

$$\mu_{01}(R) = \langle \phi_1(r, R) | r | \phi_0(r, R) \rangle_r, \quad (8.3)$$

$$\mu_{12}(R) = \langle \phi_2(r, R) | r | \phi_1(r, R) \rangle_r, \quad (8.4)$$

that represent the probabilities for the $\nu = 0 \rightarrow 1$ and $\nu = 1 \rightarrow 2$ transitions at a given value of R . The subscript r indicates that the integration should be carried over r . We assume that at larger delays after the pump pulse, the population $\Delta n_1(R)$ of the $\nu = 1$ state and the population depletion $-\Delta n_0(R)$ are thermal distributions

$$\Delta n_0(R) = N_0 e^{-\beta W_0(R)}, \quad (8.5)$$

$$-\Delta n_1(R) = N_1 e^{-\beta W_1(R)}, \quad (8.6)$$

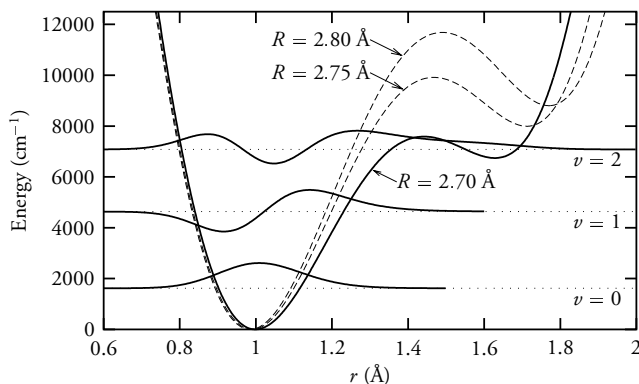


FIGURE 8.4. Vibrational potential V_1 for three different oxygen-oxygen distances R of the $\text{OH} \cdots \text{O}$ hydrogen bond as a function of the OH bond length r . Also shown are the vibrational wavefunctions of the $\nu = 0, 1, 2$ states for $R = 2.7 \text{ \AA}$.

where N_ν are normalization factors such that

$$\int \Delta n_0(R) dR = - \int \Delta n_1(R) dR = 1. \quad (8.7)$$

and $\beta = 1/k_B T$. If we denote the inverse function of $\omega_{ij}(R)$ by $R_{ij}(\omega)$, the frequency spectrum is given by

$$\begin{aligned} -\Delta \tilde{\alpha}(\omega) \propto & [\Delta n_0(R_{01}) + \Delta n_1(R_{01})] \cdot |\mu_{01}(R_{01})|^2 \cdot \frac{dR_{01}}{d\omega} \\ & + \Delta n_1(R_{12}) \cdot |\mu_{12}(R_{01})|^2 \cdot \frac{dR_{12}}{d\omega}. \end{aligned} \quad (8.8)$$

The derivatives of R_{ij} are necessary to transform the distribution $n_i(R_{ij})$ (particles per unit of R_{ij}) to the distribution $\Delta \tilde{\alpha}(\omega)$ (absorption per unit of ω). The above equation is in fact nothing more than a precise version of Eq. (5.4) and Eq. (7.28). To translate this frequency spectrum to the observed transient spectrum $\Delta \alpha(\omega)$ (Fig. 8.1), a convolution with the effective probe spectrum $F_{\text{pr}}(\omega')$ is necessary (see also §2.6):

$$\Delta \alpha(\omega) = \bar{\sigma} \int d\omega' \Delta \tilde{\alpha}(\omega - \omega') F_{\text{pr}}(\omega'), \quad (8.9)$$

where $\bar{\sigma}$ defines the amplitude of the bleaching [see also Eq. (1.6)] and $F_{\text{pr}}(\omega)$ is the convolution of the probe pulse spectrum and a homogeneous line shape with an FWHM of 90 cm^{-1} . We will discuss the homogeneous line shape in §8.4, where we also discuss the effect of the equilibration process on the transient spectrum.

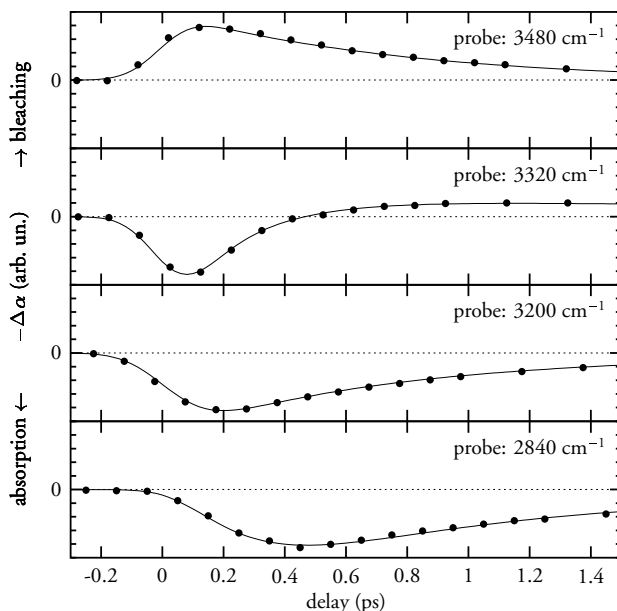


FIGURE 8.5. Pump-probe delayscans of HDO:D₂O after excitation of the OH stretch mode at 3560 cm⁻¹. The drawn lines result from the QLS model in combination with the spectral dynamics discussed in §8.4.1 and §8.4.2.

8.4 THE DYNAMICS OF THE TRANSIENT SPECTRA

8.4.1 SPECTRAL DIFFUSION

The transient spectra in Fig. 8.1, taken at pump-probe delays $t > 0.5$ ps, differ mainly in amplitude. For shorter delays, this is no longer true. Figure 8.5 shows pump-probe delayscans after excitation at 3560 cm⁻¹. Especially the data where the probe frequency was 2840 cm⁻¹ shows a response directly after excitation (delay $t = 0$) that is significantly slower than in the data where the probe frequency was 3320 cm⁻¹. This delayed response results from spectral dynamics.

Because of the strong overdamped behavior of the hydrogen bond (§4.5), we describe the hydrogen-bond dynamics as a classical diffusive process in the $W_0(R)$ and $W_1(R)$ hydrogen-bond potentials. In Chapters 5, 6, and 7, we approximated the hydrogen-bond potentials by harmonic potentials, for which the diffusive hydrogen-bond dynamics could be described analytically. However, in order to take the strong anharmonicity of the potentials $W_v(R)$ (Fig. 8.4) fully into account, a numerical calculation is necessary. In related previous microscopic semiclassical treatments, the dynamics on the potential-energy surfaces of the ground and excited state were calculated using molecular dynamics simulations.^{14,83,32} Here, we describe the dynamics of the hydrogen bonds as a diffusion process in a potential well $W_v(R)$. The populations $\Delta n_v(R)$ discussed in the previous section are created by a pump pulse. Directly after excitation ($t = 0$), the distributions of the

population changes are

$$\Delta n_1(R) = -\Delta n_0(R) = F_{\text{pu}}(\omega_{\text{or}}(R)) \cdot |\mu_{\text{or}}(R)|^2 \cdot \frac{d\omega_{\text{or}}}{dR}, \quad (8.10)$$

where $F_{\text{pu}}(\omega)$ is the pump-pulse spectrum, convolved with the homogeneous linewidth (§2.6) that has an FWHM of 90 cm^{-1} . This homogeneous broadening is necessary to describe the shape of the transient spectra around $t = 0$, when the broadening effect of spectral diffusion is still limited. In a recent publication,¹¹⁵ a similar homogeneous linewidth in HDO:D₂O was observed by means of photon-echo experiments on the OH stretch vibration. After excitation, the distributions $\Delta n_\nu(R, t)$ satisfy the diffusion equation⁶³

$$\frac{\partial \Delta n_\nu}{\partial t} = \frac{L_\nu^2}{\tau_D} \left(\frac{\partial^2 \Delta n_\nu}{\partial R^2} + \beta \Delta n_\nu \frac{d^2 W_\nu}{dR^2} + \beta \frac{\partial \Delta n_\nu}{\partial R} \frac{dW_\nu}{dR} \right), \quad (8.11)$$

where L_ν is the half-width at $e^{-1/2}$ of the maximum of the equilibrium distribution in the potential $W_\nu(R)$, and τ_D is the characteristic time scale for the diffusion process. For a system with harmonic potentials and Gaussian-shaped spectra, the spectral diffusion can be described by the autocorrelation function in Eq. (5.3); the spectral correlation time τ_c is exactly the same as τ_D in Eq. (8.11). Its value can be determined from the time dependence of the first moment of the transient spectrum [see Eq. (5.10)], from which a value of 700 fs follows.³³ For non-parabolic hydrogen-bond potentials, the first moment of the transient spectrum depends has no longer an exponential time dependence. However, we find that for the present hydrogen-bond potentials $W_\nu(R)$, the value of τ_c , as it can be determined from the delay dependence of the calculated first spectral moment, differs negligibly from τ_D . In the following, we will therefore use $\tau_D = \tau_c = 700 \text{ fs}$. We solved Eq. (8.11) numerically by discretizing the R and t in steps $\delta R = 0.004 \text{ \AA}$ and $\delta t = 2 \text{ fs}$, respectively (see §7.6.4 for details). According to this diffusion equation, the populations Δn will evolve towards the thermal distribution discussed in §8.3.2. To translate the resulting time-dependent $\Delta n_\nu(\omega, t)$ to the transient spectrum, we use Eq. (8.9) for $t \geq 0$, which we convolve with the pump-probe cross-correlate, with a duration of 300 fs FWHM (§2.6).

The above modeling of spectral diffusion describes the hydrogen-bond dynamics in the adiabatic approximation, in which no transitions from the $\nu = 1$ to the $\nu = 0$ population are possible. Non-adiabatic transitions, or vibrational relaxation, are likely to have a strong impact on the hydrogen-bond dynamics, since the released vibrational energy is converted to kinetic energy of the hydrogen-bond motion. However, vibrational relaxation of an OH oscillator also implies that the latter has returned to the vibrational ground state, where it no longer contributes to the $\nu = 0 \rightarrow 1$ and $\nu = 1 \rightarrow 2$ bands in the transient spectrum. Thus, the hydrogen-bond dynamics observed in the transient spectra are the result of purely adiabatic dynamics, i.e. the dynamics of those oscillators that do not undergo vibrational relaxation. We note here that the excitation of the hydrogen bond accompanying the vibrational relaxation causes a measurable temporary blueshift of the relaxed OH stretch vibration, as we saw in Chapter 4. This blueshift may affect the transient spectrum to a small extent, but we neglected it in the present analysis.

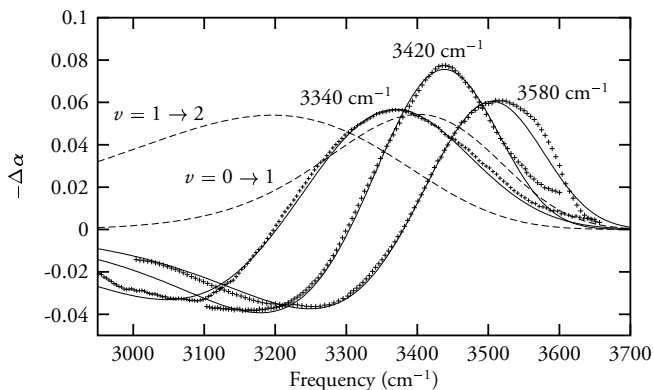


FIGURE 8.6. Transient spectra of HDO:D₂O, pumped at three different frequencies, at delay $t = 0.30$ ps. Data points: experiment (by Gallot and co-workers^{33,35}); drawn curves: QLS model; dashed curves: equilibrated spectra of $0 \rightarrow 1$ and $1 \rightarrow 2$ transitions of the OH band.

8.4.2 INERTIAL DYNAMICS

Because the time resolution is limited by the pump–probe cross-correlation function (with its 300 fs FWHM duration), the data in Fig. 8.1 do not display spectral relaxation very clearly. However, Gallot and co-workers have performed similar experiments^{33,35} with a better time resolution (cross-correlate 210 fs) and have kindly placed their data at our disposal. In their data, the broadening and the shift of the bleaching band are very clearly visible. However, the modeling of the hydrogen-bond dynamics with a single diffusive process does not provide a good description of Gallot’s data, especially in the region of the $\nu = 1 \rightarrow 2$ transition. This is illustrated in Fig. 8.8, which shows the frequency at which the induced absorption changes into a bleaching as a function of delay. The pump frequency was 3580 cm^{-1} . The experimentally observed frequencies are compared with the results of two calculations in which the hydrogen-bond dynamics is purely diffusive. At short delay times ($t < 500$ fs), the experimentally observed zero-crossings can be fitted well with a fast diffusion process with a time constant $\tau_c = 600$ fs, but for longer delay times (> 1 ps), this value describes the experimental data poorly. At these longer delay times, a much better description is obtained with $\tau_c = 950$ fs. Hence, during the first 500 fs after excitation, the transient spectra show a rapid shift towards lower frequencies. This rapid shift is followed by a much slower evolution to the final thermal distribution.

The fast process during the first 500 fs is more pronounced at frequencies $< 3450 \text{ cm}^{-1}$ than at frequencies $> 3550 \text{ cm}^{-1}$ in the transient spectra in Ref. 35, which indicates that the fast process has a much stronger effect on the $\nu = 1 \rightarrow 2$ induced absorption spectrum than on the $\nu = 0 \rightarrow 1$ bleaching signal. This observation suggests that the fast process only affects the $\nu = 1$ state. The solid curves in Figs. 8.1 and 8.8 represent the results of a calculation in which the hydrogen-bond length is stochastically modulated in the $\nu = 0$ and $\nu = 1$ state with a time constant of 950(100) fs (i.e. diffusion according to Eq. (8.11)), and in which the excited distribution $\Delta n_1(R, t)$ in the $W_1(R)$ potential has an additional rapid shift over a limited distance, directly following its excitation. This shift, which depends on the elapsed time since excitation, cannot easily be incorporated

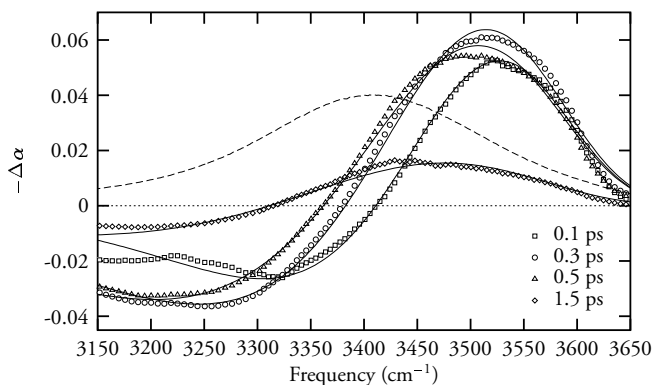


FIGURE 8.7. Transient spectra of HDO:D₂O, pumped at 3580 cm⁻¹ at four pump-probe delays. Data points: experiment (by Gallot and co-workers^{33,35}); drawn curves: QLS model with inertial shift; dashed curve: linear spectrum of the OH band.

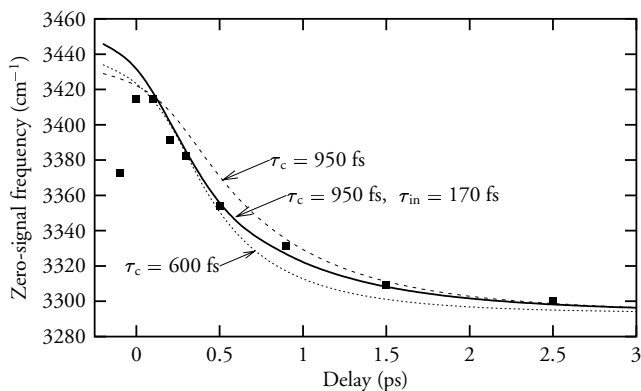


FIGURE 8.8. Frequency at which the bleaching in the transient spectrum changes into an induced absorption as a function of delay. The points were provided by Gallot and co-workers^{33,35} who obtained them by exciting the OH stretch vibration in dilute HDO:D₂O at 3580 cm⁻¹. The dashed curves represent calculations in which the hydrogen-bond length is stochastically modulated (diffusion) in the hydrogen-bond potentials W_0 and W_1 . The solid curve represents a calculation in which the hydrogen bond is stochastically modulated and in addition experiences a fast shift with a time constant $\tau_{in} = 170(40)$ fs towards the minimum of the W_1 potential.

in the time-invariant diffusion equation Eq. (8.11). Therefore, we model the inertial shift phenomenologically in the numerical calculation, with time steps δt and excitation time t_{ex} , with the transformation

$$\Delta n_1(R, t + \delta t) = \Delta n_1(R + \Lambda \delta t, t), \quad (8.12A)$$

$$\Lambda = (S/\tau_{\text{in}}) \exp((t_{\text{ex}} - t)/\tau_{\text{in}}). \quad (8.12B)$$

In the description of this inertial shift, we incorporated the non-zero pulse duration of the pump and probe pulses. From a fit to the Gallot's transient spectra, we find $S = 0.56(12)$ pm for the total distance over which this shift occurs, and $\tau_{\text{in}} = 170(40)$ fs. This value of S corresponds to 45% of the distance between the center of the initially excited hydrogen-bond length distribution and the minimum of the $W_1(R)$ potential.

The presence of a fast initial component in the hydrogen-bond dynamics of the $\nu = 1$ state can be explained as follows. The oscillation in the hydrogen-bond coordinate R is overdamped, which means that each individual oscillator has a local hydrogen-bond potential that is determined both by the potential W_0 and by the local configuration of the liquid. The excitation with a short pump pulse to the $\nu = 1$ state leads to a rapid change of W_0 to W_1 , and thereby to a change of the local potential. This change of the local potential induces a rapid adaptation of the hydrogen-bond length. For the hole that is burnt in $\nu = 0$, the local potential does not change, and therefore the dynamics of the hole only result from the diffusive reorganization of the local liquid structure. The presence of a significant fast component in the hydrogen-bond dynamics of liquid water implies that water molecules can adapt to changes in charge distribution or molecular orientation (for instance as a result of chemical reactions) on a time scale that is much shorter than that of the spontaneous reorganization of the liquid.

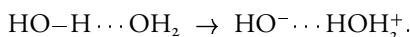
The time constant $\tau_{\text{in}} = 170(40)$ fs of the contraction of the hydrogen-bond length in the $\nu = 1$ state is much shorter than the time constant $\tau_c = 950(100)$ fs of the spontaneous reorganization of the liquid. This suggests that the fast initial response is a local effect, involving only a few water molecules. Nevertheless, τ_{in} is still much longer than the inverse angular frequency of the undamped $\text{OH} \cdots \text{O}$ hydrogen-bond stretch vibration (the inverse of $\omega = 200 \text{ cm}^{-1}$ is 27 fs).⁴⁷ Hence, the fast adaptation of the hydrogen-bond length is still an overdamped motion. The time constant $\tau_{\text{in}} = 170$ fs is very similar to that of the fast component of the dielectric relaxation of liquid water that was recently observed with THz reflection spectroscopy.^{103,104} This fast dielectric component was also assigned to a local reorganization involving only one or a few water molecules.

8.5 AUTODISSOCIATION OF WATER

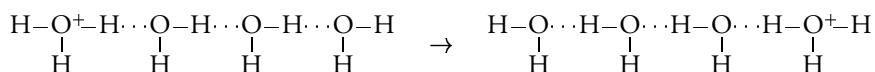
The strong delocalization of the $\nu = 2$ state (Fig. 8.4), especially for hydrogen-bond lengths $R \leq 2.7 \text{ \AA}$, has interesting implications. A direct excitation of the $\nu = 0 \rightarrow 2$ transition is known to lead to an increased, non-thermal, concentration of H_3O^+ and OH^- ions in pure water. This excess concentration decays on a microsecond time scale due to the recombination of the H_3O^+ and OH^- ions back to water.^{40,59} However, the exact mechanism that converted the vibrational energy to a dissociation was not clear. We can now understand this dissociation mechanism from the fact that in the $\nu = 2$ state, the

hydrogen atom becomes strongly delocalized between the oxygen atoms of two hydrogen-bonded water molecules. The excitation from the localized $\nu = 0$ ground state to this delocalized $\nu = 2$ state implies a partial transfer of the hydrogen atom to the other oxygen atom in the $\text{DO}-\text{H}\cdots\text{OD}_2$ system. This means that the excitation leads to a high probability for the formation of an oxygen atom to which only one hydrogen is bound and an oxygen atom to which three hydrogen atoms are bound. If this hopping of the hydrogen atom is associated with a charge transfer, not a hydrogen atom but a proton is transferred, which results in the formation of an H_3O^+ ion and an OH^- ion.

Closely related to the above photo-induced dissociation is the (spontaneous) autodissociation reaction



The rightmost ion, the hydronium ion, exists in ordinary liquid water with a concentration of 10^{-7} mol/l (hence, $\text{pH} = 7$). Recent theoretical work^{84,37} showed that such an autodissociation will become semi-permanent if the hydronium ion is transported away from the OH^- ion via a Grotthuss conduction mechanism,^d in which not the ion itself is transported but rather its charge, along a 'hydrogen-bond wire':



We will now see that the $\nu = 2$ state of the OH stretch vibration is related to this autodissociation reaction. The first step in the autodissociation of water is the transfer of a proton between two hydrogen-bonded water molecules, a fact that was recently shown by *ab initio* molecular dynamics simulations.³⁷ However, these simulations do not give information on the (quantum) nature of the transition state of the first proton-transfer step, since they describe the nuclear dynamics classically.

8.5.1 TRANSITION STATE

In the following we will calculate the energy required to induce proton transfer in the $\text{DOH}\cdots\text{OD}_2$ system formed by an HDO and a D_2O molecule for the different quantum states of the OH stretch vibration. In this calculation, we will use the knowledge from §8.3.1 of the potentials V_I and V_{II} . Proton transfer can occur when the proton has a significant probability amplitude at a distance r_{\min} from the right oxygen atom in the $\text{OH}\cdots\text{O}$ system, with r_{\min} the equilibrium OH bond length in the $\nu = 0$ state. This requirement will be fulfilled if the energy of the occupied vibrational state of the OH stretch vibration exceeds $V_I(r, R)$ at $r = R - r_{\min}$. Proton transfer can thus be induced by shortening the hydrogen-bond length and/or by exciting the OH stretch vibration to a

^dVon Grotthuss,²⁰ who published his experiments on the electrolysis of salt solutions in 1806, knew about neither protons nor ionic dissociation of salts. He assumed, conforming to the ideas of his time, that in a salt solution, both the water and the salt existed as small neutral particles. He tried to explain the formation of different products at the two electrodes by proposing that each neutral particle consisted of a positive and negative half. Upon electrolysis, salt and water wires would form that extended from cathode to anode, in which a conduction mechanism similar to the above hydronium transport took place. His insight that salts are composed of ions was brilliant, but the 'wire theory' ultimately turned out inaccurate. However, the mechanism for proton and hydroxyl ion transport over short distances, being the only case where the wire theory applies, is named in honor of Von Grotthuss.

TABLE 8.1. Calculated energy $E_{T,v}$ required for proton transfer in a hydrogen-bonded $\text{DOH} \cdots \text{OD}_2$ system, for the five lowest quantum states ν of the O–H stretch vibration and the corresponding distances $R_{\text{eq},\nu} - R_{T,\nu}$ over which the hydrogen bond is contracted compared to the ground-state equilibrium value $R_{\text{eq},0} = 2.85 \text{ \AA}$. The strong delocalization of the vibrational states for $\nu \geq 3$ means that proton transfer can occur without contraction.

quantum number ν of transition state	Contraction (pm)	Transition energy (cm^{-1})	(kJ/mol)
0	41	12447	149
1	35	8976	107
2	25	6533	78
3	–	7044	84
4	–	8466	101

delocalized state. To determine the energy required for this transfer in the vibrational state ν , we solve $E_\nu(R) = V_{\text{I}}(R - r_{\text{min}}, R)$ for R . The value of R at which this equality holds is denoted as $R_{T,\nu}$, whose values are shown in Table 8.1. For the higher vibrational states, $R_{T,\nu} > R_{\text{eq},\nu}$, which means that the energy $E_\nu(R)$ already exceeds $V_{\text{I}}(R - r_{\text{min}}, R)$ at the equilibrium distance $R_{\text{eq},\nu}$. The proton transfer energy for state ν is: $E_{T,\nu} = E_\nu(R_{T,\nu}) + V_{\text{II}}(R_{T,\nu}) - E_0(R_{\text{eq},0}) - V_{\text{II}}(R_{\text{eq},0})$, with $R_{\text{eq},0} = 2.85 \text{ \AA}$. The resulting energies $E_{T,\nu}$ are shown in Table 8.1.

For the $\nu = 0$ and $\nu = 1$ states, the proton transfer requires a strong shortening of the hydrogen bond, which has a high associated energy cost. For the $\nu = 2$ state, no contraction of the hydrogen bond is required, because of the delocalized character of the proton in this state. The proton is also delocalized in the $\nu = 3$ and $\nu = 4$ states, but these states require a larger excitation energy than the $\nu = 2$ state. Hence, the $\nu = 2$ state of the OH stretch vibration is the most favorable transition state for getting proton transfer from an HDO molecule to a D_2O molecule. This result agrees with the observation in photolysis experiments that excitation of the $\nu = 2$ state already suffices to generate a high concentration of non-thermal excess protons and hydroxyl ions.^{49,59} The required activation energy $E_{T,2}$ of 6500 cm^{-1} (78 kJ/mol) for autodissociation is less than 20% of the OH binding energy. This illustrates the strong effect of hydrogen bonds on the OH bonds of the water molecule.

For pure H_2O , the interactions between the OH stretch vibrations and the $\text{OH} \cdots \text{O}$ hydrogen bonds are similar to those in a solution of HDO in D_2O . Therefore, we expect the same qualitative behavior for the mechanism of proton transfer between two H_2O molecules. Quantitatively there will be small differences, because the OH stretch vibrations of the H_2O molecule form delocalized symmetric and asymmetric modes. The energy of the $\nu = 2$ state of the symmetric mode is lower and that of the asymmetric mode is higher than the energy of the $\nu = 2$ state of HDO molecule. These energy differences will lead to small changes in the value of the oxygen-oxygen distance $R_{T,2}$ at which proton transfer becomes possible.

The proton-transfer energy $E_{T,2}$ of $6,500 \text{ cm}^{-1}$ represents the lowest possible activation energy for proton transfer between two water molecules. This energy is expected to be somewhat higher than the overall enthalpy change ΔH of the autodissociation reaction. ΔH can be calculated using the Van 't Hoff isochore $d \ln K_w / dT = \Delta H / k_B T^2$, with

K_w the autoprotolysis constant of water; $K_w = a(\text{H}_3\text{O}^+) \cdot a(\text{OH}^-) = 1.008 \times 10^{-14}$ at $T = 298$ K, which corresponds to $p\text{H} = 7$). From the temperature dependence of K_w ,² it follows that $\Delta H = 5500 \text{ cm}^{-1}$ (66 kJ/mol) at 298 K, which is approximately 1000 cm^{-1} less than the activation energy $E_{T,2}$, which can be explained from the solvation of the produced H_3O^+ and OH^- ions.

8.5.2 MECHANISM

Because the *ab initio* simulations on the autodissociation of water³⁷ did not describe the motions of the nuclei quantum-mechanically, the present findings provide complementary information on the microscopic mechanism of the autodissociation reaction. This mechanism likely consists of the following steps. (i) Fluctuations of the local water structure lead to excitation of an OH stretch mode to the $\nu = 2$ state. (ii) This excitation induces a contraction of the hydrogen bond to its new equilibrium length of 2.65 Å (Fig. 8.3). (iii) The contraction leads to a decrease of the barrier in the potential V_1 (Fig. 8.4). The resulting delocalization of the $\nu = 2$ state enables transfer of the proton to the other (right-hand) oxygen atom. (iv) The proton transfer is followed by a spatial separation of the OH^- and the H_3O^+ ion via proton conduction along the hydrogen-bonded network formed by the surrounding water molecules.^{84,118,117} (v) The proton conduction should be followed by a cleavage of the hydrogen-bond network to avoid recombination via the reverse proton-conduction mechanism.³⁷

Finally, it should be noted that the hydrogen bonds formed between water and molecules different from water (e.g., dissolved acids and bases) can show a similar effect on the OH stretch frequency as the hydrogen bond between two water molecules. In view of this similarity, we can expect that the proton-transfer reactions between water and these other molecules also proceed via the excited quantum states of the OH stretch vibration. This should be verified in future experimental studies.

8.6 CONCLUSIONS

We investigated the transient spectrum of vibrationally excited HDO dissolved in D_2O . The transient absorption ($\nu = 1 \rightarrow 2$) of the OH stretch mode is strongly asymmetric and much broader than the linear ($\nu = 0 \rightarrow 1$) absorption spectrum. The shape of the $\nu = 1 \rightarrow 2$ absorption spectrum can be explained from the strong (anharmonic) interactions between the OH stretch vibration and the $\text{OH} \cdots \text{O}$ hydrogen-bond. These anharmonic interactions are quantitatively described with a quantum-mechanical version of the Lippincott-Schroeder (QLS) model. This model also provides an accurate description of the relations between the hydrogen-bond length, the OH bond length and the OH stretch frequency.

From a detailed study of the transient spectral responses at different delays, we find that the dynamics of the hydrogen-bond length in both the $\nu = 0$ and the $\nu = 1$ state of the OH stretch vibration are diffusive processes with a time constant $\tau_c = 950(100)$ fs. These diffusive dynamics result from the spontaneous reorganisations of liquid water. For the $\nu = 1$ state, the hydrogen-bond dynamics contain an additional fast component with a time constant $\tau_{\text{in}} = 170(40)$ fs. This fast component is observed directly after excitation

of the $\nu = 1$ state out of $\nu = 0$, and results from the rapid contraction of the hydrogen bond towards its new equilibrium position in this state.

The wave function of the $\nu = 2$ state of the OH stretch mode is strongly delocalized, which implies that an excitation to the $\nu = 2$ state can initiate an autodissociation reaction $2\text{H}_2\text{O} \rightarrow \text{OH}^- + \text{H}_3\text{O}^+$. The energy required for this excitation is in good agreement with the estimated activation energy for the autodissociation in water.

APPENDIX: THE cm^{-1} UNIT

For the uninitiated, the spectroscopist's habit of using the unit cm^{-1} for both frequency and energy is often confusing. The cm^{-1} (pronounced as 'reciprocal centimeter') is formally the unit for the quantity $\tilde{\nu}$, called *wave number* (i.e. the inverse of a wavelength). However, it is often used as a unit for frequency (i.e. the frequency of light in vacuum that corresponds to that wave number), for angular frequency, or for energy (i.e. the energy of a photon at that wave number). Table 8.2 provides the appropriate conversion formulas; Table 8.3 provides some fundamental constants in cm^{-1} units.

TABLE 8.2. Converting $\tilde{\nu}$ expressed in cm^{-1} to other quantities. The symbolic conversion factors assume SI units.

Desired quantity	Conversion	
	(numeric)	(symbolic)
Energy (J)	$1.9865 \times 10^{-23} \times \tilde{\nu}$	$100hc\tilde{\nu}$
Energy (eV)	$123.99 \times 10^{-6} \times \tilde{\nu}$	$100hc\tilde{\nu}/e$
Energy (J mol^{-1})	11.963	$100hcN_A$
Frequency ν (Hz)	$29.978 \times 10^9 \times \tilde{\nu}$	$100c\tilde{\nu}$
Frequency ω (rad s^{-1})	$0.18836 \times 10^{12} \times \tilde{\nu}$	$200\pi c\tilde{\nu}$
Characteristic time $t = 1/\omega$ (s)	$5.3091 \times 10^{-12}/\tilde{\nu}$	$1/200\pi c\tilde{\nu}$
Wavelength (nm)	$10^7/\tilde{\nu}$	$10^7/\tilde{\nu}$
Wavelength (μm)	$10^4/\tilde{\nu}$	$10^4/\tilde{\nu}$

TABLE 8.3. Fundamental constants in spectroscopic units. The symbolic expressions assume SI units.

Fundamental constant	Value		
		(symbolic)	
Boltzmann's constant	k_B	$0.69503 \text{ cm}^{-1}\text{K}^{-1}$	$k_B / 100 hc$
Planck's constant (in $h\nu$)	h	1	1
Planck's constant (in $\hbar\omega$)	\hbar	1	1

BIBLIOGRAPHY

1. S. M. Arrivo, T. P. Dougherty, W. T. Grubbs, and E. J. Heilweil. Ultrafast infrared-spectroscopy of vibrational co-stretch up-pumping and relaxation dynamics of $\text{W}(\text{CO})_6$. *Chem. Phys. Lett.* **235**, 247–254 (1995).
2. P. W. Atkins. *Physical Chemistry*. Oxford University Press, Oxford, 1990.
3. M.-P. Bassez, J. Lee, and G. W. Robinson. Is liquid water really anomalous? *J. Phys. Chem.* **91**, 5818–5825 (1987).
4. N. Bloembergen, E. M. Purcell, and R. V. Pound. Relaxation effects in nuclear magnetic resonance absorption. *Phys. Rev.* **73**, 679–712 (1948).
5. M. Bonn, M. J. P. Brugmans, A. W. Kleyn, R. A. van Santen, and H. J. Bakker. Infrared picosecond transient hole-burning studies of the effect of hydrogen bonds on the vibrational line shape. *J. Chem. Phys.* **105**, 3431–3442 (1996).
6. T. A. Boyd. *Nonlinear Optics*. Academic Press Inc., San Diego, 1992.
7. S. Bratos. Profiles of hydrogen stretching IR bands of molecules with hydrogen bonds: a stochastic theory. I. Weak and medium strength hydrogen bonds. *J. Chem. Phys.* **63**, 3499–509 (1975).
8. S. Bratos and J.-C. Leicknam. Ultrafast infrared pump-probe spectroscopy of water: a theoretical description. *J. Chem. Phys.* **101**, 4536–4546 (1994).
9. S. Bratos and J.-C. Leicknam. Subpicosecond transient infrared-spectroscopy of water: a theoretical description. *J. Chem. Phys.* **103**, 4887–4893 (1995).
10. M. J. P. Brugmans, M. Bonn, H. J. Bakker, and A. Lagendijk. Multiphonon decay of stretch vibrations in zeolites. *Chem. Phys.* **201**, 215 (1995).
11. F. Bruni, M. A. Ricci, and A. K. Soper. Structural characterization of NaOH aqueous solution in the glass and liquid states. *J. Chem. Phys.* **114**, 8056–8063 (2001).
12. R. Buchner, G. Hefter, P. M. May, and P. Sipos. Dielectric relaxation of dilute aqueous NaOH, $\text{NaAl}(\text{OH})_4$, and $\text{NaB}(\text{OH})_4$. *J. Phys. Chem. A* **103**, 11186–11190 (1999).
13. A. I. Buhrshtein and V. S. Malinovsky. Free-induction decay in the framework of sudden-modulation theory. *J. Opt. Soc. Am. B* **8**, 1098–1113 (1991).
14. E. A. Carter and J. T. Hynes. Solvation dynamics for an ion-pair in a polar solvent: time-dependent fluorescence and photochemical charge-transfer. *J. Chem. Phys.* **94**, 5961–5979 (1991).

15. A. Chandra and T. Ichiye. Dynamical properties of the soft sticky dipole model of water: Molecular dynamics simulations. *J. Chem. Phys.* *111*, 2701 (1999).
16. Y. J. Chang and E. W. Castner. Fast responses from slowly relaxing liquids—a comparative-study of the femtosecond dynamics of triacetin, ethylene-glycol, and water. *J. Chem. Phys.* *99*, 7289–7299 (1993).
17. C. Chaudhuri, Y. S. Wang, J. C. Jiang, J. C. Jiang, Y. T. Lee, H. C. Chang, and G. Niedner-Schatteburg. Infrared spectra and isomeric structures of hydroxide ion-water clusters $\text{OH}^- (\text{H}_2\text{O})_{1-5}$: a comparison with $\text{H}_3\text{O}^+ (\text{H}_2\text{O})_{1-5}$. *Mol. Phys.* *99*, 1161–1173 (2001).
18. D. J. Cook and R. M. Hochstrasser. Intense terahertz pulses by four-wave rectification in air. *Opt. Lett.* *25*, 1210–1212 (2000).
19. G. Dahlquist, A. Björk, and N. Anderson. *Numerical methods*. Prentice-Hall, Eaglewood Cliffs, 1974.
20. C. J. T. de Grotthuss. Mémoire sur la décomposition de l'eau et des corps qu'elle tient en dissolution à l'aide de l'électricité galvanique. *Annales de Chimie* *58*, 54–74 (1806).
21. J. C. Deak, S. T. Rhea, L. K. Iwaki, and D. D. Dlott. Vibrational energy relaxation and spectral diffusion in water and deuterated water. *J. Phys. Chem. A* *104*, 4866–4875 (2000).
22. P. Debye. *Polar molecules*. Dover Publications, Inc., New York, 1929.
23. M. H. Dunn and M. Ebrahimzadeh. Parametric generation of tunable light from continuous-wave to femtosecond pulses. *Science* *286*, 1513–1517 (1999).
24. C. G. Durfee, S. Backus, M. M. Murnane, and H. C. Kapteyn. Ultrabroadband phase-matched optical parametric generation in the ultraviolet by use of guided waves. *Opt. Lett.* *22*, 1565–1567 (1997).
25. D. Eisenberg and W. Kauzmann. *The structure and properties of water*. Oxford University Press, New York, 1969.
26. K. Ekvall, P. van der Meulen, C. Dhollande, L.-E. Berg, S. Pommeret, R. Naskrecki, and J.-C. Mialocq. Cross phase modulation artifact in liquid phase transient absorption spectroscopy. *J. Appl. Phys.* *87*, 2340–2352 (2000).
27. U. Emmerichs, S. Woutersen, and H. J. Bakker. Generation of intense femtosecond optical pulses around $3 \mu\text{m}$ with kHz rep-rate. *J. Opt. Soc. Am. B* *14*, 1480 (1997).
28. T. A. Ford and M. Falk. Hydrogen bonding in water and ice. *Can. J. Chem.* *46*, 3579 (1968).
29. T. Förster. Transfer mechanisms of electronic excitation. *Discussions Faraday Soc.* *27*, 7–17 (1959).
30. F. Franks, editor. *Water: a comprehensive treatise*, volume 3. Plenum Press, New York, 1973.

31. F. Franks. *Water*. Royal Society of Chemistry, London, 1983.
32. L. E. Fried, N. Bernstein, and S. Mukamel. Simulation of the femtosecond optical-response of a solute in water. *Phys. Rev. Lett.* **68**, 1842–1845 (1992).
33. G. M. Gale, G. Gallot, F. Hache, N. Lascoux, S. Bratos, and J.-Cl. Leicknam. Femtosecond dynamics of hydrogen bonds in liquid water: a real time study. *Phys. Rev. Lett.* **82**, 1068–1071 (1999).
34. G. M. Gale, G. Gallot, F. Hache, and R. Sander. Generation of intense highly coherent femtosecond pulses in the mid infrared. *Opt. Lett.* **22**, 1253–1255 (1997).
35. G. Gallot. *Génération d'impulsions femtoseconde intenses, accordables dans l'infrarouge moyen. Dynamique de la liaison hydrogène dans l'eau liquide*. PhD thesis, Ecole Polytechnique, Palaiseau, France, 1998.
36. G. Gallot, N. Lascoux, G. M. Gale, J.-C. Leicknam, S. Bratos, and S. Pommeret. Non-monotonic decay of transient infrared absorption in dilute HDO/D₂O solutions. *Chem. Phys. Lett.* **341**, 535–539 (2001).
37. P. L. Geissler, C. Dellago, D. Chandler, J. Hutter, and M. Parrinello. Autoionization in liquid water. *Science* **291**, 2121–2124 (2001).
38. P. A. Giguère. Les liaisons hydrogène dans les solutions aqueuses d'alcalis. *Rev. Chim. Minérale* **20**, 588–594 (1983).
39. C. C. Gillispie, editor. *Dictionary of Scientific Biography*. Charles Scribner's Sons, New York, 1970.
40. D. M. Goodall and R. C. Greenhow. Ionization of water induced by vibrational excitation using a neodymium:glass laser. *Chem. Phys. Lett.* **9**, 583–86 (1971).
41. B. C. Gordalla and M. D. Zeidler. Molecular dynamics in the system water-dimethylsulphoxide: A N.M.R. relaxation study. *Mol. Phys.* **59**, 817–828 (1986).
42. H. Graener. The equilibration of vibrational excess energy. *Chem. Phys. Lett.* **165**, 110–114 (1990).
43. H. Graener and G. Seifert. Vibrational and orientational relaxation of monomeric water molecules in liquids. *Chem. Phys. Lett.* **98**, 35–45 (1992).
44. H. Graener, G. Seifert, and A. Laubereau. Direct observation of rotational relaxation times by time-resolved infrared spectroscopy. *Chem. Phys. Lett.* **172**, 435–439 (1990).
45. H. Graener, G. Seifert, and A. Laubereau. New spectroscopy of water using tunable picosecond pulses in the infrared. *Phys. Rev. Lett.* **66**, 2092–2095 (1991).
46. H. Graener, T. Q. Ye, and A. Laubereau. Ultrafast dynamics of hydrogen bonds directly observed by time-resolved infrared spectroscopy. *J. Chem. Phys.* **90**, 3413–3416 (1989).

47. B. Guillot. A molecular dynamics study of the far infrared spectrum of liquid water. *J. Chem. Phys.* 95, 1543–51 (1991).
48. P. Hamm, C. Lauterwasser, and W. Zinth. Generation of tunable subpicosecond light-pulses in the midinfrared between 4.5 and 11.5 μm . *Opt. Lett.* 18, 1943–1945 (1993).
49. P. Hamm, M. Lim, and R. M. Hochstrasser. Structure of the amide I band of peptides measured by femtosecond nonlinear-infrared spectroscopy. *J. Phys. Chem. B* 102(31), 6123–6138 (1998).
50. E. H. Hardy, A. Zygari, M. D. Zeidler, M. Holz, and F. D. Sacher. Isotope effect on the translational and rotational motion in liquid water and ammonia. *J. Chem. Phys.* 114, 3174–3181 (2001).
51. E. J. Heilweil, M. P. Casassa, R. R. Cavanagh, and J. C. Stephenson. Temperature dependence of the vibrational population lifetime of OH($\nu = 1$) in fused silica. *Chem. Phys. Lett.* 117, 185–189 (1985).
52. G. Herzberg. *Molecular spectra and molecular structure*. D. van Nostrand, New York, 1950.
53. J. C. Hindman, A. Svirnickas, and M. Wood. Relaxation processes in water. a study of the proton spin-lattice relaxation time. *J. Chem. Phys.* 59, 1517–1522 (1974).
54. J. D. Jackson. *Classical Electrodynamics*. John Wiley & Sons, Inc., New York, second edition, 1975.
55. J. Jonas, T. DeFries, and D. J. Wilbur. Molecular motions in compressed liquid water. *J. Chem. Phys.* 65, 582–588 (1976).
56. R. A. Kaindl, M. Wurm, K. Reimann, P. Hamm, A. M. Weiner, and M. Woerner. Generation, shaping, and characterization of intense femtosecond pulses tunable from 3 to 20 μm . *J. Opt. Soc. Am. B* 17, 2086–2094 (2000).
57. J. T. Kindt and C. A. Schmuttenmaer. Far-infrared dielectric properties of polar liquids probed by femtosecond terahertz pulse spectroscopy. *J. Phys. Chem.* 100, 10373–10379 (1996).
58. P. I. Klocek, editor. *Handbook of infrared optical materials*. Marcel Dekker, Inc., New York, 1991.
59. B. Knight, D. M. Goodall, and R. C. Greenhow. Single-photon vibrational photochemistry. *J. Chem. Soc. Faraday II* 75, 291–295 (1979).
60. S. A. Kovalenko, A. L. Dobryakov, J. Ruthmann, and et al. Femtosecond spectroscopy of condensed phases with chirped supercontinuum probing. *Phys. Rev. A* 59, 2369–2384 (1999).
61. D. Kroh and A. Ron. The overtone spectra of H₂O, D₂O, and mixtures of H₂O in D₂O ice. *Chem. Phys. Lett.* 36, 527–530 (1975).

-
62. M. F. Kropman and H. J. Bakker. Dynamics of water molecules in aqueous solvation shells. *Science* 291, 2118–2120 (2001).
63. R. Kubo, M. Toda, and N. Hashitsume. *Statistical Physics II: Nonequilibrium statistical mechanics*. Springer-Verlag, Berlin, 1995.
64. D.J. Kushner, Alison Baker, and T.G. Dunstall. Pharmacological uses and perspectives of heavy water and deuterated compounds. *Can. J. Physiology and Pharmacology* 77, 79–88 (1999).
65. R. Laenen, G. M. Gale, and N. Lascoux. IR spectroscopy of hydrogen-bonded methanol: vibrational and structural relaxation on the femtosecond time scale. *J. Phys. Chem. A* 103, 10708–10712 (1999).
66. R. Laenen and C. Rauscher. Transient hole-burning spectroscopy of associated ethanol molecules in the infrared: structural dynamics and evidence for energy migration. *J. Chem. Phys.* 106, 8974–8980 (1997).
67. R. Laenen, C. Rauscher, and A. Laubereau. Local substructures of water studied by transient hole-burning spectroscopy in the infrared: dynamics and temperature dependence. *J. Phys. Chem. B* 102, 9304–9311 (1998).
68. D. Lankhorst, J. Schriever, and J. C. Leyte. Determination of the rotational correlation time of water by proton NMR relaxation in H_2^{17}O and some related results. *Ber. Bunsengesellschaft Phys. Chem.* 86, 215–221 (1982).
69. A. Laubereau, L. Greiter, and W. Kaiser. Intense tunable picosecond pulses in the infrared. *Appl. Phys. Lett.* 25, 87 (1974).
70. H. M. Leicester. *The historical background of chemistry*. John Wiley and Sons, New York, 1956. Republished in 1971 by Dover, New York.
71. F. O. Libnau, O. M. Kvalheim, A. A. Christy, and J. Toft. Spectra of water in the near- and mid-infrared region. *Vibrational Spectroscopy* 7, 243–254 (1994).
72. D. R. Lide, editor. *CRC Handbook of Chemistry and Physics*. CRC Press, Boca Raton, 75th edition, 1994.
73. E. R. Lippincott and R. Schroeder. One-dimensional model of the hydrogen bond. *J. Chem. Phys.* 23, 1099–1106 (1955).
74. A. J. Lock, S. Woutersen, and H. J. Bakker. Ultrafast energy equilibration in hydrogen-bonded liquids. *J. Phys. Chem. A* 105, 1238–1243 (2001).
75. W. A. P. Luck. The angular dependence of hydrogen bond interactions. In P. Schuster, G. Zundel, and C. Sandorfy, editors, *The Hydrogen Bond*, volume II, chapter 11. North Holland, Amsterdam, 1976.
76. W. A. P. Luck. Semiclassical model calculations of weak, strong, and short O–H \cdots O H-bonds. *Can. J. Chem.* 69, 1819–1826 (1991).

77. H. D. Lutz. Bonding and structure of water-molecules in solid hydrates—correlation of spectroscopic and structural data. *Struct. Bond. (Berlin)* 69, 97–125 (1988).
78. D. Madsen, J. Stenger, J. Dreyer, E. T. J. Nibbering, P. Hamm, and T. Elsaesser. Coherent vibrational ground-state dynamics of an intramolecular hydrogen bond. *Chem. Phys. Lett.* 341, 56–62 (2001).
79. I. H. Malitson. Refraction and dispersion of synthetic sapphire. *J. Opt. Soc. Am.* 52, 1377–1379 (1962).
80. I. H. Malitson. A redetermination of some optical properties of calcium fluoride. *Appl. Opt.* 2, 1103–1107 (1963).
81. I. H. Malitson. Refractive properties of barium fluoride. *J. Opt. Soc. Am.* 54, 628 (1964).
82. Y. Marechal and A. Witkowski. Infrared spectra of H-bonded systems. *J. Chem. Phys.* 48, 3697–3703 (1968).
83. M. Maroncelli and G. R. Fleming. Computer-simulation of the dynamics of aqueous solvation. *J. Chem. Phys.* 89, 5044–5069 (1988).
84. D. Marx, M. E. Tuckerman, J. Hutter, and M. Parrinello. The nature of the hydrated excess proton in water. *Nature* 397, 601–604 (1999).
85. W. Mikenda. Stretching frequency versus bond distance correlation of O–D(H)···Y (Y = N, O, S, Se, Cl, Br, I) hydrogen bonds in solid hydrates. *J. Mol. Struct.* 147, 1–15 (1986).
86. R. E. Miller. The vibrational spectroscopy and dynamics of weakly bound neutral complexes. *Science* 240, 447 (1988).
87. M. Moskovits and K. M. Michaelian. Alkali hydroxide ion pairs. A Raman study. *J. Am. Chem. Soc.* 102, 2209–2215 (1980).
88. S. Mukamel. *Principles of nonlinear optical spectroscopy*. Oxford University Press, Oxford, 1991.
89. D. L. Myers, M. Shigeiwa, C. Stromberg, M. D. Fayer, and B. J. Cherayil. Temperature dependence of solute vibrational relaxation in supercritical fluids: experiment and theory. *Chem. Phys. Lett.* 325, 619–626 (2000).
90. A. Nitzan and J. Jortner. Vibrational relaxation of a molecule in a dense medium. *Mol. Phys.* 25, 713–734 (1973).
91. A. Nitzan, S. Mukamel, and J. Jortner. Energy gap law for vibrational relaxation of a molecule in a dense medium. *J. Chem. Phys.* 63, 200 (1975).
92. A. Novak. Hydrogen bonding in solids. correlation of spectroscopic and crystallographic data. *Struct. Bonding (Berlin)* 18, 177 (1974).

-
93. H. Okamoto and M. Tasumi. Generation of ultrashort light-pulses in the midinfrared ($3000\text{--}800\text{ cm}^{-1}$) by 4-wave-mixing. *Opt. Commun.* *121*, 63–68 (1995).
 94. J. C. Owrutsky, M. Li, B. Locke, and R. M. Hochstrasser. Vibrational-relaxation of the CO stretch vibration in hemoglobin-CO, myoglobin-CO, and protoheme-CO. *J. Phys. Chem.* *99*, 4842–4846 (1995).
 95. D. W. Oxtoby and S. A. Rice. On vibrational relaxation in liquids. *Chem. Phys. Lett.* *42*, 1–7 (1976).
 96. S. Palese, L. Schilling, R. J. Dwayne Miller, P. Randall Staver, and W. T. Lotshaw. Femtosecond optical Kerr effect studies of water. *J. Phys. Chem.* *98*, 6308–6316 (1994).
 97. V. Petrov and F. Noack. Tunable femtosecond optical parametric-amplifier in the midinfrared with narrow-band seeding. *J. Opt. Soc. Am. B* *12*, 2214–2221 (1995).
 98. V. Petrov, F. Rotermund, F. Noack, and P. Schunemann. Femtosecond parametric generation in ZnGeP_2 . *Opt. Lett.* *24*, 414–416 (1999).
 99. J. R. Pliego and J. M. Riveros. *Ab initio* study of the hydroxide ion–water clusters: an accurate determination of the thermodynamic properties for the processes $n\text{H}_2\text{O} + \text{OH}^- \rightarrow \text{HO}^-(\text{H}_2\text{O})_n$ ($n=1\text{--}4$). *J. Chem. Phys.* *112*, 4045–4052 (2000).
 100. W. H. Press, S. A. Teukolsky, W. T. Vetterling, and B. P. Flannery. *Numerical recipes in C: the art of scientific computing*. Cambridge University Press, Cambridge, second edition, 1992.
 101. G. N. Robertson and J. Yarwood. Vibrational relaxation of hydrogen-bonded species in solution. I. Theory. *Chem. Phys.* *32*, 267–282 (1978).
 102. G. W. Robinson, C. H. Cho, and J. Urquidi. Isosbestic points in liquid water: further strong evidence for the two-state mixture model. *J. Chem. Phys.* *111*, 698–702 (1999).
 103. C. Rønne, P.-O. Åstrand, and S. R. Keiding. THz spectroscopy of liquid H_2O and D_2O . *Phys. Rev. Lett.* *82*, 2888–2891 (1999).
 104. C. Rønne, L. Thrane, P.-O. Åstrand, A. Wallqvist, K. V. Mikkelsen, and S. R. Keiding. Investigation of the temperature dependence of dielectric relaxation in liquid water by THz reflection spectroscopy and molecular dynamics simulation. *J. Chem. Phys.* *107*, 5319–5331 (1997).
 105. J. Ropp, C. Lawrence, T. C. Farrar, and J. L. Skinner. Rotational motion in liquid water is anisotropic: A nuclear magnetic resonance and molecular dynamics simulation study. *J. Am. Chem. Soc.* *123*, 8047–8052 (2001).
 106. M. Rozenberg, A. Loewenschuss, and Y. Marcus. An empirical correlation between stretching vibration redshift and hydrogen bond length. *Phys. Chem. Chem. Phys.* *2*, 2699–2702 (2000).

107. M. G. Sceats and S. A. Rice. The intramolecular potential of water molecules engaged in hydrogen bonding from analysis of the overtone spectrum of ice I. *J. Chem. Phys.* 71, 973–982 (1979).
108. D. Schiøberg and G. Zundel. Very polarisable hydrogen bonds in solutions of bases having infra-red absorption continua. *J. Chem. Soc. Faraday Transactions II* 69, 771–81 (1973).
109. Y. R. Shen. *The principles of nonlinear optics*. John Wiley & Sons, Inc., New York, 1984.
110. T. Shimanouchi, editor. *Tables of molecular vibrational frequencies consolidated*, volume I. National Bureau of Standards, Washington D.C., 1972.
111. D. W. G. Smith and J. G. Powles. Proton spin-lattice relaxation in liquid water and liquid ammonia. *Mol. Phys.* 10, 451–463 (1966).
112. R. J. Speedy and C. A. Angell. Isothermal compressibility of supercooled water and evidence for a thermodynamic singularity at -45°C . *J. Chem. Phys.* 65, 851–858 (1976).
113. M. Sprik, J. Hutter, and M. Parrinello. *Ab initio* molecular dynamics simulation of liquid water: Comparison of three gradient-corrected density functionals. *J. Chem. Phys.* 105, 1142–1152 (1996).
114. A. Staib and J. T. Hynes. Vibrational predissociation in hydrogen bonded OH...O complexes via OH stretch-OO stretch energy transfer. *Chem. Phys. Lett.* 204(1,2), 197–205 (1993).
115. J. Stenger, D. Madsen, P. Hamm, E. T. J. Nibbering, and T. Elsaesser. Ultrafast vibrational dephasing of liquid water. *Phys. Rev. Lett.* 87(2), 027401-1–027401-4 (2001).
116. L. Stryer. *Biochemistry*. W. H. Freeman and Co., New York, third edition, 1988.
117. M. E. Tuckerman, K. Laasonen, M. Sprik, and M. Parrinello. *Ab initio* molecular dynamics simulation of the solvation and transport of H_3O^+ and OH^- ions in water. *J. Phys. Chem.* 99, 5749–5752 (1995).
118. M. E. Tuckerman, K. Laasonen, M. Sprik, and M. Parrinello. *Ab initio* molecular dynamics simulation of the solvation and transport of hydronium and hydroxyl ions in water. *J. Chem. Phys.* 103, 150–161 (1995).
119. M. E. Tuckerman, D. Marx, M. L. Klein, and M. Parrinello. On the quantum nature of the shared proton in hydrogen bonds. *Science* 275, 817–820 (1997).
120. M. A. F. H. van den Broek and H. J. Bakker. Observation of a bottleneck in the vibrational relaxation of liquid bromoform. *Chem. Phys.* 253, 157–164 (2000).
121. M. A. F. H. van den Broek, H. K. Nienhuys, and H. J. Bakker. Vibrational dynamics of the C-O stretch vibration in alcohols. *J. Chem. Phys.* 114, 3182–3186 (2001).

122. D. van der Spoel, P. J. van Maaren, and H. J. C. Berendsen. A systematic study of water models for molecular simulation: derivation of water models optimized for use with a reaction field. *J. Chem. Phys.* *108*, 10220–10230 (1998).
123. A. Vegiri and S. V. Shevkunov. Hydration shell structure of the $\text{OH}^- (\text{H}_2\text{O})_{n=1-15}$ clusters from a model potential energy function. *J. Chem. Phys.* *113*, 8521–8530 (2000).
124. K. L. Vodopyanov. Saturation studies of H_2O and HDO near 3400 cm^{-1} using intense picosecond laser pulses. *J. Chem. Phys.* *94*, 5389–5393 (1991).
125. G. E. Walrafen. Raman spectral studies of the effects of temperature on water and electrolyte solutions. *J. Chem. Phys.* *44*, 1546–1558 (1966).
126. G. E. Walrafen. Raman spectral studies of the effects of perchlorate ion on water structure. *J. Chem. Phys.* *52*, 4176–4198 (1970).
127. D. Wei, E. I. Proynov, A. Milet, and D. R. Salahub. Solvation of the hydroxide anion: a combined DFT and molecular dynamics study. *J. Phys. Chem. A* *104*, 2384–2395 (2000).
128. K. Winkler, Jörg Lindner, H. Bürsing, and P. Vöhringer. Ultrafast Raman-induced Kerr-effect of water: single molecule versus collective motions. *J. Chem. Phys.* *113*, 4674–4682 (2000).
129. S. Woutersen and H. J. Bakker. The hydrogen bond in liquid water as a Brownian oscillator. *Phys. Rev. Lett.* *83*, 2077–2080 (1999).
130. S. Woutersen and H. J. Bakker. Resonant intermolecular transfer of vibrational energy in liquid water. *Nature* *402*, 507–509 (1999).
131. S. Woutersen and H. J. Bakker. Coherent coupling in frequency-resolved pump-probe spectroscopy. *J. Opt. Soc. Am. B* *17*, 827–832 (2000).
132. S. Woutersen, U. Emmerichs, and H. J. Bakker. Femtosecond mid-IR pump-probe spectroscopy of liquid water: Evidence for a two-component structure. *Science* *278*, 658–660 (1997).
133. S. Woutersen, U. Emmerichs, and H. J. Bakker. A femtosecond midinfrared pump-probe study of hydrogen bonding in ethanol. *J. Chem. Phys.* *107*, 1483 (1997).
134. S. Woutersen, U. Emmerichs, H. K. Nienhuys, and H. J. Bakker. Anomalous temperature dependence of vibrational lifetimes in water and ice. *Phys. Rev. Lett.* *81*, 1106–1109 (1998).
135. H. R. Wyss and M. Falk. Infrared spectrum of HDO in water and in NaCl solution. *Can. J. Chem.* *48*, 607 (1970).
136. A. Yariv. *Introduction to optical electronics*. CBS College Publishing, New York, 1985.
137. Y.-L. Yeh and C.-Y. Mou. Orientational relaxation dynamics of liquid water studied by molecular dynamics simulation. *J. Phys. Chem. B* *103*, 3699–3705 (1999).

138. R. N. Zare. *Angular Momentum: understanding spatial aspects in chemistry and physic.* John Wiley & Sons, 1988.
139. M. Ziolk, R. Naskrecki, M. Lorenc, J. Karolczak, J. Kubicki, and A. Maciejewski. The influence of the excitation geometry on the temporal resolution in femtosecond pump-probe experiments. *Opt. Comm.* 197, 467–473 (2001).

SUMMARY

This thesis describes experiments on liquid water that aimed at obtaining more information on and understanding of the microscopic properties of liquid water. The method is pump–probe spectroscopy on the *OH stretch vibration* in a diluted HDO in D₂O solution. The latter serves as a model system for normal water (H₂O), the macroscopic physical properties (melting point, boiling point, specific heat, etc.) of which are not very different from heavy water (D₂O). In pump–probe experiments on a sample consisting of liquid HDO/D₂O, a short and very intense light pulse, or *pump pulse* vibrationally excites a fraction of the OH groups of the HDO molecules. These OH groups have a strong absorption around a frequency of 3400 cm⁻¹ (i.e., a wavelength of 2.94 μm). The effect of such an excitation is a temporary change in the absorption spectrum of the sample. This change can be observed by measuring the transmittance of a second pulse, or *probe pulse*. Since the normally low transmittance at 3400 cm⁻¹ increases, this change is called *bleaching*. This bleaching is measurable during a few picoseconds. The transient spectrum of the bleaching (i.e., the bleaching as a function of the probe frequency) evolves in time and can be described as a spectral diffusion process with a *spectral correlation time* that is about 0.5 ps [Woutersen et al., Phys. Rev. Lett. 83, 2077 (1999)]. The spectral correlation time is directly related to the timescale of the length fluctuations of the hydrogen bonds in the liquid because in an OH···O hydrogen bond, the OH stretch frequency is related to the O–O distance.

The light pulses that have been employed in the pump–probe experiments were generated by a technique called optical parametric generation and amplification (OPG/OPA), but Chapter 3 discusses a new technique with promising features to generate tunable mid-IR pulses in the range 2.4–7.7 μm through a phase-matched four-wave mixing process in ordinary mid-IR window materials such as calcium fluoride and barium fluoride. In this process, the difference frequency $\nu_3 = 2\nu_2 - \nu_1$ is generated from pump fields ν_1 and ν_2 . The process can be phase-matched to different frequencies by adjustment of the angle between the pump fields.

The lifetime T_1 of an excited OH stretch vibration (in HDO:D₂O) is found to be 0.74 ps at room temperature. However, the lifetime of the bleaching is slightly longer with 0.85 ps and depends on the frequency at which is probed. The lifetime increases with temperature, a quite unusual fact compared to the typical behavior of molecular vibrations in other molecules. From these facts, we conclude that, upon relaxation of the OH stretch vibration, its energy flows into the hydrogen bond OH···O that is donated by the OH group. Moreover, we estimate that the resulting hydrogen-bond excitation decays with a time of 1.0 ± 0.5 ps.

We investigated to what extent the model system HDO:D₂O differs from pure H₂O by performing similar experiments on the OD stretch vibration of HDO dissolved in H₂O, in which the roles of all H and D atoms are exchanged. In the latter, the vibrational lifetime is $T_1 = 1.8$ ps, over 2 times longer than in the former. However, the spectral

correlation time is only slightly different with 0.40 ps instead of 0.5 ps, which justifies the use of HDO:D₂O as a model system to describe the hydrogen-bond dynamics in H₂O.

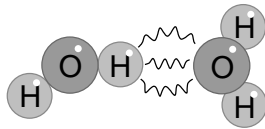
It is generally accepted from dielectric and NMR experiments that the random orientational motion of water molecules can be described with a time constant $\tau_2 \approx 2.5$ ps, which is the average value over all water molecules in the liquid. At any moment, water molecules in liquid water are oriented completely at random. However, by means of polarization-resolved pump-probe experiments, it is possible to use the excited OH stretch vibration to label those HDO molecules that happen to be oriented in a certain direction. This anisotropic orientation distribution can then be followed in time; it turns out that weakly hydrogen-bonded molecules have a much shorter orientation time, while strongly hydrogen-bonded molecules reorient very slowly. This differentiation is possible because pump and probe pulses at different frequencies are sensitive to different hydrogen-bond lengths. The average time constant of 2.5 ps is the result of the hydrogen-bond length fluctuations (that can be interpreted as the rapid making and breaking of hydrogen bonds). The temperature dependence of the frequency-dependent reorientation can be interpreted as an activated process, for which we estimate how the activation energy depends on the OH stretch frequency.

For most purposes, the potential in the OH stretch coordinate can be approximated as a harmonic potential with a small anharmonic perturbation. In this approximation, the OH stretch mode can be described as a harmonic oscillator, whose uniformly-spaced energy levels are slightly perturbed, which results in a $\nu = 1 \rightarrow 2$ transition energy that is lower than its $\nu = 0 \rightarrow 1$ transition. However, a more accurate model [Lippincot and Schröder, JCP 23, 1099 (1955)] of the potential $V(r, R)$ as a function of both the OH stretch coordinate r and the hydrogen-bond coordinate R shows that the approximation of a perturbed harmonic oscillator already breaks down for states $\nu \geq 2$, a fact that is reflected in the $\nu = 1 \rightarrow 2$ contribution in the transient spectrum of HDO:D₂O. The shape of this potential implies that the energetically most favorable path for the autodissociation reaction $\text{H}_2\text{O} \rightarrow \text{H}_3\text{O}^+ + \text{OH}^-$ is via the $\nu = 2$ state with a total activation energy of 79 kJ/mol. This value is comparable to the dissociation enthalpy that follows from the temperature dependence of the pH of water. With the potential $V(r, R)$ it is possible to describe the spectral relaxation more accurately than with the parabolic potentials of the Brownian Oscillator model; the correlation time is 950 ± 100 fs, larger than previously assumed values. A detailed analysis of data with a higher time resolution [Gale et al., Phys. Rev. Lett. 82, 1068 (1999)] show that, directly after excitation, excited molecules undergo a small and rapid inertial shift with a time constant of 170 ± 40 fs.

The hydrogen-bond network in water is completely disturbed if water is used as a solvent for sodium hydroxyde (NaOH). From pump-probe experiments on a 10 mol/l solution of NaOD in HDO:D₂O, we conclude that the broad absorption band of the OH stretch vibration consists of two separate classes of OH groups: (I) OH groups with DO-H...OD₂-like hydrogen bonds, suprisingly similar to those in HDO:D₂O. (II) OH groups with DO-H...OD⁻-like hydrogen bonds, which show a very rapid vibrational relaxation, possibly due to deuteron transfers. For component I, the lifetime of the OH stretch vibration is observed to increase with frequency, which can be explained from the accompanying decrease in the strength of the hydrogen-bond interaction. Spectral holes can be created in this component that change neither position nor width on a picosecond timescale. The spectral diffusion ($\tau \approx 0.5$ ps) in HDO:D₂O is completely absent, which indicates that, in this solution, the hydrogen-bond network is very static.

SAMENVATTING

Dit proefschrift gaat over water en waterstofbruggen. We leren nu op school dat water de chemische formule 'H₂O' heeft, dus dat een watermolecuul bestaat uit twee waterstofatomen en één zuurstofatoom. Achter deze eenvoudige formule gaat echter een bijzonder gecompliceerde vloeistof schuil. Water is de enige stof met vergelijkbaar kleine moleculen die vloeibaar is bij kamertemperatuur. Methaanmoleculen en watermoleculen zijn bijvoorbeeld ongeveer even groot en zwaar, terwijl methaan, hoofdbestanddeel van aardgas, pas vloeibaar wordt na afkoelen tot 161 graden onder nul. Verder zet water fors uit bij bevriezen, met als bijeffect dat ijs blijft drijven. Stel je eens voor dat water, zoals de meeste andere stoffen, zou krimpen bij het bevriezen. De Noordpoolkap zou naar de bodem van de oceaan zinken en de Elfstedentocht zou definitief afgeschaft worden! Waaraan dankt water dit soort eigenschappen nu? Het geheim ligt in de waterstofbruggen die watermoleculen met elkaar kunnen vormen. Een waterstofbrug is een term om de wisselwerking aan te duiden die kan plaatsvinden tussen twee watermoleculen:



Een waterstofbrug, die altijd loopt van het waterstofatoom (H) van het ene molecuul naar het zuurstofatoom (O) van het andere, 'poogt' als een soort veer de afstand tussen de twee watermoleculen vast te houden; het kost dus energie om twee watermoleculen van elkaar te scheiden. Een watermolecuul kan vier waterstofbruggen vormen, met vier andere watermoleculen. In ijs worden er daadwerkelijk vier gevormd, waardoor een star driedimensionaal netwerk ontstaat: ijs is een vaste stof. Bij het smelten van water verbreekt dit netwerk en wordt het een dynamisch krioelend geheel van moleculen die waterstofbruggen vormen en weer verbreken. Gemiddeld heeft elk molecuul dan zo'n drie-eneenhalve waterstofbrug.

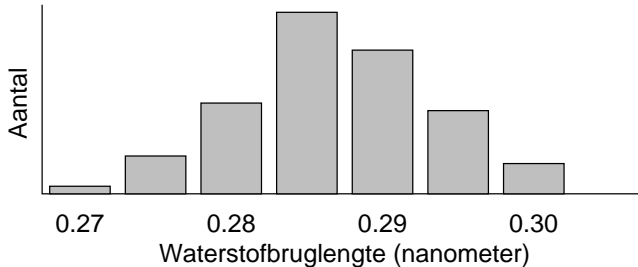
Veel van dit soort kennis over water is bekend geworden door de 'gemiddelde eigenschappen' van water te bestuderen. Daarbij kun je denken aan hoe de soortelijke warmte en het soortelijk gewicht afhangen van de temperatuur en druk, of (neutronen-)diffractie, die informatie oplevert over de gemiddelde onderlinge afstanden tussen de moleculen. Zulke methoden verschaffen helaas geen informatie over de dynamiek van de waterstofbruggen, die plaatsvindt op een tijdschaal van typisch 10^{-12} seconden (een miljoenste van een miljoenste seconde, ofwel 1 picoseconde). Sinds enkele jaren is er een techniek beschikbaar om dergelijke snelle processen in water te volgen: tijdsopgeloste mid-infraroodspectroscopie. De experimenten aan water die ik in dit proefschrift beschreven heb, zijn gedaan met deze techniek.

Water is transparant voor zichtbaar licht, dat golflengtes heeft van ongeveer 400 tot 700 nanometer (een nanometer is een miljoenste millimeter). Dat geldt echter niet voor

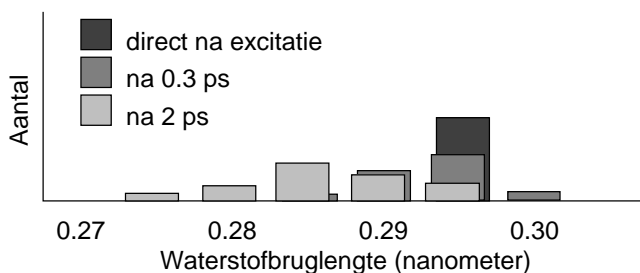
infrarood licht met een golflengte van ongeveer 2940 nanometer. In het infrarood heeft water meer weg heeft van paarse inkt: een laagje water van een honderdste millimeter dik laat vrijwel geen licht van die golflengte door, maar wel van iets kortere ('blauwe') en iets langere ('rode') golflengtes, vandaar de kleur paars. In wetenschappelijke termen: de OH-vibratie van H_2O absorbeert bij 2940 nanometer. Nu heeft deze OH-vibratie de eigenschap dat de precieze absorptiegolflengte samenhangt met de lengte van de waterstofbrug. Langere waterstofbruggen absorberen bij kortere golflengtes:



In water zijn zowel moleculen met korte als met lange waterstofbruggen aanwezig. Elk watermolecuul absorbeert dus bij een eigen, specifieke golflengte. Door de infraroodabsorptie precies te meten, kun je nu vaststellen hoeveel moleculen er voor elke waterstofbruglengte zijn, waaruit je een verdeling als de onderstaande kunt construeren.



Dit grafiekje vertelt nog steeds niets over de dynamiek in water. Een waterstofbrug die op het ene moment een lengte van 0,275 nanometer heeft, kan een paar picoseconden later best 0,29 nanometer zijn geworden, of zelfs helemaal zijn verbroken. Om deze dynamiek waar te nemen, gebruiken we een ultrakorte puls infrarood licht die heel specifiek worden geabsorbeerd door watermoleculen met een bepaalde waterstofbruglengte. Deze moleculen worden dan, in natuurkundige termen, *geëxciteerd*. Met een golflengte van bijvoorbeeld 2830 nanometer kun je specifiek watermoleculen exciteren die een waterstofbruglengte hebben van 0,295 nanometer. Doordat de aldus geëxciteerde moleculen andere absorptie-eigenschappen hebben, is het mogelijk de moleculen in de tijd te volgen. Hiervoor gebruiken we een tweede puls infrarood licht die met een korte tijdsvertraging na de eerste puls door het te onderzoeken water gaat. Door dit tweepuls-experiment te herhalen voor verschillende tijdsvertragingen en infraroodgolflengtes, kun je rechtstreeks zien hoe de waterstofbruglengtes van deze geëxciteerde moleculen variëren in de tijd:



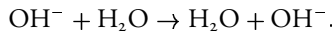
Door een dergelijke verdeling te meten kun je tot de conclusie komen dat waterstofbruggen binnen ongeveer 1 picoseconde sterk van lengte kunnen veranderen. Wat zegt dat getalletje, de zogenaamde *waterstofbrugcorrelatietijd*, nu? Ik heb zo-even geschetst dat vloeibaar water een dynamisch krioelend geheel is. Stel je maar eens voor hoe een mierenhoop eruit ziet op een warme zomerdag. Als je een foto van die mierenhoop zou maken met een sluitertijd die voldoende kort is, dan krijg je een foto waarop je duidelijk kunt zien hoe mieren even stilstaan om elkaar met hun voelsprietten te betasten. Zou je een lange sluitertijd nemen, van bijvoorbeeld 1/4 seconde, dan heb je een bewogen foto waarop je geen afzonderlijke mier meer kunt herkennen. Welnu, die ene picoseconde betekent dat watermoleculen alleen lijken te krioelen als je langer wacht dan ongeveer 1 picoseconde. Als je maar gedurende een veel kortere tijd, bijvoorbeeld 0,1 picoseconde, naar de watermoleculen kijkt, lijken de moleculen nauwelijks ten opzichte van elkaar te bewegen. Er blijft echter wel een soort snelle 'bibbering' van de moleculen over, vergelijkbaar met mieren die elkaar met hun voelsprietten betasten. Deze snelle, maar in omvang beperkte, beweging is ongeveer zes maal zo snel als de waterstofbrugcorrelatietijd.

In werkelijkheid zijn er allerlei details waar je rekening mee moet houden die enerzijds de interpretatie wat ingewikkelder maken, en anderzijds op zich ook interessante informatie bevatten. Na een infraroodpuls blijft een watermolecuul bijvoorbeeld niet eeuwig in een geëxciteerde toestand zitten; de excitatie verdwijnt gemiddeld na ongeveer 0,8 picoseconden. Deze zogenaamde *vibratielaxatie* wordt beïnvloed door de temperatuur op een manier die blijkt te verklaren doordat de energie van de excitatie wordt opgenomen door een waterstofbrug. Hierbij is te schatten dat die waterstofbrug op zijn beurt zijn energie afstaat aan de omgeving binnen ongeveer 1 ps.

Om technische en praktische redenen zijn de metingen niet gedaan aan normaal water (H_2O), maar aan zwaar water (D_2O) met een klein beetje 'half-zwaar' water (HDO) erin opgelost. Zwaar water en gewoon water zijn chemisch vrijwel identiek, maar verschillen met name in hun absorptie-eigenschappen voor infrarood licht. Om af te schatten in hoeverre het gebruik van zwaar water in plaats van 'gewoon' water de metingen heeft beïnvloed, hebben we metingen gedaan aan een omgekeerd systeem: in plaats van HDO opgelost in D_2O hebben we gemeten aan HDO opgelost in H_2O . Het blijkt dat met name de vibratielaxatie wat langzamer gaat, terwijl de fluctuaties in waterstofbruglengtes juist iets sneller gaan. Er zijn dus verschillen tussen gewoon water en zwaar water, maar deze zijn niet dramatisch, dat wil zeggen pakweg een factor 2.

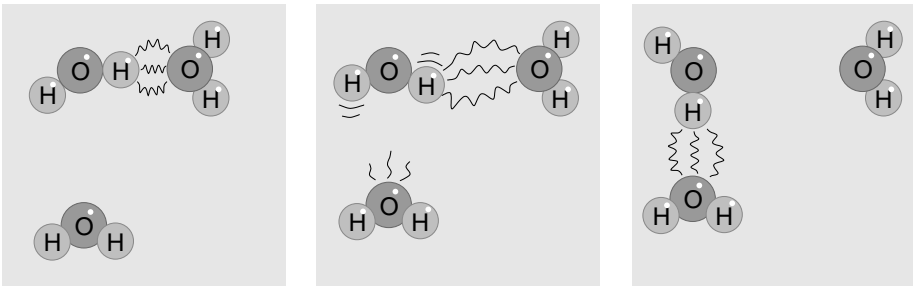
De waterstofbrugdynamica verandert volledig als je *natriumhydroxide* (chemische formule: NaOH) in water oplost. Deze stof staat in veel huishoudens in het keukenkastje onder de naam 'gootsteenontstopper.' Door natriumhydroxide in water op te lossen, krijg je natronloog, met daarin Na^+ - en OH^- -ionen. Het blijkt dat watermoleculen in een

geconcentreerde oplossing hiervan zich behoorlijk anders gedragen dan in normaal water. De waterstofbrugcorrelatietijd wordt zo lang(zaam) dat hij niet meer is te onderscheiden met onze meettechniek, dus pakweg 10 picoseconden of langer, in plaats van 1 picoseconde, zoals in gewoon water. Deze langzame beweging heeft betrekking op het maken en verbreken van waterstofbruggen. Verrassend genoeg is de snelle 'bibbering' van de watermoleculen, waarbij de watermoleculen nauwelijks van plaats veranderen, wel vrijwel hetzelfde. Om het nog ingewikkelder te maken: er blijken twee soorten watermoleculen in deze oplossing te zitten. De eerste heb ik hierboven geschetst; de tweede heeft een enorm snelle vibratielaxatie: 0,14 in plaats van 0,8 picoseconden. Het vermoeden is dat deze watermoleculen het slachtoffer zijn van *protonuitwisseling*, waarin een OH^- -ion een proton (H^+) van een watermolecuul 'afpakt':



Dit kan alleen watermoleculen overkomen die toevallig de goede oriëntatie hebben ten opzichte van een OH^- -ion, zo blijkt uit de metingen.

Tot nu toe hebben we het 'kriolende mierennest' water bekeken door te kijken hoe de waterstofbruggen in lengte variëren. Het is ook mogelijk te kijken hoe watermoleculen van oriëntatie veranderen, dus hoeveel tijd een watermolecuul nodig heeft om vanuit een horizontale positie een verticale positie aan te nemen, of andersom. Watermoleculen met een korte waterstofbrug blijken niet of nauwelijks te reoriënteren, in tegenstelling tot watermoleculen met een lange waterstofbrug. Je zou dus kunnen zeggen dat reoriëntatie en variaties in waterstofbruglengte twee aspecten van hetzelfde proces zijn:



Twee waterstofgebrugde watermoleculen (links) verwijderen zich van elkaar (waterstofbrug wordt langer); het molecuul krijgt nu bewegingsvrijheid (midden), waarbij de waterstofbrug nog verder uitgerekt wordt; de oorspronkelijke waterstofbrug wordt verbroken en een nieuwe waterstofbrug wordt gevormd (rechts).

Dat was in een notendop de inhoud van dit proefschrift. De motivatie om dit alles uit te zoeken komt in het volgende hoofdstuk.

NAWOORD

Natuurkundigen zijn als kleine kinderen, zij het met dunder speelgoed. Misschien geldt het niet voor alle natuurkundigen, maar voor mij lijkt deze stelling wel op te gaan. Door te spelen zonder vooropgezet doel ontdekt een kind hoe de wereld in elkaar zit. Zo is in feite mijn enthousiasme voor natuurkunde gewekt op de middelbare school. Idealiter zou natuurkundig onderzoek ook zo moeten werken. Helaas kom je er niet alleen maar met spelen; je moet regelmatig ook gewoon de tanden op elkaar zetten en doorgaan, ondanks twijfels of alle inspanningen ook wat zullen opleveren. Behalve speels zijn kinderen ook nieuwsgierig. Kleine kinderen schijnen vaak een ‘waarom’-periode door te maken, waarin zij hun ouders tot waanzin drijven door bij alles wat ze zien of horen de vraag ‘Waarom?’ te stellen. Het bedrijven van wetenschap is het blijven stellen van die vraag. Ik ben mijn ouders dankbaar dat zij altijd geduldig antwoord bleven geven op al mijn kindervragen. Die nieuwsgierigheid is gebleven; inmiddels is gebleken dat niet iedereen even geduldig is, al is dat verbeterd sinds ik heb geleerd dat je met ‘Is dat echt zo?’ verder komt dan met ‘Dàt geloof ik niet.’

Als natuurwetenschapper heb je vaak het probleem dat je onderzoek zo gespecialiseerd is en zo ver van de alledaagse werkelijkheid staat, dat het voor een buitenstaander volslagen abracadabra is. Toen ik aan mijn promotie begon, dacht ik dat dat met het onderwerp ‘water’ wel anders zou zijn, want water, dat kent immers iedereen. Helaas werkte dat maar ten dele zo. Want hoe interessant ook, de dynamica van waterstofbruggen is nog steeds maar een heel klein aspectje van water. Alle nieuwe kennis die ik in dit proefschrift heb opgetekend zal niet direct leiden tot een oplossing van het wereldwijde drinkwaterprobleem of tot energieopwekking uit water. Het dient slechts ter bevrediging van de nieuwsgierigheid van hen die nieuwsgierig zijn, als een deeltje in de encyclopedie van de menselijke kennis.

Dan wil ik nu degenen bedanken die hebben bijgedragen aan deze promotie. Allereerst mijn promotoren, Rutger van Santen en Huib Bakker. Rutger heeft mijn promotieonderzoek mogelijk gemaakt, een samenwerking tussen zijn vakgroep aan de TU Eindhoven en Huibs groep op AMOLF in Amsterdam. Ondanks de kilometers tussen ons, heeft Rutger altijd grote betrokkenheid getoond met mijn promotieonderzoek. Huib is begiftigd met een razendsnelle intuïtie. Een paar minuten kijken naar een stapel grafieken en daar was een theorie die, na een gedetailleerde analyse, maar al te vaak juist bleek. Los van de wetenschappelijke kant dank ik Huib ook voor zijn licht anarchistische kijk op het leiding geven, waardoor er ook plaats was voor spelen, en voor de keren dat hij me wist op te beuren wanneer ik het even niet zag zitten. Twee belangrijke voorgangers heb ik gehad: Uli Emmerichs, die de originele meetopstelling heeft gebouwd, en Sander Woutersen, die mij heeft ingewerkt en met zijn werk de fundamenten heeft gelegd waarop ik heb doorgebouwd. Verder hebben mijn andere naaste collega’s gezorgd voor een prettige samenwerking en sfeer binnen onze de groep: Frederik van den Broek, Michel Kropman, Arjan Lock en Anne Willem Omta. Met Frederik heb ik menig uurtje ’s avonds en ’s nachts op het lab doorgebracht, zowel in Amsterdam als in Rijnhuizen. Michel heeft, nog als

stagiair, de metingen van hoofdstuk 5 gedaan. Arjan heeft een gedeelte van de metingen in hoofdstuk 6 gedaan. Ook noem ik hier mijn ex-groepsleden Issa Abu Shiekah, Ingrid Giebels en Mingcheng Zong. Van de TU Delft afkomstig is Paul Planken, met zijn onnavolgbare creativiteit en aanstekelijke humor, die mij inwijdde in de principes van ver-infraroodspectroscopie, wat uitmondde in de metingen van hoofdstuk 3.

AMOLF is een fantastische omgeving voor wetenschappelijk onderzoek. Een afwezigheid van bureaucratie—geen vier handtekeningen voor elke onbenullige bestelling; de interactie tussen onderzoeksgroepen—je weet wie wat doet, zodat je altijd mensen om advies of hulp kunt vragen, en de technische ondersteuning—voor elk elektronisch of mechanisch probleem is er wel iemand die daar verstand van heeft. Op zulke zaken moet je zuinig zijn! Hinc Schoenmaker en Rob Kemper dank ik voor hun technische ondersteuning op het mechanische vlak, waarin zij werden bijgestaan door de fijnmechanische werkplaats. Hans ter Horst, Idsart Attema, Hans Alberda en de rest van de afdeling E&I hebben geholpen bij het oplossen van allerlei elektronische kwesties. Van de TU Eindhoven wil ik in het bijzonder Wout van Herpen bedanken, die de samplecel heeft gebouwd voor de metingen in hoofdstukken 4 en 7.

Dan resten nog de overige AMOLFers. Harm Geert Muller wist altijd hoe je nóg meer berekeningen uit een Pentiumprocessor kon persen en was een vraagbaak die overal verstand van had. De onbevengene houding van Wim van der Zande, die steeds oprecht zijn verbazing en enthousiasme toonde, was altijd erg verfrissend. Verder zijn er nog alle andere leden van de afdeling QDAMS (voorheen atoomfysica), plus de nodige mensen van buiten de afdeling. Ik durf ze niet allemaal op te noemen, want dan vergeet ik vast een van degenen die inmiddels elders werken. Mensen, bedankt voor de prettige sfeer door de jaren heen!

CURRICULUM VITAE

Han-Kwang Nienhuys werd in 1973 geboren in Utrecht. In 1991 behaalde hij het athe-neumdiploma aan het Hertog Jancollege in Valkenswaard. Vanaf 1991 volgde hij de studie experimentele natuurkunde aan de Universiteit Utrecht, waar hij in 1995 een onder-zoek deed op het gebied van elektronspinresonantie in de groep van E. E. van Faassen en Y. K. Levine (Moleculaire Biofysica). Zijn afstudeeronderzoek bij de groep van A. F. M. Arts en H. W. de Wijn (Gecondenseerde Materie) was getiteld '*Monochromatic phonon beams: generation at oblique angles and experiments on reflection.*' In 1997 voltooide hij zijn studie met het judicium *cum laude*, waarna hij als AIO begon bij R. A. van Santen (Katalyse & Anorganische Chemie) aan de Technische Universiteit Eindhoven. Zijn promotieonderzoek verrichtte hij op het FOM-Instituut voor Atoom- en Molecuulfysica te Amsterdam in de groep van H. J. Bakker (Vibratiedynamica).

Han-Kwang Nienhuys was born in Utrecht, Netherlands, in 1973. In 1991, he obtained the Atheneum degree at the Hertog Jancollege in Valkenswaard. Starting in 1991, he studied experimental physics at Utrecht University, where he carried out a research project in the field of electron spin resonance in the group of E. E. van Faassen and Y. K. Levine (Molecular Biophysics). His M.Sc. project at the group of A. F. M. Arts and H. W. de Wijn (Condensed Matter Physics) was titled '*Monochromatic phonon beams: generation at oblique angles and experiments on reflection.*' In 1997, he was awarded his M.Sc. degree *cum laude*, after which he started as a Ph.D. student with R. A. van Santen (Catalysis and Anorganic Chemistry) at the Eindhoven University of Technology. He carried out his Ph.D. work at the FOM Institute for Atomic and Molecular Physics in Amsterdam in the group of H. J. Bakker (Vibrational Dynamics).

INDEX

- absorbance
 - induced, definition, 28
- absorbance change
 - definition, 14
 - isotropic, 15
 - measuring, 24
- absorbance, definition, 13
- activation energy
 - autodissociation, 99
 - reorientation, 74, 76, 78, 80–81
- adiabatic approximation, 89
- anharmonic redshift, 28
- Arrhenius equation, 74
- artifact
 - coherent, 29
 - cross-phase modulation, 29
- asymmetry of transient spectra, 87
- autodissociation of water, 97–100

- background from pump stray light, 75
- BBO, 19
- beam angle, effect on time resolution, 25
- birefringence of sapphire, 23
- bleaching, definition, 28
- blueshift, 47
- Brownian oscillator
 - distribution of, 63–65
 - model, 53–55

- Cavendish, 10
- cm^{-1} , conversion, 102
- coherent artifact, 29
- compressibility of water, 68
- correlation time
 - rotational, 15
 - spectral
 - HDO:H₂O, 58
 - NaOX solution, 67
- cross-correlation function, 26
- cross-phase modulation artifact, 29
- crossection of HDO, 16

- Debye time, 73
- Debye-Stokes-Einstein equation, 73
- $\Delta\alpha$, *see* absorbance change
- deuteron transfer, 70–71
- difference-frequency generation, 18
- diffusion equation
 - heat, 34
 - numerical solution, 85
 - reorientation, 83
 - spectral (in potential), 83
- diffusion equation, spectral (in potential), 94

- energy-gap law, 57
- error margins, notation of, 15
- experimental setup
 - pump–probe, 23–25
- experimental setup, photo, 9

- fractional power law, 74
- FTCS algorithm, 34
- FWHM, definition, 20

- geometrical factor (ξ), 14
- geometry of overlap region, 24
- germanium
 - for pulse characterisation, 26
- Grotthuss, 98

- HDO in D₂O, reason for use, 15
- HDO, crossection of, 16
- HDO:D₂O, IR spectrum, 13
- HDO:H₂O, IR spectrum, 51
- heat diffusion equation, 34
- heating of sample
 - accumulated, 33
 - one pulse, 23, 33, 55
- homogeneous broadening, 27
 - by fast modulation, 28, 69
 - in HDO:D₂O, 69
- hydrogen-bond network, picture, 10

- ice, 42
idler (in OPG/OPA), definition, 19
induced absorbance, definition, 28
inertial shift, 97
instrument function, 26
 convolution, 27
intermediate-state model, 43–46
isotope effects on vibrational dynamics,
 50–58
isotropic absorbance change, 15
- Kerr effect, 74
KTP, 19
- Laenen, *see* coherent artifact
Lavoisier, 10
lifetime
 dependence on frequency, 48, 63
 fast component in NaOX solution,
 65
 hydrogen-bond excitation, 49
 OD stretch in HDO:H₂O, 56–57
 OH stretch in HDO:D₂O, 44
- magic angle, 15
molecular dynamics simulation
 autodissociation, 100
 NaOH solution, 61, 70
 reorientation, 81
motional narrowing, 69
movie camera, 13
- NaOX
 IR spectrum, 59–60
NMR, measuring reorientation with, 13,
 73, 81
noise suppression, 30–33
- Ockham's razor, 67
optical parametric amplification, 19
optical parametric generation and am-
 plification, 18
orientational relaxation
 HDO:D₂O, 73–85
 NaOX solution, 68–69
overlap region, geometry of, 24
overtone spectrum, 91
- phase matching
 condition, 19, 36
 four-wave mixing, 37
 types, 19
phlogiston, 10
proton transfer, *see* deuteron transfer
pump–probe spectroscopy
 principles, 13–15
 setup, 23–25
- redshift, 48
relaxation time, *see* lifetime
rotational anisotropy
 HDO:D₂O, 75
 measurement, 31
 NaOX solution, 68
rotational correlation time, 15
- sapphire, birefringence of, 23
second-harmonic generation, 18
signal (in OPG/OPA), definition, 19
signals, magnitude of, 16
solvation shells, 59
spectral correlation time
 HDO:H₂O, 58
spectral diffusion
 in harmonic potential, 53, 83
spectral diffusion, in potential, 94
spectral hole, 63
Stokes shift
 for harmonic potentials, 53
sum-frequency generation, 18
 for pulse characterisation, 26
- thermalization of vibrational energy, 55
time resolution, effect of beam angle, 25
TOPAS, 20
transient spectra
 asymmetry, 87
 HDO:D₂O, 88
 NaOX solution, 62
transient spectra, calculation, 91–92
two-state mixture model, 11
- v*, use of symbol, 15
vibrational modes of water, 11, 12, 48
vibrational relaxation

- HDO:D₂O, 41-49
- Voigt lineshape, 70

- water (H₂O), IR spectrum, 12
- water vapor, IR spectrum, 12
- wave number, conversion, 102

- zeolites, 57
- zero point, deviation in germanium, 27

COLOPHON

Both the cover and the inside of this thesis were typeset with $\text{\LaTeX} 2_{\epsilon}$. The font used for the text was Adobe Garamond, which is a digital reproduction of the roman fonts originally designed by Claude Garamond (1499–1561) and the italic fonts designed by Robert Granjon (1530–1589). With the help of Mathkit 0.7, the Greek and mathematical symbols are typeset in a version of Computer Modern, for which the METAFONT parameters were adjusted such that the appearance of the symbols harmonized with Adobe Garamond. The diagrams were prepared with XFig 3.2.2, the plots with Gnuplot 3.7.1, except for Fig. 2.9, which was prepared with Gri 2.8.2. No Windows software was used in the preparation of this thesis. The symbol \star on the cover is the Chinese character *shuǐ* (pronounced more or less as ‘shway’), which means ‘water.’ It was calligraphed by the author’s mother. This thesis is printed by PrintPartners Ipskamp, Enschede.

SPECTROSCOPY
MID-INFRARED
FEMTOSECOND

OF

WATER



HAN-KWANG NIENHUIS